Optical Emission Spectroscopy to Determine Electron Energy Distributions with Enhanced High Energy 'Tails' in 'Low-temperature' Plasmas

By

Shicong Wang

A dissertation submitted in partial fulfillment of the
requirements for the degree of

Doctor of Philosophy
(Electrical and Computer Engineering)

at the
University of Wisconsin-Madison
2016

Date of final oral examination: 09/23/2016

The dissertation is approved by the following members of the Final Oral Committee:

Wendt, Amy E. Professor, Professor, Electrical and Computer Engineering
Anderson, David T. Professor, Professor, Electrical and Computer Engineering
Lin, Chun C. Professor, Professor, Physics
Sovinec, Carl R. Professor, Professor, Engineering Physics
Schmitz, Oliver Professor, Assistant Professor, Engineering Physics

Abstract

"Low-temperature" plasmas are weakly ionized gases with many technological applications, including the fabrication of integrated circuits. Diagnostics to determine plasma properties are desirable tools for application development, control and model verification. Processes depend on gas phase reactions involving plasma electrons, which are selectively heated to temperatures in the range of kT_e 1-10 eV. Because atom and molecule collisions with the most energetic portion of the electron population are responsible for a large proportion of the excitation, ionization and dissociation reactions central to plasma applications, diagnostics to measure this portion of the electron energy distribution function (EEDF) hold particular value.

The topic of this study is a non-invasive diagnostic that makes use of the wavelength dependence of the spectrum of emitted light from the plasma to determine the high-energy portion of the EEDF. A previously developed emission model employs published energy-dependent collision probabilities to compute relative light intensities for a set of characteristic emission wavelengths. Spectra are computed using this model for set of trial EEDFs and the "best fit" EEDF is selected from this set as that for which the predicted spectrum is found to be closest to the measured spectrum.

The analysis relies on the use of a mathematical function with adjustable parameters to express the forms of the energy dependence in the trial EEDFs. One notable contribution of this study is the introduction of the log-normal distribution as a simple function that can represent a wide range of shapes (energy dependence) for the high-energy portions of EEDFs.

The diagnostic was implemented on an inductively coupled plasma with an auxiliary electron source. The EEDF was manipulated systematically by varying the current and energy of the injected electrons. While the original emission model employed light emissions resulting only from the electronic excitation of neutral argon atoms, it was found that additional wavelengths corre-

sponding to higher energy excitation thresholds are needed. Robust measurements of the EEDF tail were achieved for a range of operating conditions through the inclusion of emissions from Ar^+ ions and the use of a gas mixture of argon, helium and neon in both experiment and emission model.

Acknowledgements

I must thank all of family, friends, and co-workers who have helped me, encouraged me, and supported me throughout these past five years. I would like to give special recognition to the following people:

I want to thank my advisor Professor Amy Wednt. It has been an honor to be her Ph.D. student. I appreciate all her contributions of time, ideas, and funding to make my Ph.D. experience productive and stimulating. She has help me countless times on every aspects of my research, including physics problems, reasoned through experimental results, and wrestled with technical writing and presentation. I have learned to think, work and write like a professional engineering. Her mentorship was paramount in providing a well rounded experience consistent my long-term career goals. She encouraged me to not only grow as an experimentalist and an engineer but also as an instructor and an independent thinker. I am not sure many graduate students are given the opportunity to develop their own individuality and self-sufficiency by being allowed to work with such independence. I am also thankful for the excellent example she has provided as a successful engineer and professor. Her attitude toward the job and research really inspires me.

Many thanks to my colleague Dr. John Boffard. He is an excellent scientist and has answered so many questions for me. He often has many "bad" ideas and "wacky" ideas which are really helpful when I struggle with research problems. When I first got to the lab, I had really limited knowledge about the instruments, the research and essentially everything. I learned my though process and actions in the laboratory by watching or listening to John's methods, suggestions. John has enlightened and entertained me with his witty explanations and unending knowledge of nearly every topic about research and everyday life.

I also want to thank all the members of our research group: Nathaniel Ly and Juan Carlos

Ruiz Bello. Nathan has been a nice and helpful person. He helped me a lot with data taken for my research. I hope everything goes well for your research. Carlos has only been in our group for a short time. But he was so nice and friendly that we became good friends real quick. I hope you have a good time working with Professor Wendt, John and Nathan.

I especially thank my mom, dad. My hard-working parents have sacrificed their lives for myself and provided unconditional love and care. I love them so much, and I would not have made it this far without them. I know I always have my family to count on when times are rough. They encouraged me so many times when I felt frustrated and confused. I owe my greatest acknowledgement to my family.

Contents

List of Tables

List of Figures

Chapter 1

Introduction

The topic of this thesis is optical emission diagnostic tools to determine plasma properties in discharges for use in industrial applications [1, 2, 3]. Industrial plasmas create great societal benefits through the technologies they enable, ranging from energy efficient light sources [4, 5] and plasma televisions to medical treatments [6, 7, 8], computer chips [9, 10, 11, 12, 13] and food science [14], as just a few examples. The economic impact over the last two decades has been significant, and continued growth is expected in coming years, as new applications emerge and as control over plasma behavior becomes more refined.

Many industrial plasmas are considered low-temperature plasmas [1, 13, 15]. "Low temperature" is a relative term, indicating temperatures lower than in so-called "hot plasmas," such as those found in stellar interiors and in fusion experiments [16]. In addition to the temperature difference, low-temperature plasmas (LTP) and hot plasmas also have several other differences with significant implications. Specifically, compared to their hot plasma 'cousins,' most LTPs used in technological applications have lower charged particle densities, a low degree of ionization, *and* are not in thermodynamic equilibrium [17]. A result of the former is that LTP electrons are more likely to collide with neutral atoms and molecules than with other charged particles [18]. LTP discharges are sustained by an electric power input that produces electric fields that preferentially heat electrons, due to their low mass. Because collisional energy transfer through elastic collisions between the electrons and other species is inefficient due to the mass difference, electron populations in LTPs are typically much hotter than anything else around them, including the ion populations, the neutral gas and the surrounding surfaces [13]. In fact, the electrons in a "low-temperature" plasma

typically have temperatures in the 1 to 10 eV range (11,000 to 110,00°K), while everything around them is close to room temperature, and the plasma never attains thermodynamic equilibrium. Both of these properties of LTP discharges make them uniquely suited for particular technological purposes [15], producing results that cannot be obtained by other methods.

Although trial-and-error once served as an adequate strategy for development of plasma applications, fundamental plasma science plays a growing role as plasmas are used in more sophisticated ways. For many materials processing applications, outcomes rely on fine control of energy flow and particle fluxes to substrate surfaces [9, 14, 19]. A good example of this is the fabrication of integrated circuits (IC), in which computer chips are created on a planar surface of a disk or 'wafer' of what starts out as a perfect crystal of nearly pure silicon. Process steps making use of plasmas have played a big role in the success of Moore's Law, the famous prediction made 50 years ago by Intel co-founder Gordon Moore, stating that the density of electronic components on integrated circuits would double annually at minimum manufacturing cost [20].

There are many steps to fabricate computer chips, such as those in our computers, phones and tablets, from a silicon wafer. One of the most critical is the etch step [21, 22, 23, 24], which is used each time a pattern is transferred into the silicon or a deposited layer by selective removal of material through a stencil or "mask." Plasma (or "dry") etching was introduced in the 1970s as an alternative to etching with wet chemicals. Because ion bombardment of substrate surfaces exposed to a plasma can produce anisotropic etching, the introduction of plasma etching led to an immediate improvement in the fidelity of pattern transfer compared to wet etching. Improvement in control over feature dimensions achieved with plasma etching has enabled subsequent steady reduction in component size over the years, leading to the present "22 nm node" in IC production; the most powerful processors now contain nearly 2 billion transistors per chip [9]. Another important aspect of plasma etching processes is selectivity, the preferential etching of one type of material over others, enhancements of which have also improved IC performance by enabling a reduction in the thickness of critical material layers within the IC [25]. In addition, advances in plasma source design to improve process uniformity have enabled a progressive increase in the diameter of silicon wafers used in fabrication, from 100 mm in the 1970s to 300 mm today, increasing throughput and thereby reducing the cost per chip [26, 27].

Further improvements in processor performance with reduced power consumption have recently

been realized with novel transistor architectures, such as the FinFET [28]. Compared to the planar transistor geometry that has been the standard in IC fabrication for decades, FinFETs are three dimensional structures that place even greater performance requirements on the plasma processes used to fabricate them [9, 29]. The advances in plasma processing for IC fabrication to date have been facilitated by a growing understanding of the physical phenomena that govern their behavior.

The research in this thesis is motivated by the prospect of continued advances in plasma process technologies for IC fabrication, and the ways that diagnostic tools could serve as an aid in achieving those advances. Knowledge about the plasma state provided by diagnostics could inform an increasingly first principles approach to process design, optimization and control. The focus of this thesis is on diagnostics to determine properties of the electron population because of the central role they play in establishing discharge properties that directly affect process results. The electron population, through inelastic collisions, is responsible for ionization, which sustains the discharge, electronic excitation of atoms and molecules, resulting in photon emission and the characteristic plasma glow, and dissociation reactions, which produce "radicals," i.e., atoms or molecules that are highly chemically reactive with certain materials (Fig. 1.1). In the case of plasma etching, electrons are thus responsible for the production of radicals and bombarding ions, the energies and relative fluxes of which govern etch rate, anisotropy, and selectivity. The collision probabilities for all of these processes are dependent on electron energy, and the rates of ionization and electron-driven gas phase chemical reactions are a function of both electron density and the distribution of electron energies [19, 30, 31].

The non-equilibrium nature of LTPs is an important factor in the use of plasma processes for IC fabrication. Because the electrons are so energetic, gas phase chemical reactions are possible that in the absence of a plasma would require temperatures that would destroy the circuits being fabricated on the silicon wafer. In the presence of a plasma, however, such high-temperature reactions can take place while the substrate is kept at or near room temperature.

The energy distribution for a particular species specifies its volume concentration as a function of energy. Because rates for processes like charged particle generation, light emissions and electron driven chemical reactions are sensitive to subtle changes in the electron energy distribution function (EEDF), the EEDF is fundamental to assessing the plasma state. As shown in Fig. 1.2, only electrons with sufficient energies (above threshold energies for reactions) can contribute to these

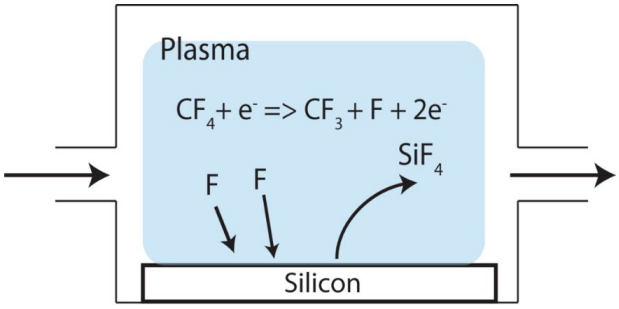

Figure 1.1: An example of chemical reactions occur in low temperature gas caused by electrons in plasma etching process.

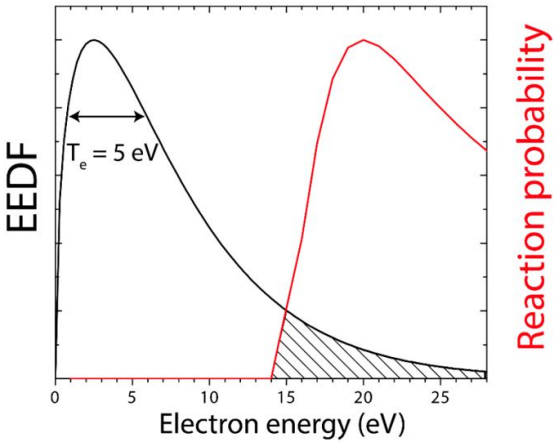

Figure 1.2: Electron collision driven reactions are dominated by high energy electrons.

collision driven reactions, and the rates of these reactions are dominated by the distribution of the high-energy portion of the EEDF. In order to highlight the high energy portion of the EEDF, it can also be represented as an electron energy probability function (EEPF), which equals EEDF/$\sqrt{E}$. It is possible for a plasma electron population to be in thermodynamic equilibrium with itself, even when it is not in equilibrium with other gas phase species. In this case, the EEDF follows a Maxwell-Boltzmann (Maxwellian) distribution, characterized by two quantities, the electron temperature, T_e, and density, n_e. Technological plasmas, however, typically are strongly *non*-equilibrium in the energy distributions of their charged constituents [32, 33, 34]. For example, previous experiments and simulation studies of inductively coupled plasmas (ICPs) [35, 36, 37, 17] report a nearly Maxwellian EEDF in the lower energy range and a 'depleted high-energy tail'. As illustrated in Fig. 1.3, in an argon capacitively coupled plasma (CCP) over a pressure range between 3 mTorr

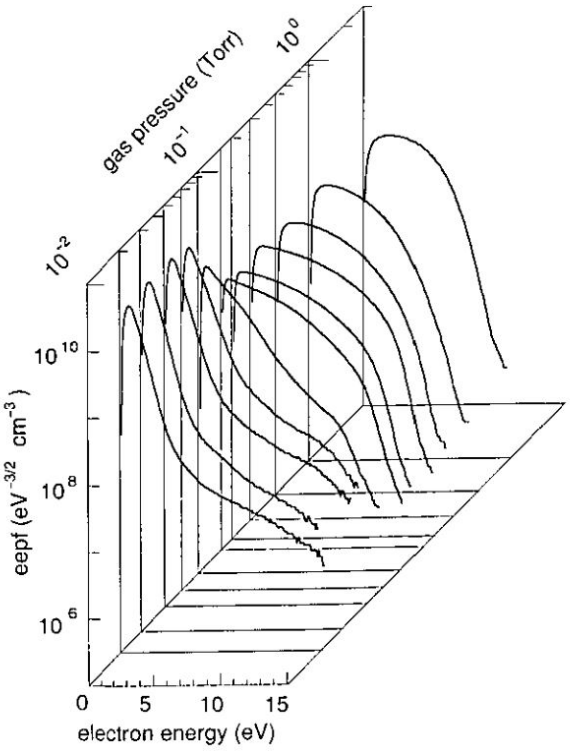

Figure 1.3: EEPF evolution with pressure in argon CCP [32].

to 3 Torr, Godyak *et al.* observed the EEDF varies from a non-Maxwellian EEDF with enhanced high-energy tail to a Maxwellian distribution, and then to a non-Maxwellian EEDF with depleted tail [32]. Different EEDF shapes (i.e., Maxwellian, depleted or enhanced tail EEDF) may result in a large difference in the number of electrons greater than the threshold energies for electron collision driven reactions, and therefore affects the reaction rates (Fig. 1.4). Therefore, the EEDF, especially the high energy portion, is important to control the electron driven chemical reactions. Despite inaccuracies, the practice of attributing an electron temperature to LTPs is widespread due to the simplicity of the Maxwellian form of the EEDF as well as challenges in determining and representing the true form. Considerable understanding of LTP behavior has been achieved in recent years with models employing Maxwellian EEDFs, but the future of LTP technology lies in "predictive plasma design", through the 'tuning' of the energy dependence of non-equilibrium EEDFs to optimize the mix of gas phase neutral and charged particle species for each process [29, 38, 39, 40, 41, 42, 43, 44, 45], as exemplified in Fig. 1.5 and 1.6.

The goal of "predictive plasma design" will involve models that capture the complex physical processes that underly plasma behavior, provided those models can accurately predict subtle

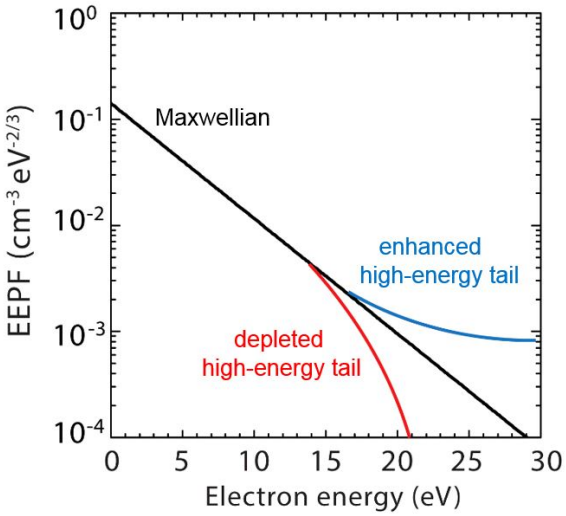

Figure 1.4: EEPF for Maxwellian distribution is a straight line. And non-Maxwellian distributions have more complicated shapes which affect the rates of electron collision driven reactions.

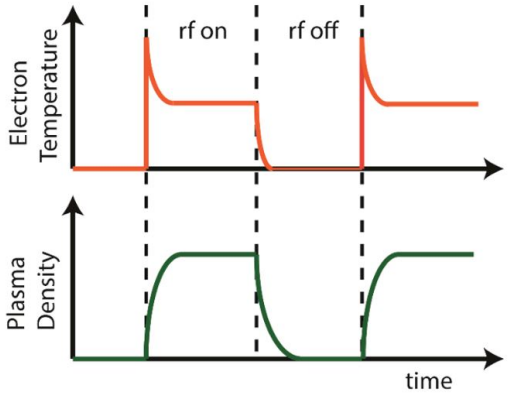

Figure 1.5: An example of tunning the EEDF for process control is to use time-modulation of RF power which generates plasma to control plasma chemistry [38].

changes in nonequilibrium particle energy and velocity distributions. This direction has been highlighted in two recent reports examining the significance of low temperature plasmas and laying out future strategies: the National Academy sponsored Plasma 2010 decadal report, and a more detailed examination of low temperature plasma science sponsored by the U. S. Department of Energy Office of Fusion Energy Science [46, 47]. Despite remarkable advances in numerical techniques and computing power over the last few decades, efficient multidimensional modeling/simulation of LTP discharges has remained a considerable challenge [48].

Diagnostics are essential in the continued development of such predictive models and simu-

Figure 1.6: Incident auxiliary high-energy electrons to improve etching profile by neutralizing positive charge on sidewalls [39].

lations, by identifying the relevant physical processes, and in confirming that models accurately represent that behavior. Furthermore, diagnostics that could be easily and cheaply implemented on plasma process tools would allow real-time monitoring of the EEDF, which in combination with an accurate simulation would provide a feedback loop that would enable tuning of the EEDF to optimize process results. Methods for accurately measuring the EEDF are thus of great importance to understanding and quantifying plasma kinetics essential to plasma technology outcomes, and to process monitoring and control. For low pressure plasmas, optical diagnostics offer an alternative to the most common method to measure the EEDF, "Langmuir" or electric probes, physically inserted directly into the plasma [13, 49, 50]. Langmuir probes may perturb plasma conditions, introduce contaminants, and higher energy electrons sometimes critical to discharge behavior may not be accurately represented due to signal-to-noise limitations. In contrast, optical diagnostic methods make use of the spectrum of light emitted by the plasma to non-invasively probe the EEDF over a wider range of electron energies [51, 52, 53, 54].

Previously, our group has successfully measured Maxwellian EEDFs and non-Maxwellian EEDFs using an OES diagnostic in argon ICPs over a wide range of pressures (1-50 mTorr) and discharge

powers (20-1000 W). Both the electron temperature and the shape of the EEDF, i.e., the degree the distribution departs from a Maxwellian were observed to vary with the discharge pressure, and independent control of these two properties was not achieved.

The intent of this thesis is thus to develop optical emission spectroscopy (OES) based diagnostics for non-Maxwellian EEDFs with enhanced high-energy tails, and characterize the capabilities and limitations of such OES diagnostics. In order to produce the non-Maxwellian EEDFs, an auxiliary electron source is installed on a conventional ICP source to produce plasmas in which the shape of the enhanced tail EEDF could be varied systematically over a wide range. Using this modified ICP source, relatively independent control of the low energy range and high energy range of the EEDF can be achieved. The emission model which connects a trial EEDF into the predicted emission spectrum is described in Chapter 2. The model requires an EEDF described as an analytical function characterized by a number of free parameters (i.e., T_e and n_e for a Maxwellian EEDF). By minimizing the difference between the observed and modeled spectra, the values of the parameters can be extracted from the OES diagnostic. Chapter 2 describes the functional forms used in this work to describe non-Maxwellian EEDF with enhanced tails. The number of parameter values that can be reliably measured and the fidelity of the resulting EEDF improve with the number of emission lines used in the fitting process. Chapter 5 presents the limited results using only Ar emission lines. Chapter 6 and 7 present more advanced results using a variety of Ar, Ne and He emission lines. The emission measurements in Chapter 5-7 were obtained using a high-resolution scanning monochromator (described in Chapter 3). Plasma processing tools used in IC fabrication, however, are typically fitted with *low-resolution*, compact spectrometers. Chapter 8 describes the attempts to apply the OES diagnostic to measurements with a similar low-resolution spectrometer.

Chapter 2

Determining plasma parameters using optical emission spectroscopy

Optical emission spectroscopy (OES) is a well established plasma diagnostic tool [52, 54]. Emission spectra from the plasma are recorded to provide insight into plasma processes and plasma parameters. For example, as shown in Fig. 2.1, in Ar spectra, there are many emission lines that can be used to provide information about the plasma state. Several applications of OES for plasma processing have been reported. For example, OES is widely used as a real-time 'end-point' monitor to detect emission changes that signal completion of plasma etching steps in the fabrication of integrated circuits [55]. The focus of this chapter is emission models for rare gas plasmas used to determine the electron energy distribution function (EEDF) from recorded emission spectra. The procedure of determining EEDFs is briefly illustrated in Fig. 2.2. The emission model predicts the intensities of rare gas emissions by combining an assumed EEDF with other required atomic data and plasma parameters. Many different trial EEDFs, i.e., $f_1(E)$, $f_2(E)$ and etc., are used to calculate corresponding emission spectra. These predicted emission spectra are compared with the measured spectra to calculate their χ^2 differences, i.e., χ_1^2, χ_2^2 and etc.. The minimum χ^2 value, for example, χ_i^2 gives $f_i(E)$ which is the best approximation of the EEDF in the plasma. This optical diagnostic is a non-invasive alternative to Langmuir probes and is not affected by many factors that complicate interpretation of Langmuir probe measurements.

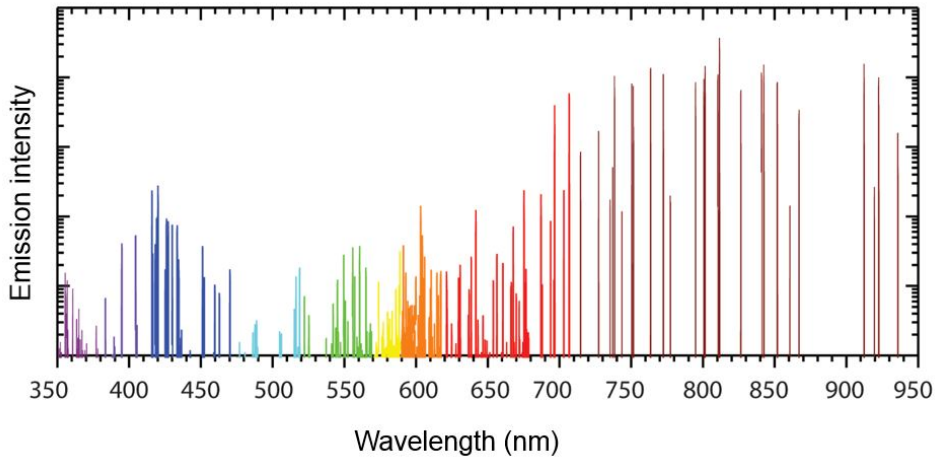

Figure 2.1: Emission intensities measured as a function of wavelength for a 600 W, 25 mT, Ar inductively coupled plasma (ICP).

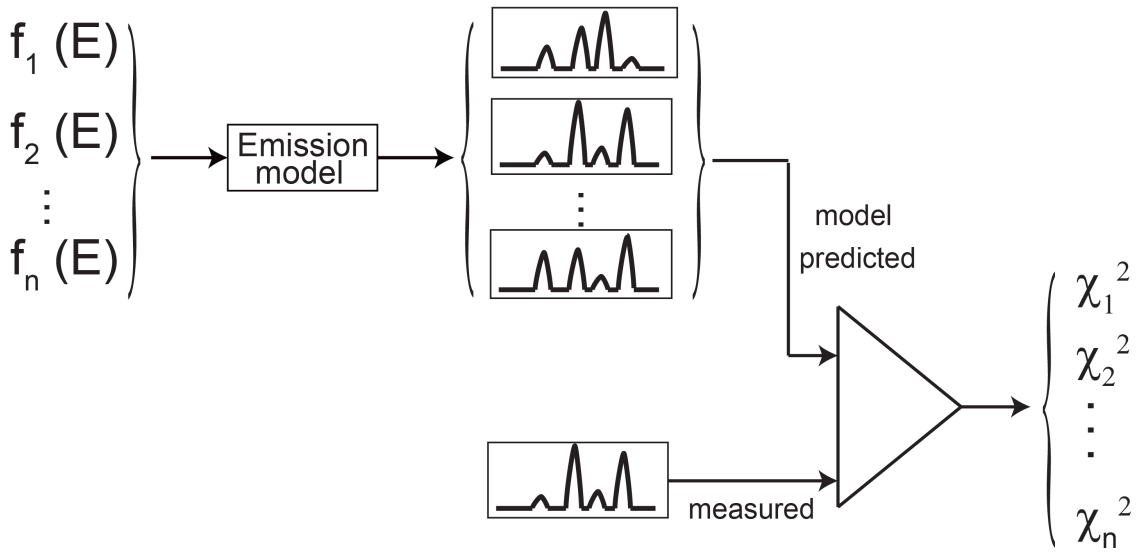

Figure 2.2: Spectra are computed for many different trial EEDFs using the emission model. The values of χ^2 are compared to determine the minimum, χ^2_m=min(χ^2_1, χ^2_2...χ^2_n), and the "best fit" EEDF is identified as the corresponding distribution f_m(E).

2.1 Relating plasma parameters to emission intensity

To extract plasma parameters of interest from emission spectra of rare gas plasmas, one first builds up an emission model to estimate relative emission intensities of a set of spectral lines by considering the dominant production and depopulation processes of emitting states. As illustrated in the partial atomic energy level diagram for argon in Fig. 2.3, atoms or ions in lower energy levels, including the ground state and metastable levels, undergo electron-impact collisions and photon absorption, leading to the production of photon-emitting electronically excited states. Following an inelastic electron collision, an atom may be directly excited into an emitting state or cascade from higher-lying levels. Once particles are excited into an emitting state, they may decay to lower levels by electron-impact de-excitation or by spontaneous radiative decay, the latter resulting in emitted photons. The probability for an atom in level-i to radiatively decay to a particular lower level-j versus all the other lower levels is characterized by the $i \rightarrow j$ branching fraction, for which numerical values have been published in many cases. In addition, the population of emitting states can be affected by other kinetic reactions, such as collisions between heavy particles (i.e., atom-atom, atom-molecular), recombination between electrons and ions, etc. However, for plasmas at lower pressures or lower ionization fraction of interest here, the contributions from these reactions are typically negligible.

The emission intensity can be quantified by an emission model that accounts for the populating and depopulating processes of the emitting state. First, consider electron-impact collisions which dominate atomic excitation into radiative levels. The probability for excitation into a particular energy level varies with the electron energy and is characterized by its electron-impact excitation "cross section," $Q(E)$. As an example, Fig. 2.4 shows argon *optical emission* cross sections (which include the effects of the branching fraction and cascades from higher-lying states) for a variety of emission lines with excitation originating from both the ground state and the metastable levels, respectively [59]. The energy thresholds for excitation from the ground state ($\sim$13 eV) are much higher than those from the metastable levels ($\sim$2 eV). Therefore, the average energy of electrons contributing to ground state excitation is much higher than in the case of excitation from metastable levels. Also, the energy thresholds for excitation into the Ar^+ emitting states from the neutral ground state ($\sim$35 eV) are much higher than those into the neutral emitting states ($\sim$13 eV).

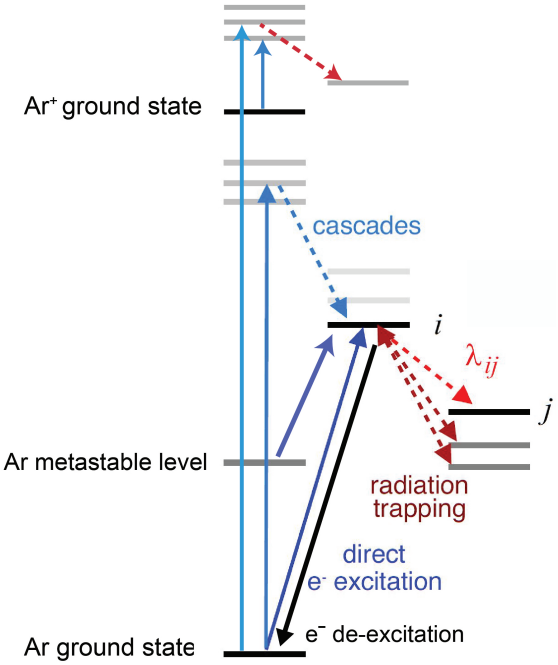

Figure 2.3: Partial energy level diagram for argon, showing populating and depopulating processes relevant to plasma emissions.

The excitation cross sections of Ar have been well studied and can be found in Ref. [57, 60, 58, 61, 62, 63]. In addition, there are differences in energy levels between rare gases (Fig. 2.5). For example, the emitting states of He and Ne are at much higher energies above the ground state which results in larger excitation threshold energies (∼19 eV for Ne and ∼23 eV for He) compared with Ar (∼13 eV). The Ne and He excitation cross sections have also been studied and presented in Ref. [64, 65, 66, 67, 68, 69, 70].

Integrating the product of the cross section and the EEDF over electron energy yields the electron impact excitation rate [59],

$$k_{ij}^{k} = \sqrt{\frac{2}{m_e}} \int_0^\infty Q_{ij}^{k}(E)\, f(E)\, \sqrt{E}\, dE \qquad (Q_{ij}^{k} = 0, \text{ for } E < E_{th}), \tag{2.1}$$

where E is the electron energy, $f(E)$ represents the EEDF and E_{th} is the excitation threshold energy. The cross section vanishes for electron energies below the excitation threshold. For low-temperature plasmas studied in this thesis, which typically have electron temperature in the 1 to 10 eV range, differences in the "tails" of EEDFs become significant in an energy range that

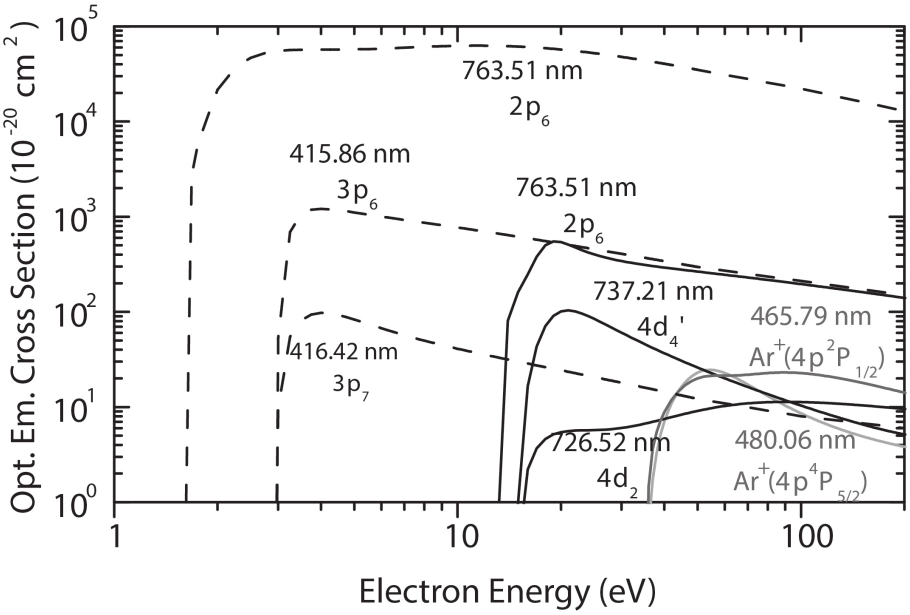

Figure 2.4: Argon optical emission cross sections, $Q(E)$ for electron impact excitation from the ground state (solid lines) [56] and from the $1s_5$ metastable level (dashed lines) [57, 58]. Excitation into $3p^5 4p$ levels (i.e. the $2p_6$ level) from the $1s_5$ metastable level have the lowest excitation thresholds of around 1.5 eV. Excitation into $3p^5 5p$ levels from the $1s_5$ metastable level have onset energies around 3 eV. For excitation from the ground state, the threshold energies are in the 13-15.5 eV range for excitation into neutral levels. Excitation into Ar^+ excited levels from the neutral ground state (shallow lines) have much larger threshold energies (35 eV).

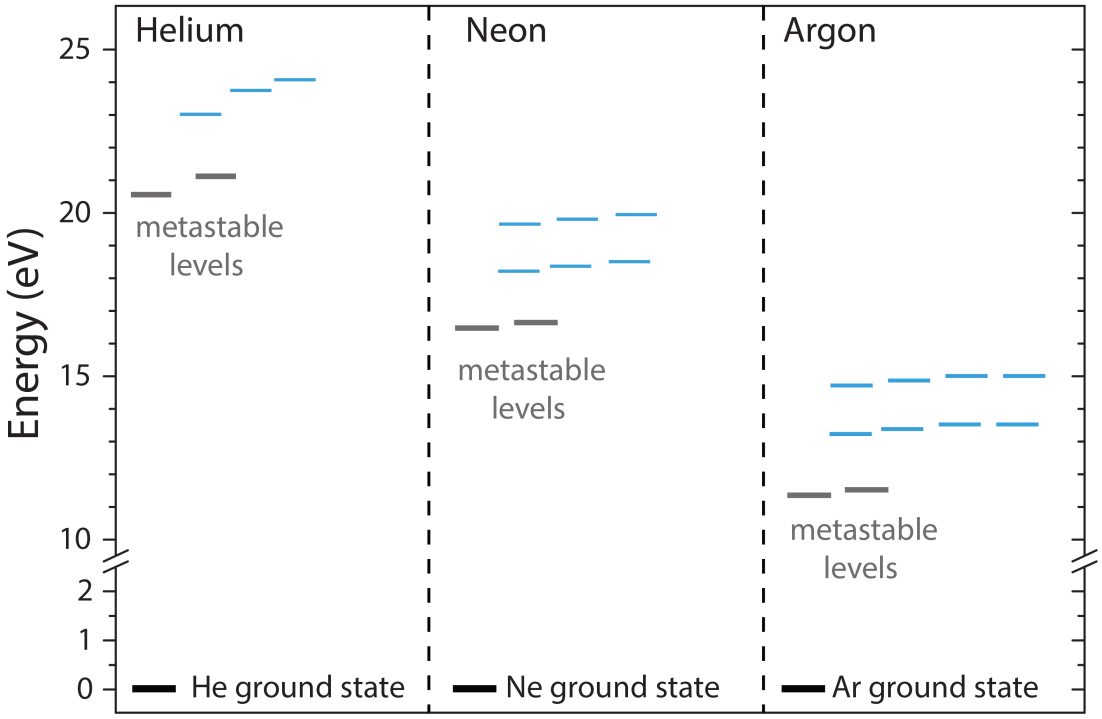

Figure 2.5: Partial energy level diagrams for Ar, Ne, He. The energies of Ne and He emitting states (blue) and metastable levels are higher than those in Ar.

include the threshold energies for a number of electronic excitation transitions for rare gases (see Fig. 2.6, in which EEDFs are represented as electron energy probability functions (EEPF), defined as $f(E)/\sqrt{E}$). Therefore, rates for transitions with higher electron energy thresholds are more sensitive to the shape of the high energy region of the EEDF. However, the determination of EEDFs by making use of the rare gas transitions is only applicable to the plasmas in which the EEDF tails fall close to the set of excitation threshold energies of these transitions. The situation is different, however, for plasmas with much lower or higher electron temperatures. For the case of high electron temperatures e.g. the plasmas found in stellar interiors and in fusion experiments [16], there is very little difference in the number of electrons which can contribute to these rare gas transitions, and the emission spectra are therefore relatively insensitive to changes in EEDF shape of the magnitude under consideration here. At the other extreme, very low electron temperature (<1 eV) plasmas, such as those found in plasma afterglows, have negligibly small excitation rates,

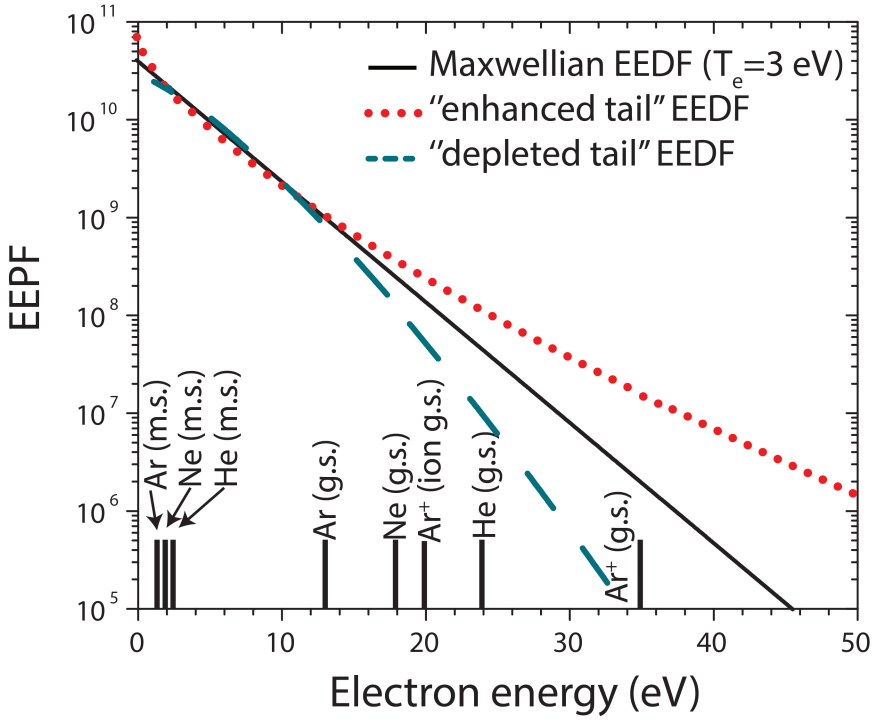

Figure 2.6: Excitation thresholds of selected emitting states of Ar, Ne, He, Ar^+ from the neutral ground state (g.s.), metastable levels (m.s.) and the ion ground state (ion g.s.). The excitation rate depends on the excitation threshold and the electron population with energies above the threshold. For low-temperature plasmas, excitation rates for transitions with higher threshold energies will therefore be more sensitive to differences in the "tail" of the EEDF.

so that resulting emission intensities may be too low for meaningful analysis.

Another mechanism for populating an emitting state is the absorption of a photon by an atom in a lower lying state, essentially the reverse of the emission process. As a result, an emitted photon will in some cases be absorbed by an atom as it travels thro ugh the plasma. The electronically excited atom produced by photon reabsorption may subsequently emit a photon, but the wavelength of the emission may be different from that of the absorbed photon, with the distribution of wavelengths following the branching fraction for the upper state. Because the absorption/emission cycle can repeat multiple times, it is referred to as "radiation trapping," and will produce a relative distribution of detected emission intensities that differs from the branching fraction prediction. The degree of radiation trapping depends on the concentration of atoms in the lower energy state associated with the transition, which is typically a metastable or resonance level state. By compar-

ing measured relative intensities of a family of wavelengths associated with a particular emitting state with the predictions of an emission model including the effects of radiation trapping, the concentrations of metastable and resonance levels can be estimated.

The last mechanism considered here is electron impact de-excitation of an upper state, which causes a transition out of the excited state without photon emission. The likelihood of this mechanism depends on the radiative lifetime of the upper state as well as the electron concentration. If the electron density is sufficiently high that the rate for this quenching mechanism is non-negligible compared to radiative decay, it will suppress emission intensities relative to excitation rates. When the effects of electron quenching are included in the emission model, it may be possible to determine the value of electron density as that for which predicted relative emission intensities match measured values. In practice, transitions are selected with upper states of significantly different radiative lifetimes to maximize variation in the quenching contribution. Also, by examining a set of emission lines terminating on a common lower state, the effect of electron quenching can be decoupled from that of radiation trapping.

In the following sections, several previously reported emission models are reviewed. Among these OES methods, the one developed by Boffard *et al.* using an "extended corona model," also used in this thesis work, is described in detail, including the mathematical representation of the emission model, and the procedure to determine plasma parameters.

2.2 Overview of plasma emission models

In this section, several published emission models are summarized, with a focus on the choice of populating and depopulating processes included. The fundamental principles, applications and limitations of these emission models are discussed, and provide context for the model selected for use in this proposed study.

Corona Model. A simple emission model developed to predict plasma emissions is the so-called corona model [71]. The corona model is used to estimate emission line intensity ratios as the ratios of excitation rates originating only from the argon ground state. The resulting quantity is a function of electron temperature T_e only (when a Maxwellian EEDF is assumed), since the dependencies on

the electron density and the ground state density are removed by considering ratios.

For example, Hope *et al.* [72] employed an Ar/Ar^+ line ratio to estimate the electron temperature (T_e). Due to the difference in excitation threshold energy from the neutral argon ground state between the neutral Ar and Ar^+ emission lines (Fig. 2.6), this line ratio is a strong function of T_e compared to those formed by two neutral lines, for which the difference in excitation threshold energies is much smaller.

The corona model is valid only for plasmas at low pressure and low ionization fraction. This is because, under these conditions, the number density of atoms is low enough to safely neglect excitation processes driven by atom-atom and ion-atom collisions. Furthermore, the low ionization fraction ensures the probability of electron impact de-excitation processes is much lower than de-excitation by spontaneous emission and can be neglected. Even under optimal plasma conditions, the corona model accurately estimates emissions from lower-lying levels dominated by ground state excitation, but fails for excited levels with significant metastable contribution and high-lying states which have increased electron collisional de-excitation, thus limiting which emission lines for which the corona model is valid. The corona model is typically used to estimate the electron temperature by assuming a Maxwellian distribution, although for T_e values in the 1-10 eV range of interest here, results are sensitive only to the electron population in the high energy 'tail' of the distribution. Therefore, although its simplicity is attractive, the corona model is of limited use in determining non-Maxwellian EEDFs because it is insensitive to the population of electrons with energy below the threshold for inelastic excitation from the ground state. A comprehensive review of OES with the corona model can be founded in Ref. [73].

Extended Corona Model. To describe more complicated plasma dynamics affecting emitted spectra, the corona model can be extended by including excitation processes from argon metastable levels and de-excitation by collisions with electrons [59]. The extended corona model is used to calculate emission intensities as

$$\Phi_{ij} = C\ R_{ij}\ n_e\ \gamma_{ij}^{\mathrm{de-ex}} \sum_k n_k\ k_{ij}^k\ , \tag{2.2}$$

where i and j are the upper and lower levels, respectively, of the transition, C is an overall normalization factor, R_{ij} is a radiation trapping correction factor, which depends on the number densities of atoms in absorbing levels. $\gamma_{ij}^{\mathrm{de-ex}}$ is a correction factor for electron impact de-excitation. n_k represents the number density of atoms in the lower level k and k_{ij}^k is the excitation rate, in which the EEDF dependence is implicitly contained (Eq. 2.1). In the extended corona model, the index k covers both the ground state and the four $3p^5 4s$ metastable and resonance levels; their determination is discussed in Section 2.3.2. By considering only relative emission intensities, the dependence on n_e and C is eliminated as they are common factors. With known or estimated number densities of lower states, line ratios predicted by the extended corona model are functions of the EEDF through its effect on the excitation rate k_{ij}^k. Due to the large difference in electron energy threshold between excitations out of the ground state (∼13 eV) and metastable levels (∼2 eV), the excitation rates from different initial states include contributions from different ranges of electron energy (Fig. 2.4), including, in the case of excitation from metastable levels, much lower electron energies compared to the corona model. The extended corona model thus allows determination of non-Maxwellian EEDFs, as reported by Boffard *et al.* [59, 74, 75]. The extended corona model is valid for argon-containing plasmas at low pressures, for which heavy particle collisions (atom-atom, atom-ion) and recombination of electrons and ions are negligible. One limitation of this method is that since the metastable atoms play an important role, the uncertainty in T_e or the EEDF can be high when the metastable concentration is low, as occurs at low discharge power levels or due to quenching by molecular gases in argon-molecular gas mixtures [76].

Trace Rare Gas OES. The extended corona model is applicable to all rare gases (He, Ne, Kr, Ar and Xe) for which excitation cross sections and other atomic parameters are known. A diagnostic technique known as trace rare gases optical emission spectroscopy (TRG-OES) has been developed by Malyshev and Donnelly [77, 78, 79] based on such an emission model. In particular, a small amount (∼5% of total feed gas) of He, Ne, Ar, Kr and Xe with known concentrations are added to the reactive gases. Computed intensity ratios formed by emission lines from multiple rare gases are compared to measured values to determine the EEDF or T_e via its contribution to excitation rates. Due to the low metastable densities of rare gases at these low partial pressures, radiation trapping can be ignored. Unlike the emission model developed by Boffard *et al.*, the metastable densities

of rare gases, which are important inputs to determine the EEDF, are obtained by modeling their creation and loss rate balance. As displayed in Fig. 2.6, due to the wide range of excitation threshold energies for ground state excitation of rare gases (19 eV, 13 eV, 11 eV and 9.5 eV for Ne, Ar, Kr and Xe respectively), different energy ranges of the high energy 'tail' of the EEDF can be sampled. Therefore, TRG-OES can in principle measure non-Maxwellian EEDFs with more complex structures compared to the emission model developed by Boffard *et al.*. On the other hand, since multiple rare gases are involved, the determination of metastable densities by modeling depends on many species and kinetic reactions, which may introduce inaccuracies. In addition, considering the small concentrations of the trace rare gases, a high resolution spectrometer system is required to measure intensities of the weak emissions from rare gases.

Collisional Radiative Model. At higher pressure and high ionization fraction, the extended corona model is invalid since several other processes, including ionization by electron collisions, heavy-particle collisions (ion-atom, atom-atom) and recombination between electrons and ions may depopulate excited states. For this case, plasma emissions may be predicted using a "collisional radiative model" (CRM) which adds the kinetic reactions mentioned above to the extended corona model [51]. In argon CRMs, the intensity ratios are calculated as the ratios of radiative level concentrations. The population ratios as functions of T_e and n_e are estimated from the rate balance equations of states, which contain the dominant production and depopulation processes. For example, Iordanova *et al.* [80] considered the population of a number (14) of argon excited levels in the CRM, which have important contributions to the radiation terms, by solving their creation-loss rate balance equations. T_e and n_e were obtained simultaneously by comparing observed line-intensity ratios with those computed from the CRM model with T_e and n_e as adjustable parameters.

Discussion. Considering the argon-containing plasmas (1-30 mTorr, weakly ionized) studied in this thesis work, the extended corona model is appropriate to estimate plasma emissions and determine plasma parameters. Both the extended corona model developed by Boffard *et al.* and TRG-OES method reviewed above can be used to determine non-Maxwellian EEDFs. In principle, TRG-OES may resolve more complex EEDF structures through the use of a large number of available emission lines with different threshold energies, but accuracy may be compromised due to

the large number of adjustable parameters. However, OES measurement of metastable density, introduced by Boffard *et al.*, is not susceptible to modeling uncertainties associated with TRG-OES. In addition, for applications using a low-resolution spectrometer, i.e., real-time OES measurements (Sec. 8.1), TRG-OES is not suitable since the weak emissions from rare gases cannot be measured with sufficient accuracy. In contrast, the OES method developed by Boffard *et al.* can still work since in the Ar ($3p^5 4p \rightarrow 3p^5 4s$) transition array, there are a number of intense and isolated emission lines that can be measured with a low-resolution spectrometer.

2.3 Determination of plasma parameters using extended corona model

In this section, procedures for determining plasma parameters, including the EEDF or T_e, metastable densities and n_e, using the extended corona model are described.

2.3.1 Determination of EEDFs

The extended corona model predicts relative intensities of the rare gas atom emissions by combining an assumed EEDF with known excitation cross sections [57, 60, 58, 61, 62, 63, 64, 65, 66, 81, 67, 68, 69, 70] and the number densities of species excited, including the ground state and metastable levels, as captured in Eqs. 2.1 and 2.2. The ground state density is estimated from the gas pressure and temperature [59] and the metastable and resonance densities are determined from the emission spectra, based on the degree of radiation trapping, to be described in Section 2.3.2. With these values as model inputs, the EEDF or T_e is determined as that which minimizes the difference between computed and measured spectra.

Mathematical representation of EEDFs. To calculate spectral intensities using the emission model, a mathematical representation of the EEDF is required. EEDFs are commonly described by functional forms with one, two or more free parameters. In thermodynamic equilibrium, the EEDF follows a Maxwell-Boltzmann (Maxwellian) distribution form:

$$f_{\mathrm{e-Max}}(E) = n_e \frac{2}{\sqrt{\pi}} T_e^{-3/2} \sqrt{E}\, \mathrm{e}^{-E/T_e} \,, \tag{2.3}$$

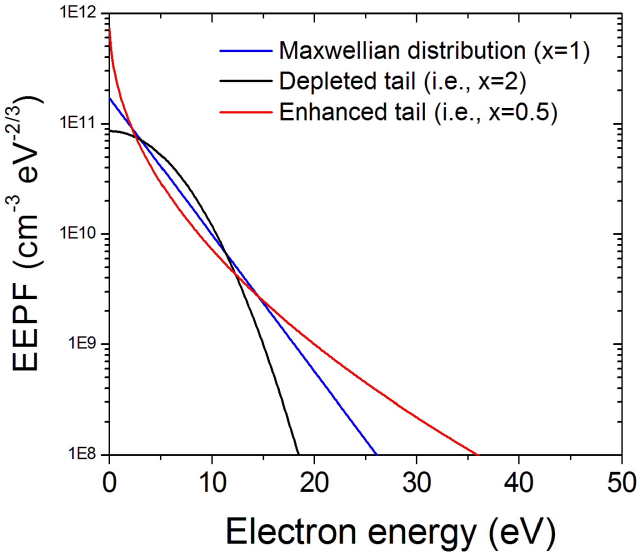

Figure 2.7: Examples of EEDFs that can be captured with the x-form.

where the EEDF $f_{\mathrm{e-Max}}$ is characterized by two parameters, the electron temperature, T_e and the electron density, n_e. Plasmas employed in applications, however, typically are non-equilibrium in the energy distributions of their charged constituents [32, 33, 34]. To faithfully represent non-Maxwellian electron distributions, a more complicated expression is required. A widely used functional form is the three parameter (x, T_x, n_e) form [82, 83],

$$f_{\mathrm{x}}(E) = c_1(x)\, n_e\, T_x^{-3/2}\, \sqrt{E}\, \mathrm{e}^{-c_2(x)(E/T_x)^x}\ , \tag{2.4}$$

where x is a parameter affecting the energy dependence of the EEDF, T_x is an effective electron temperature, defined as 2/3 of the average electron energy, and n_e is the electron density. A Maxwellian distribution corresponds to the case of x=1 and a Druyvesteyn distribution which has a 'depleted' high energy tail relative to a Maxwellian distribution [13] corresponds to the case of x=2. As illustrated in Fig. 2.7, distributions with 'enhanced' tails compared to a Maxwellian are represented when x<1, and 'depleted' tails when x>1. The 'x-form' has been previously used to represent EEDFs with depleted tails in argon inductively coupled plasmas [59, 74].

In this thesis work, OES diagnostics for EEDFs with enhanced tails relative to a Maxwellian distribution are developed. Therefore, a mathematical form which is suitable to representing EEDFs

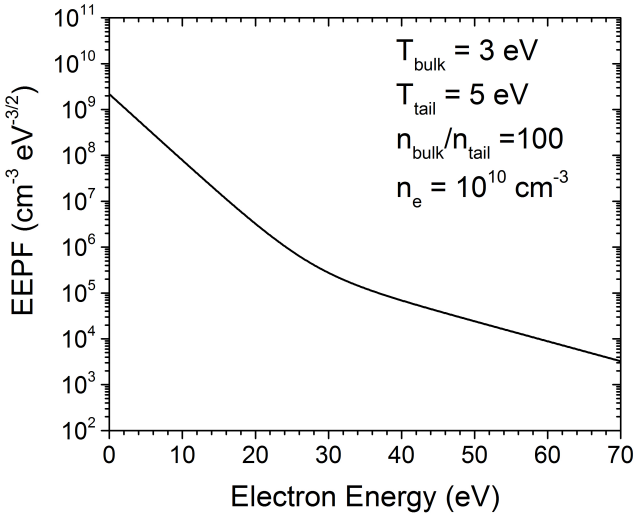

Figure 2.8: A sample EEDF represented by the bi-Maxwellian distribution function.

with enhanced tails is essential. There are several mathematical expressions that are candidates. In principle, the 'x-form' with x<1 can represent enhanced EEDF tails. However, the EEDF generated using x<1 results in an even larger enhancement in the 'bulk' EEDF (Fig. 2.7), which is not consistent with observation [59, 74, 35, 36]. Another possibility is the 'bi-Maxwellian' distribution (Fig. 2.8). The bi-Maxwellian EEDF is represented as the sum of two Maxwellian distributions, with the low energy or 'bulk' electron population and higher energy 'tail' of the distribution characterized by different respective temperatures (T_e^{bulk}, T_e^{tail}). A third parameter $n_{\text{bulk}}/n_{\text{tail}}$ is needed to describe the relative density of the bulk and tail populations [84]. A forth parameter n_e sets the overall magnitude of the EEDF. In addition, there are some other possible forms for representing the enhanced EEDF 'tail', such as a Gaussian 'bump' or a rectangular tail (Fig. 2.9). However, since the exact shape of the EEDFs in the plasma being observed are unknown, instead of the mathematical forms listed above, it is advantageous to use a mathematical form for the EEDF that can take different shapes by varying the value of a parameter in the equation.

Through probe measurements and other evidence, 'x-form' is adequate for representing the 'bulk' EEDF [35, 36, 17, 85]. The focus here is therefore a mathematical representation of the tail distribution, which will be added to the 'bulk' distribution to represent tail enhanced EEDF.

Here we introduce a functional form called 'log-normal distribution' [86] to represent enhanced

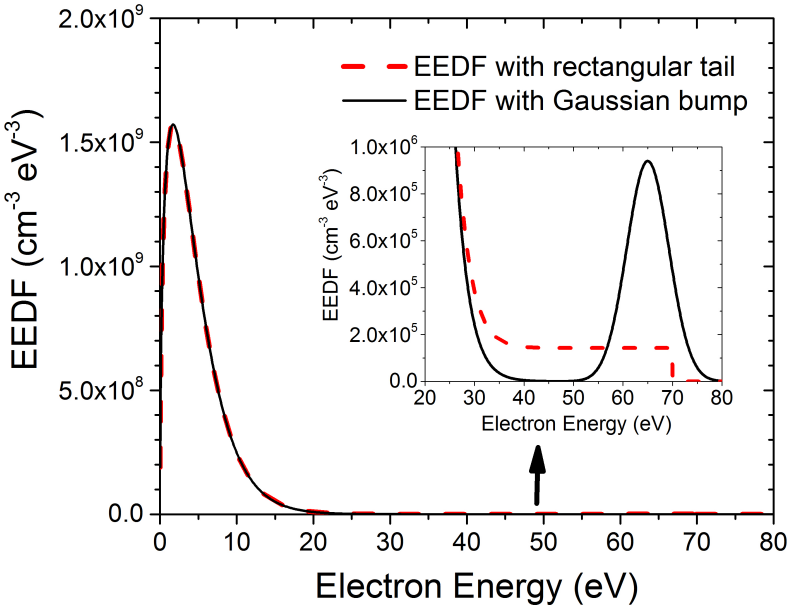

Figure 2.9: Enhanced EEDF tails represented by a Gaussian 'bump' and a rectangular shape. The embedded plot is a zoomed in view of the high energy portion of the EEDFs.

EEDF tails,

$$f_{\text{tail}}(E) = f_{\log-\text{n}}(E) = n_{\text{tail}}\, N\, \text{e}^{-(\ln(\text{E}-\text{E}_{\text{cut}})-\text{s})^2}\ , \tag{2.5}$$

where s is a parameter affecting the shape of the high energy tail, n_{tail} represents the tail electron density and E_{cut} is the cutoff energy of the tail. As illustrated in Fig. 2.10, by adjusting the shape parameter s, the log-normal distribution can be used to describe a wide range of different EEDF tail shapes, including a high energy 'bump' (Fig. 2.10a), a near-Maxwellian tail (Fig. 2.10d), and the shapes in between (Fig. 2.10b and c).

The standard log-normal probability function is normalized to one when integrated from $-\infty$ to $+\infty$. For describing EEDFs, the lower limit of the electron energy integration is limited to zero. Therefore, to have $\int_0^{E_{\text{cut}}} f_{\text{tail}}(E)\, dE = n_{\text{tail}}$, an additional normalization factor N is required in Eq. 2.5. This can be approximated as

$$N \approx \frac{1.79}{1.7724\ (\text{E}-\text{E}_{\text{cut}})} \text{e}^{-((s-0.83)/1.26)^2}\ . \tag{2.6}$$

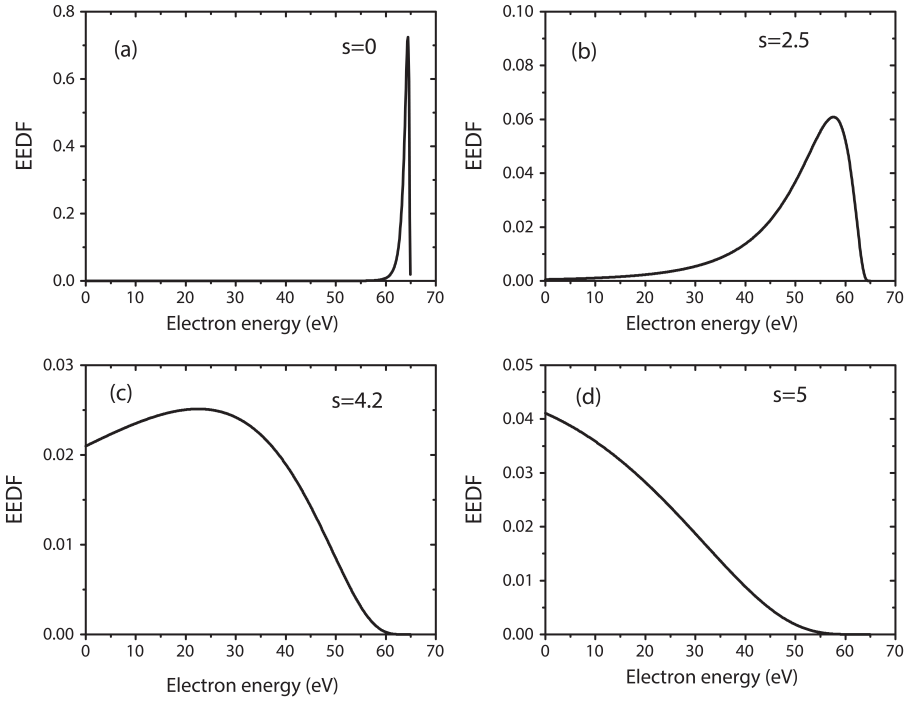

Figure 2.10: Examples of EEDF tail structures generated by the log-normal distribution by adjusting the shape parameter s.

Determination of the free parameters in mathematical form of EEDF. With an assumed mathematical representation of the EEDF, the free parameters are determined by minimizing the difference (χ^2) between the model predicted relative intensity, referred to as LR^{model} (LR = "line ratio"), to the observed one referred to as LR^{obs} [59, 74, 75]. For a particular choice of trial EEDF, the goodness of fit value, χ^2, is calculated as

$$\chi^2 = \sum_i \left(\frac{LR_i^{\text{obs}} - LR_i^{\text{model}}}{\sigma \, LR_i^{\text{obs}}} \right)^2 , \tag{2.7}$$

where σ refers to the estimation of the error of emission measurements, and the differences of all the line ratios are summed.

Note that there is a trade-off when selecting the mathematical representation of the EEDF; using a mathematical representation with more parameters allows the description of more complex EEDF shapes, but reduces the effectiveness of the fit process. In practice, when using a Maxwellian form, the electron temperature, T_e is the only free parameter determined from the emission model

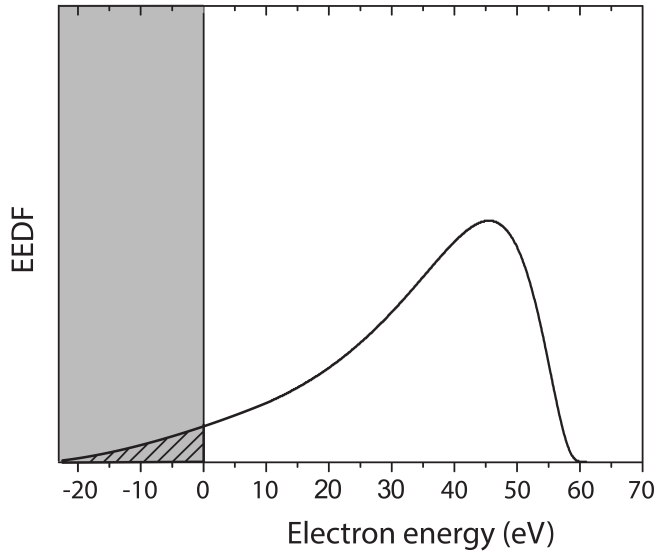

Figure 2.11: A sample EEDF tail represented by the log-normal distribution. For this value of the shape parameter s, the function extends to negative electron energy, and this range is excluded in normalization.

analysis (n_e is determined from the line ratio method as described in a later section). Fig. 2.12 illustrates the variation in the goodness of fit parameter as a function of the assumed electron temperature at two different source pressures. For the 15 mTorr data, the reduced χ^2 function has a deep, narrow minimum at 2.4 eV. As a result, the extracted value of T_e is well localized about the value of 2.4 eV with an estimated uncertainty of about ± 0.1 eV (within 10% of the minimum χ^2 value). In contrast, the curve for the 15 mTorr data is more shallow, leading to a greater uncertainty in the extracted T_e, with an approximate uncertainty range of 5.0 to 6.3 eV (within 10% of the minimum χ^2 value).

When fitting more than one free parameter, the possibility arises that there is either no solution, or that the uncertainty in the fitted parameters is high. For the two free parameters T_x and x in the 'x-form' representation, as illustrated in Ref. [59, 74], incorporating the Ar ($3p^5 4p \rightarrow 3p^5 4s$ and $3p^5 5p \rightarrow 3p^5 4s$) transitions to the emission model is generally sufficient to constrain both x and T_x. For example, Fig. 2.13 illustrates the variation in the goodness of fit parameter as a function of the assumed T_x and x for a 15 mTorr, 400 W Ar ICP plasma. The extracted value of T_x is localized about the value of 3.3 eV with an estimated uncertainty of about ± 0.3 eV (within 10% of

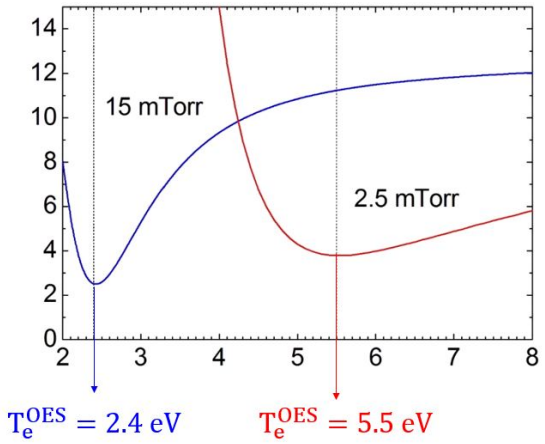

Figure 2.12: Plot of χ^2 values for OES analysis assuming a simple Maxwellian EEDF for 600 W, 2.5 and 15 mTorr ICPs [59]. Vertical lines correspond to best fit values of T_e.

the minimum χ^2 value), and the value x is localized about the value of 1.6 eV with an estimated uncertainty of about ± 0.3 (within 10% of the minimum χ^2 value). Sometimes there is not enough information in the emissions to *simultaneously* constrain the values of both x and T_x. In those cases, the effective electron temperature T_x is regarded as the only variable while the value of x is held fixed, e.g. $x = 1.2$ (which indicates a depleted high energy tail in the EEDF), determined by other means. However, when using a bi-Maxwellian form (four free parameters), the EEDF cannot typically be uniquely determined from the measurable Ar $3p^5 4p$ and $3p^5 5p$ emissions because the uncertainties of the four free parameters (T_e^{bulk}, T_e^{tail}, $n_{\text{bulk}}/n_{\text{tail}}$, n_e) are excessively large.

In our 'bulk' +'tail' EEDF form, there are six free parameters including three free parameters in the 'x-form' distribution and three free parameters in the log-normal distribution. It is impossible to uniquely determine all 5 free parameters simultaneously.

A two-step process for determining the EEDF has therefore been developed. Specifically, diagnostics are first used to measure the 'bulk' EEDF which is described using the 'x-form' representation. Second, another set of diagnostics are used to determine the tail distribution after accounting for the 'known' bulk contributions. For the three free parameters in the log-normal function, one is typically fixed at a selected value based on physical reasoning. The other two are regarded as variables and determined from the analysis of emission intensities. When determining the 'x-form' distribution, we can use the Ar ($3p^5 4p \rightarrow 3p^5 4s$ and $3p^5 5p \rightarrow 3p^5 4s$) emissions by assuming exci-

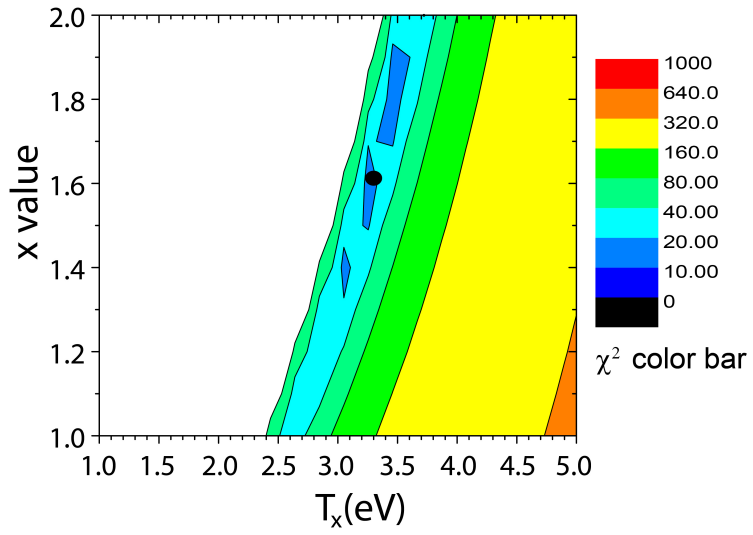

Figure 2.13: Contour plot of χ^2-values for OES analysis of 15 mTorr, 400 W Ar ICP (including emissions from both $3p^5 4p$ and $3p^5 5p$ levels). Solid dot represents the best-fit (T_x, x) value.

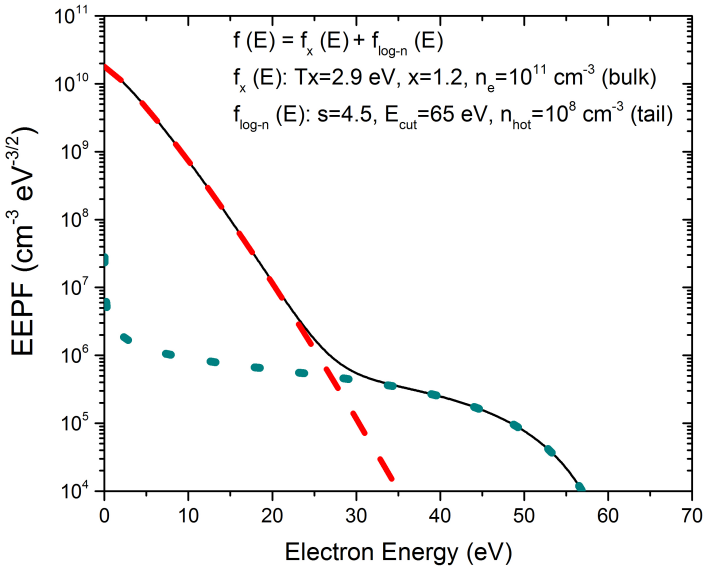

Figure 2.14: A sample EEDF described the sum of the 'x-form' and the log-normal distribution (solid line). The x-form (dashed line) and the log-normal distribution (dotted line) are also displayed.

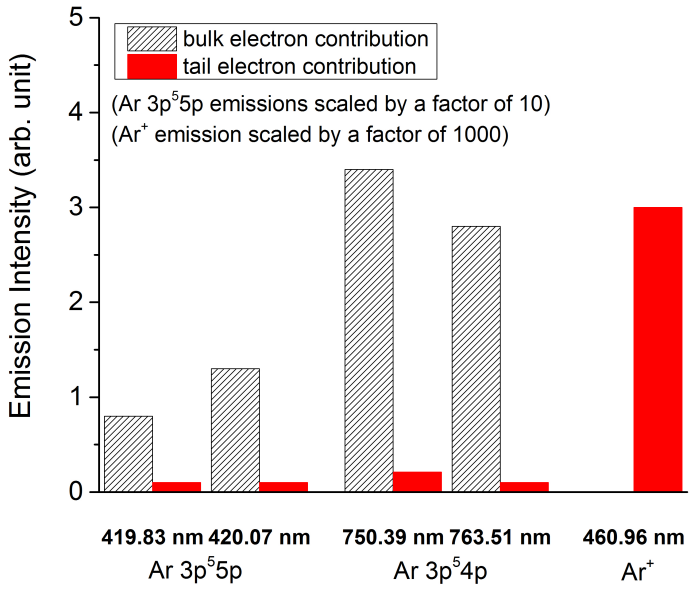

Figure 2.15: Emission intensities of selected Ar ($3p^5 4p \rightarrow 3p^5 4s$ and $3p^5 5p \rightarrow 3p^5 4s$) and Ar^+ emissions contributed by the 'bulk' electron and the 'tail' electron.

tation rates are dominated by contributions from collisions involving only 'bulk' electrons. A test has been devised to evaluate the validity of this assumption, in which the contributions from the electrons in the 'bulk' and the 'tail' distributions, respectively to some Ar emission lines, including selected Ar $3p^5 4p$, $3p^5 5p$ and Ar^+ emissions, have been calculated using the emission model with a sample EEDF represented by the 'x-form'+log-normal distribution form (Fig. 2.14). The parameters in this sample EEDF come from our experimental OES measurements of EEDFs with enhanced tails, which is described in Chapter 6. The result demonstrates that for the EEDF with enhanced tail, the contribution from electrons in the 'tail' distribution to Ar $3p^5 4p$ and $3p^5 5p$ emissions can be safely neglected (Fig. 2.15). The domination of these emission lines by 'bulk' electron excitations means that they carry limited information about the high energy 'tail'.

Once the analysis to determine the bulk distribution parameter has been completed, we begin the second step, i.e., to determine the tail distribution. In order to determine the free parameters in the log-normal distribution, emission lines with higher threshold energies are required. The emitting states of Ar^+ are excited by electrons with energies beyond 35 eV (Fig. 2.6), making it a possible choice. As illustrated in Fig. 2.15, the 460.96 nm Ar^+ emission is dominated by the 'tail' electron

contribution and the bulk contribution is negligible. The OES diagnostic of EEDF tails using Ar and Ar^+ emissions will be discussed in detail in Chapter 5. In addition, emissions from other rare gases (i.e., Ne, He) that include neutral states with threshold energies higher than those for argon (Fig. 2.6), are also sensitive to the tail distribution and can contribute to the determination of the tail distribution. The use of Ar, Ar^+, Ne and He emissions to measure enhanced EEDF tails will be introduced in Chapter 6.

2.3.2 Determination of Ar ($3p^5 4s$) and Ne ($2p^5 3s$) number densities

Ar($3p^5 4s$) and Ne ($2p^5 3s$) (metastable and resonance level) number densities can be found by comparing measured relative intensities with the predictions of the emission model including the effects of radiation trapping, in what is called the OES branching fraction method (OES-BF) [75].

A full and accurate accounting of radiation trapping in plasma emissions is complicated owing to the complex nature of spectral emission line shapes and spatial variations in the densities and temperatures of emitting and absorbing atoms [87, 54, 88, 89]. To simplify the analysis, a 'universal' escape factor g [89, 90, 91] is used, which refers to the probability for an emitted photon to successfully escape the plasma. The escape factor $g(k_{ij}(n_j)\rho)$, is derived using volumetric averages assuming a spatially uniform distribution of emitting and absorbing atoms by Mewe [92], where $k_{ij}(n_j)$ is the reabsorption coefficient [75] and ρ is the scale length of the plasma. Although this assumption can be questioned for a typical plasma, the departures for both absorbing and emitting components in escape factor partially offset each other such that this simplification can be used to accurately model radiation trapping. This approach was also employed by Schultz *et al.* to model emissions from Ar plasmas [93]. Using this escape factor, the branching fraction Γ_{ij} which characterizes the $i \rightarrow j$ spontaneous emission, is replaced by the effective branching fraction Γ_{ij}^{eff} which accounts for radiation trapping. The correction factor R_{ij} in Eq. 2.2 is equal to $\Gamma_{ij}^{\text{eff}}/\Gamma_{ij}$.

By considering line ratios from the *same* upper state, the dependence on the populating mechanism is removed so that the relative emission intensity only depends on the effective branching fractions,

$$LR_j^{\text{model}} = \frac{I_{ia}}{I_{ib}} = \frac{\Gamma_{ia}^{\text{eff}}}{\Gamma_{ib}^{\text{eff}}} = \frac{\Gamma_{ia}\; g(k_{ia}(n_a)\rho)}{\Gamma_{ib}\; g(k_{ib}(n_b)\rho)} \tag{2.8}$$

where I_{ia} and I_{ib} are the photon emission rates for transitions terminating on lower levels a and b. Similar to the numerical χ^2 analysis in the determination of EEDFs, the Ar($3p^5 4s$) and Ne ($2p^5 3s$) number densities are obtained by minimizing the difference between model predicted line ratios to the experimentally observed values. In principle, a total of four 1s level number densities must be determined from the OES-BF analysis, requiring at least four line ratio measurements. However, the number densities of the two resonance levels under a wide variety of plasma conditions are generally about the same as each other, while the number densities of the two metastable levels are typically proportional to one another. Therefore, only two line ratios, one for the metastable levels and one for the resonance levels, are necessarily required. In practice, all available line ratios (i.e., from 8 to 10 lines for Ar) are employed in the OES-BF method to average out random uncertainties. Note that the OES-BF analysis is not applicable to He metastable densities. For the case He metastable densities are required, they can be determined from white light absorption measurements (OAS), the general principle of which is described in Section 3.2.2.

2.3.3 Determination of electron density

The electron density (n_e) is determined by quantifying the suppression of emission intensities caused by electron impact de-excitation. Without electron quenching, the $i \rightarrow j$ emission line is characterized by the branching fraction Γ_{ij} which is found by dividing the $i \rightarrow j$ photon emission rate A_{ij} by the total photon emission rate $\sum_l A_{il}$. However, the electron-impact de-excitation adds a non-radiative decay channel to atoms in the excited level-i, therefore yields a 'new' branching fraction. The electron quenching factor is defined as the ratio of the 'new' branching fraction to the 'old' one,

$$\gamma_{ij}^{\mathrm{de-exc}} = \frac{\text{new } \Gamma_{ij}}{\text{old } \Gamma_{ij}} = \left(\frac{\Phi_{ij}}{\sum_l \Phi_{ij} + K_i \, n_e} \right) \Big/ \left(\frac{\Phi_{ij}}{\sum_l \Phi_{ij}} \right) = \frac{1}{1 + n_e / n_{eC,i}} \tag{2.9}$$

where k_i is the electron impact de-excitation rate out of level i into all other levels. To express the dependence of electron quenching on n_e explicitly, the critical electron density, $n_{eC,i}$, for level-i is defined as the ratio between the spontaneous emission and electron quenching rates, which equals to $\sum_l \Phi_{ij}/k_i$. Zhu and Pu have obtained $n_{eC,i}$ values for a number of Ar levels by measuring the variations of plasma emissions with electron density [94, 95]. With known $n_{eC,i}$, the electron

quenching factor, γ_{ij}^{de-ex} is solely a function of n_e.

The line ratio formed by emissions out of two upper states where the primary populating mechanism are both excitation from the ground state, but the radiative lifetimes are radically different, is selected to determine the electron density. This ratio is independent of ground state density. When two upper states with close threshold energies are chosen, the excitation rate ratio is nearly independent of T_e or the EEDF. Therefore, this line ratio provides a one-to-one mapping to the electron density,

$$\frac{\Phi(\lambda_1)}{\Phi(\lambda_2)} \simeq \frac{k_1\gamma_1}{k_2\gamma_2} = \frac{k_1}{k_2}\left(1+\frac{n_e}{n_{eC1}}\right)^{-1}. \tag{2.10}$$

where k_1 and k_2 are the known excitation rates for long-lived level-1 and short-lived level-2. γ_1 is the electron quenching factor for the long-lived level and electron quenching for the short-lived level is ignored ($\gamma_2 = 1$). In practice, the short-lived level is typically taken to be one of the lower J=0 levels ($2p_1$, $2p_5$, $3p_1$, or $3p_5$), and the long-lived level is taken from the higher members of this series ($4p_1$, $4p_5$, $5p_1$, $5p_5 \ldots$).

Chapter 3

Plasma source and diagnostics

A low electron temperature, low-pressure inductively coupled plasma ICP source was used for the studies presented in this document. Multiple optical and electrical diagnostics, including OES, white light absorption spectroscopy (OAS) and Langmuir probe are included on this system. This chapter will discuss the relevant apparatus used for the experiments and the basic mechanisms of the diagnostics employed.

3.1 Plasma source

This section describes the vacuum system used for the OES study, the generation of inductively coupled plasmas and the installation of a hot electron source (Fig. 3.1):

- **Vacuum system:** Inductively coupled plasmas are generated in a 50 cm diameter vacuum chamber with aluminum walls, which has comparable size to reactors used in semiconductor fabrication applications. There are four diagnostic ports located at the same axial position on the chamber. Source gases include Ar, Ne, He, N_2, O_2, H_2 and mixtures of these gases. The plasma is typically operated at 1-30 mTorr, which is comparable to the range used in integrated circuit (IC) fabrication plasma process tools [1, 9].

- **ICP generation:** An inductive discharge is generated using a flat spiral antenna, separated by a quartz or ceramic dielectric window from the plasma. RF currents in the antenna generate oscillating magnetic and electric fields which penetrate the plasma region through

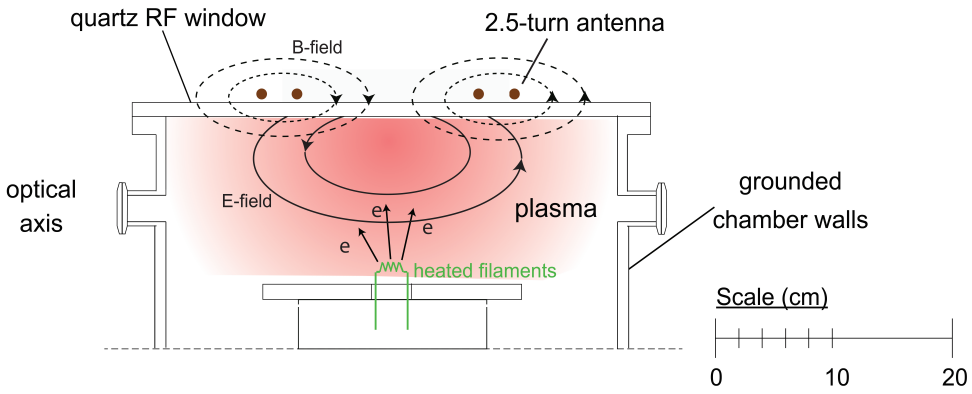

Figure 3.1: Side view of chamber. Radius of antenna is $\sim$ 15 cm, wall radius is 25 cm. Schematic of induction fields for the flat antenna is shown. Heated filament electron source is installed at the bottom of the plasma volume to inject energetic electrons.

the dielectric window. The RF electric fields accelerate the free electrons which in turn sustain the discharge through ionizing collisions with neutral gas atoms or molecules [13, 1]. In this study, RF power (0-3000 W) at 13.56 MHz is fed through a pi-matching network to the 2.5 turn planar flat coil antenna located on top of a quartz window.

- **Energetic electron source:** An auxiliary source of energetic electrons is added to the ICP. A set of thoriated tungsten filaments are located near the lower electrode and heated to thermionic emission. More detailed information about the electron source and its use can be found in Chapter 4.

3.2 Diagnostic methods

Multiple diagnostics, including OES, OAS and a Langmuir probe are installed on the ICP system to measure plasma parameters, including the number densities of metastable and resonance levels, the EEDF and the electron density (Fig. 3.2). The operating principles and the apparatus of the diagnostics are discussed in this section.

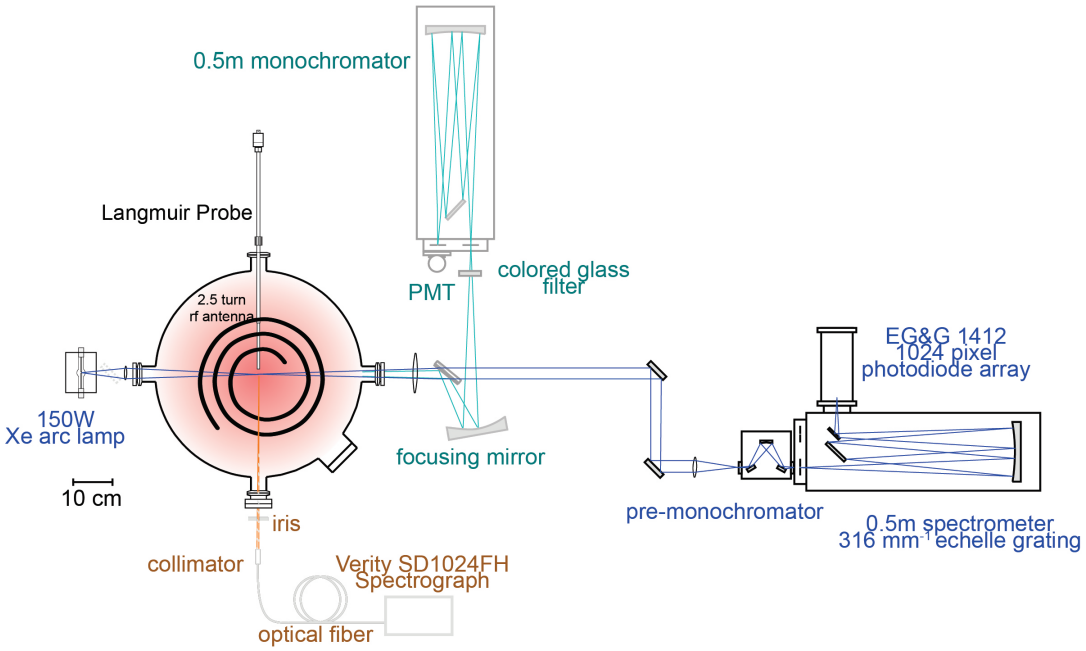

Figure 3.2: Top down view of ICP system showing diagnostics: photomultiplier tube (PMT) in conjunction with a 0.5 m monochromator for high-resolution OES; compact, fiber coupled Verity spectrometer for low-resolution OES; white light source and 0.5 m spectrometer used for OAS; and Langmuir probe.

3.2.1 Optical emission spectroscopy

Optical emission spectroscopy is used to determine the metastable and resonance densities, the EEDF and the electron density. OES has been implemented using two separate spectrometer systems with different features based on the method discussed in Chapter 2. The spectrometer parameters are listed in Table 3.1. For a spectrometer system, there is a relative efficiency of detection, of light signal, as a function of the wavelength, which is called spectral sensitivity. The spectral sensitivities of the two spectrometer systems here are calibrated by measuring the signal from a Vϕ standard lamp.

Using the high resolution PMT in conjunction with a 0.5 m monochromator, static OES measurements for continuous wave (cw) plasmas and phase-resolved measurements for pulsed plasmas can be conducted. For cw plasmas, scanning through a selected wavelength range to record high resolution spectra takes in a relatively long period ($\sim$30 mins). In addition, the PMT can be used

Table 3.1: The spectrometer systems used for optical diagnostics. "spe. acquisition time" refers to the time needed to record the spectra. The grating of the Verity spectrometer is not listed in the manual.

system	scanning monochromator	Verity SD1024FH	0.5 m spectrometer
function	OES static time-resolved	OES real-time time-resolved	OAS static
detector	PMT	1024 CCD array	cooled 1024 photodiode
wavelength range	300-830 nm	300-800 nm	400-750 nm
resolution	0.1 nm	1.4 nm	0.01 nm
spe. acquisition time	$\sim$ 30 min	$\sim$ 100 ms	$\sim$ 20 min
grating	1180 mm^{-1}	unknown	Echelle 316 mm^{-1}

to record emission signals as a function of time for each wavelength of interest. A trigger source can be used to synchronize the PMT output to the pulse modulation of plasmas, so that time-resolved emission signal can be recorded.

In addition to using the high resolution PMT-based spectrometer, plasma emissions sent through an optical fiber can be recorded by the Verity SD1024FH spectrometer, which is a small form-factor spectrometer with low resolution. Utilizing the 'fast' (millisecond scale) spectra acquisition feature of this spectrometer, real-time monitoring of plasma parameters from emission spectra has been achieved (Section 8.1), although the low resolution complicates the OES analysis. In addition, OES measurements of non-Maxwellian EEDFs can be conducted using this low-resolution spectrometer (Section 8.2 and 8.3).

3.2.2 White light absorption spectroscopy measurements

White light absorption spectroscopy (OAS) is used to determine the metastable and resonance densities and has been used as a benchmark for OES results. A xenon arc lamp is used as an external source of continuum light, which is directed through the plasma and partially absorbed by Ar ($3p^5 4s$) species. The size of absorption dips in the recorded transmitted spectrum is proportional to the number density of absorbing levels. Redundant measurements at different wavelengths are conducted to obtain the metastable and resonance densities from more than one line. The density

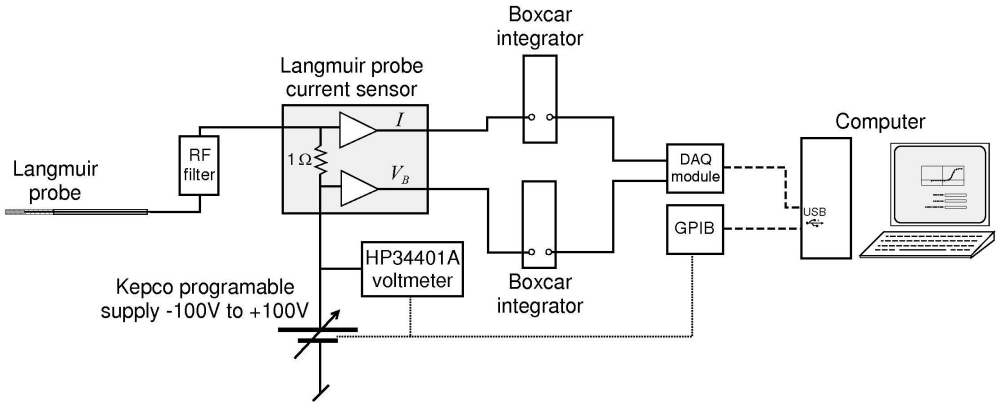

Figure 3.3: Langmuir probe electronics. The bias voltage (V_B) is supplied by a computer-controlled programable power supply. A tuned passive RF filter has a high impedance at the drive frequency of the inductively coupled plasma (13.56 MHz), so that the probe tip follows plasma potential variations in the plasma and V_B with respect to the plasma is constant (on the timescale of the rf frequency) [97]. The applied voltage and resulting probe current are sampled by separate boxcar integrators and imported into the computer through data acquisition cards.

values from different lines are averaged to yield the 'final' results. A detailed description of the OAS method can be found in Ref. [75].

In this experiment, white light from a Xe arc lamp is passed through the plasma and sent through a 10 cm pre-monochromator used for order-sorting and to decrease the scattered light, and then collected by the 0.5 m spectrometer system introduced in Table 3.1.

3.2.3 Langmuir probe measurements

The Langmuir probe consists of a small conducting (tantalum) tip exposed to the plasma, and connected electrically through a vacuum feedthrough to control and data acquisition circuitry [13]. The probe current-voltage ($I - V$) curve is recorded, and the EEDF is obtained from the second derivative of the probe current with respect to the bias voltage [96]. The electron density is obtained by integrating over the derived EEDF.

Langmuir probes system. As shown in Fig. 3.3, the Langmuir probe system is composed of three main elements, (i) the probe itself, (ii) an rf-filter designed by Wendt [97] to force the probe tip voltage to follow RF plasma potential fluctuations, and (iii) the relevant electronics. The probe current and bias voltage are sampled and averaged by the boxcar integrators. Besides

the measurements of cw plasmas, time-resolved probe measurements for pulsed plasmas can be conducted by synchronizing the boxcar integrator "window" to the pulse modulation. The temporal dependence of the EEDF and electron density is therefore obtained from the time-resolved I-V curves.

3.2.4 Harmonic probe method

The conventional probe method described in the previous section works well for determining EEDFs in the low electron energy range (i.e, below ∼20 eV), but the accuracy diminishes at higher energies due to the decreasing signal-to-noise ratio and the amplification of noise when differentiating the original IV characteristic, especially when the plasma density is low. However, the high energy range of the EEDF is critical to the plasma reaction rates including excitation, ionization and dissociation. Thus, an alternate EEDF measurement which utilizes harmonically driven electrostatic probes and works better in regions of higher energy, is also employed [98, 99, 100, 101, 102].

In this harmonic method, a small AC voltage ϕ(t) is superimposed on the DC probe bias V_0. Due to the nonlinearity of the probe IV characteristic, the probe current is modified. A Taylor expansion of the probe current $I(V)$ reveals that the second harmonic term of the measured probe current is proportional to the second derivative of current with respect to voltage.

$$I(V) = I(V_0 + \phi(t)) = I(V_0) + \phi(t)\frac{dI(V_0)}{dV} + 1/2(\phi(t))^2\frac{d^2I(V_0)}{dV^2} + ... \tag{3.1}$$

Since the second derivative of the probe $I - V$ curve is proportional to the EEPF [13], the second harmonic term of the probe current is also proportional to the EEPF. The electron density can be found be integrating the EEPF (g(E)) over all energies [13],

$$n_e = \int_0^\infty g(E)\sqrt{E}\, dE\ . \tag{3.2}$$

Therefore, the integration of the second harmonic term of the probe current (g_h(E)) is proportional to the electron density,

$$n_e = A\int_0^\infty g_h(E)\sqrt{E}\, dE\ . \tag{3.3}$$

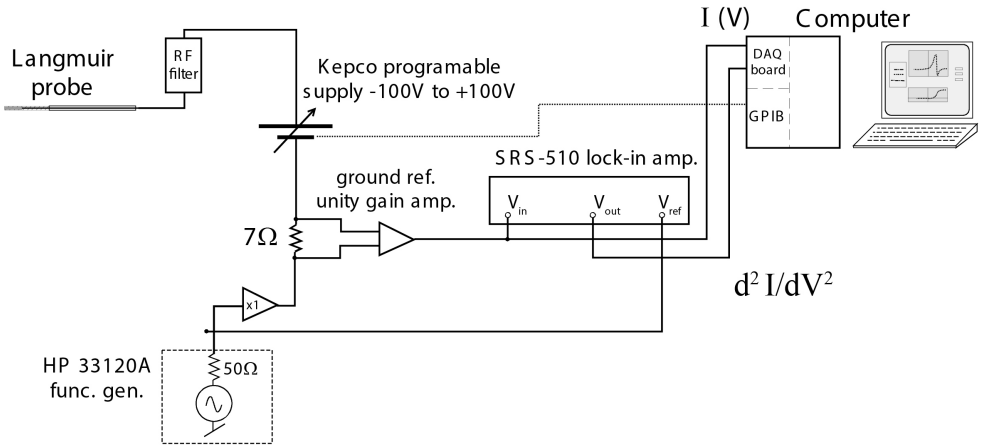

Figure 3.4: Langmuir probe electronics for harmonic method. The lock-in amplifier is used to measure the second harmonic signal of the probe current. There are two additional op-amp circuits in the harmonic probe system. One converts the floating voltage drop across the 7 Ω resistor to a ground-referenced signal. The other one is a unite gain amplifier used to isolate the 50 Ω output impedence of the function generator.

When electron density n_e is obtained from the conventional probe technique, the proportionality constant A between the EEPF and the second harmonic term of the probe current can be determined. Once this proportionality constant is determined, it can be applied to probe measurements at different plasma conditions.

With the conventional technique, the dynamic range of the amplifier must be set to prevent overloading the electronics for large probe currents near the electron saturation region. This makes measurements difficult in the high energy range of the EEDF which correspond to regions of the $I - V$ curve with a relatively small probe current. In contrast, with this harmonic technique the gain of input signal amplifier can be adjusted more easily to match the size of the observed signal, allowing a higher gain in regions of smaller signal. In principle, this should allow 'good' EEDF measurements in regions of higher energy.

Harmonic probe system. As shown in Fig. 3.4, the small AC signal is created by a HP33120A function generator. The Kepco BOP-100 programable power supply floats on this signal, producing a probe bias with both a high voltage DC component and low voltage AC component. The probe current is measured by recording the voltage drop across a 7 Ω resistor placed between the two voltage sources. An SRS 510 'analog' lock-in amplifier in is used to extract the second harmonic of

the resistor voltage.

Chapter 4

Generation of non-Maxwellian EEDFs

The topic of this thesis is OES diagnostics for measuring the electron energy distribution functions (EEDFs), because of the central role they play for many industrial plasmas, such as those used in the fabrication of integrated circuits (ICs) [19]. In order to evaluate OES diagnostics under plasma conditions similar to those for which they may be applied, a wide range of EEDF shapes is sought for this study. Plasmas employed in industrial applications are typically *non*-equilibrium in the energy distributions of their charged constituents [32, 33, 34]. Therefore, the generation of non-Maxwellian EEDFs with energy dependence which can be varied systematically will aid in the development and characterization of OES diagnostics.

The OES diagnostics described in this thesis have, up until now, been evaluated in argon inductively coupled plasmas (ICPs) over a range of pressure (1-50 mTorr) comparable to the range used in IC fabrication plasma process tools [59, 74]. Here, it is desired to produce non-Maxwellian EEDFs with shapes and average energies beyond the range explored in previous studies, as a means to evaluate OES diagnostic performance for an extended range of conditions.

Among schemes to produce EEDFs of varying shape [39, 103, 104, 45, 105, 106, 38, 44, 43, 107, 108], one option is the modification of a conventional plasma source through the addition of an auxiliary source of energetic electrons [39, 103, 104, 45, 105, 106]. In this thesis, the auxiliary electron source takes the form of high-energy electrons injected into an ICP plasma from a set of heated filaments. Modified EEDFs obtained in this way have been characterized and used to evaluate the OES diagnostics, as will be described at length in subsequent chapters.

This chapter provides a summary of the work undertaken in this thesis to produce plasmas in

which the shape of the EEDF could be varied systematically and over a range that extends beyond what has been used in previous OES studies. This chapter begins, therefore, with an overview of prior work examining OES as a diagnostic for non-Maxwellian EEDFs. This review will focus on the range of EEDF shapes that were successfully detected using OES in these studies, and will thereby serve as a point of reference for the study described in this thesis. Following the literature review is a description of the modified ICP source developed for this study, which makes use of an auxiliary energetic electron source. This modified ICP source was first characterized using Langmuir probe measurements of EEDFs, originally planned to provide guidance in selecting source operating conditions for the OES study. In addition to the Langmuir probe results, also presented are preliminary OES results that hint at the presence of a "hot tail" electron population, in an energy range beyond the detection limit of our Langmuir probe system.

4.1 Overview of OES diagnostics for non-Maxwellian EEDFs

In this section, previous studies about measuring non-Maxwellian EEDFs using OES diagnostics are summarized, with a focus on the range of EEDF shapes that were successfully detected. Among these OES measurements, the one conducted by Boffard *et al.* in argon inductively coupled plasmas (ICP) over a range of source pressure is discussed at length. In this thesis, the ICP source in the Boffard studies has been modified to produce EEDFs with shapes and average energies beyond the range previously explored by varying the source pressure.

While Boffard's work examines OES of argon, trace rare gases optical emission spectroscopy (TRG-OES), which makes use of a mix of rare gas emissions, has also been used to measure non-Maxwellian EEDFs. For example, Malyshev *et al.* [78, 109] observed EEDFs with depleted high-energy tails in a transformer coupled plasma (TCP) at pressures above 5 mTorr. EEDFs with depleted tails were also measured by Behringer *et al.* in a DC glow discharge. The three-parameter "x-form" representation of non-Maxwellian EEDFs (described in Sec. 2.3.1) was used, yielding values of x and T_x. The electron temperature (T_x) decreases from 5.5 to 3 eV as the discharge pressure increasing from 1.4 to 7 Torr, and x, the parameter characterizing depletion of the high energy portion of the EEDF was found to vary between 1.6 and 2.2. In addition, EEDFs with enhanced tails have also been measured by the TRG-OES method. In low power ($<\sim$100 W)

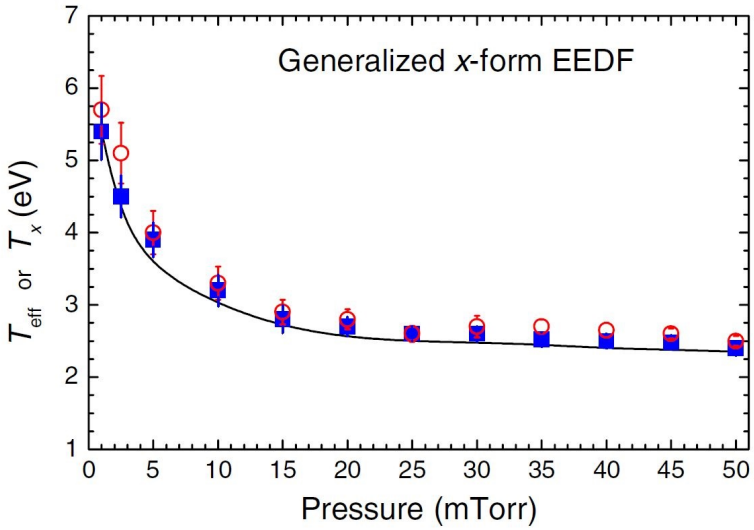

Figure 4.1: Generalized x-form for pure Ar ICPs as a function of pressure. The line is the value obtained from a global model analysis [13], solid points are from a fit to probe values, and open points are from OES analysis. For the OES and global model analysis, x was fixed at $x = 1.2$ for pressures < 25 mTorr, and varied linearly with pressure to a value of $x = 1.6$ at 50 mTorr [74].

Chlorine ICPs [110] and Oxygen TCPs [109], the OES-derived T_e were higher than the Langmuir probe results supporting the presence of enhanced high-energy EEDF tails. Fuller *et al.* [111] measured electron temperatures representative of the high energy tail (>9.8 eV) of the EEDF in Cl_2-Ar ICPs by the TRG-OES. Also, he measured the electron temperature, T_e, in a high-density inductively (transformer) coupled (TCP) 10 mTorr oxygen plasma as a function of power [112]. The EEDF is measured to be bi-Maxwellian distribution (i.e., with "enhanced tail," as described in Sec. 2.3.1) from ∼120 to 1046 W. An Ne (585.2 nm)-to-Ar (750.4 nm) emission ratio is also used as a qualitative indicator of the relative population of high-energy electrons in the measurements of O_2 TCPs [112]. Furthermore, Chen *et al.* [113] measured EEDFs using TRG-OES for a 500 W CF_4/O_2 capacitively coupled plasma (CCP) as a function of pressure (4-200 mTorr). The observed EEDFs varied from a Maxwellian distribution to a bi-Maxwellian distribution. The measured 'bulk' electron temperature varied from ∼8 to ∼3 eV and the 'tail' electron temperature changes from ∼6 to ∼7 eV. When the 'bulk' electron temperature was lower than the 'tail' electron temperature, an enhanced EEDF tail was measured. Moreover, Zhu and Pu [114] measured bi-Maxwellian EEDFs using argon and krypton emissions in Ar-containing ICPs at 10 mTorr, 12 W and 200 W.

The OES method developed by Boffard *et al.*, which is the basis of the OES diagnostics developed in this thesis, has been used to study argon inductively coupled plasmas (ICPs) [59, 74].

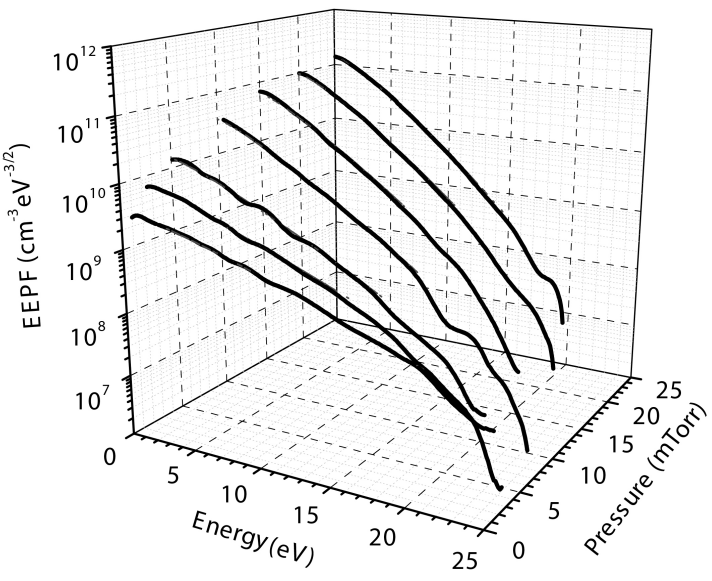

Figure 4.2: EEPF versus Ar pressure in 600 W ICP, obtained from Langmuir probe measurements [74].

In Boffard's study, the three-parameter "x-form" representation of non-Maxwellian EEDFs was used in the OES analysis, yielding values of x and T_x [82, 83]. The variation of the EEDF as a function of pressure was measured for a 600 W argon ICP between 1.0 and 50 mT. The OES diagnostic captured a decrease in electron temperature (T_x) from 5.3 to 2.3 eV with increasing pressure. Excellent agreement in T_x between probe and OES values at all pressures was observed (Fig. 4.1). The deviation in the shape of the EEDF from the Maxwell-Boltzmann form can also vary with pressure. Semi-log plots of sample probe-derived EEPF traces in the 1-25 mTorr are shown in Fig. 4.2. (A semi-log plot of the EEPF has a linear dependence on electron energy in the case of a Maxwellian distribution.) At low energies (< 10 eV) all of the curves in Fig. 4.2 appear approximately linear, but at higher energies the curves exhibit 'depleted tails'. Using the shape parameter 'x' in the x-form representation of EEDFs as an indication of deviation of the EEDF from a Maxwellian form, in the 1-50 mTorr range, the variation of values of 'x' from 1.1 to 1.6 was also successfully captured by the OES measurements (Fig. 4.3).

In prior works, OES measurements of non-Maxwellian EEDFs were conducted in conventional plasma sources, i.e., DC discharges, ICPs, TCPs and CCPs. Although the EEDFs can be modified by changing the discharge power and source pressure, people only have limited control of the shape

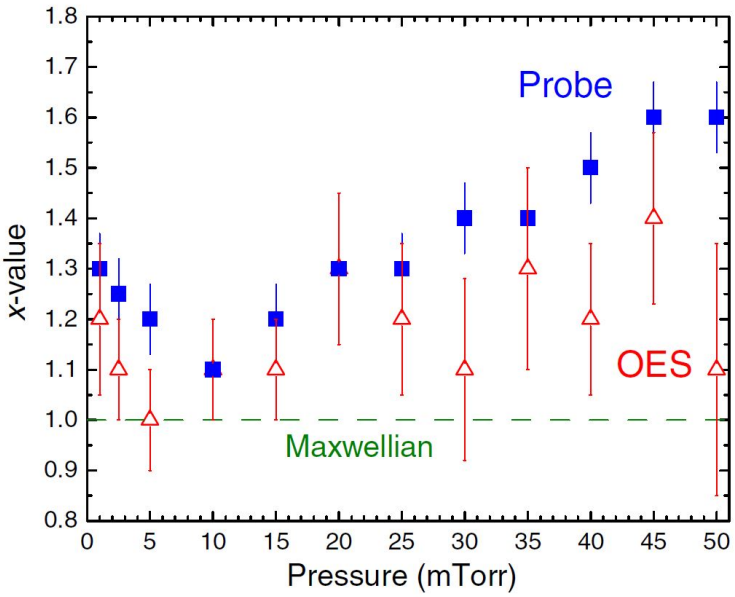

Figure 4.3: Variation of EEDF shape parameter x with pressure for a 600 W Ar ICP. Squares are probe results, and triangles are OES results [74].

of the EEDF. First, the 'bulk' EEDF and the EEDF tail cannot be controlled independently in previous studies. For example, for depleted tail EEDFs, the electron temperature (T_x) and the depletion of the EEDF tail (x) both varied with the source pressure. Second, the enhanced high-energy tail is insensitive to the changes in 'bulk' discharge conditions. For example, in Ref. [113], varying the pressure of a CCP discharge from 4-200 mTorr only changes the 'tail' electron temperature from ~6 to ~7 eV. Also, the density and the shape of the EEDF tails may not be controlled independently and systematically by changing the 'bulk' discharge conditions. The intent of the work presented in this chapter is therefore to modify a conventional plasma source (i.e., ICP) to produce EEDFs with shapes and average energies can be controlled systematically and beyond the range previously explored.

4.2 Heated filaments as electron source

In this thesis, an auxiliary electron source in which the emitted electron energy and current can be systematically varied is added to the existing ICP system as a means to manipulate EEDFs. The auxiliary electron source consists of a set of filaments that can be heated to produce thermionic emission. This section introduces the design of the electron source and the capable ranges of emitted

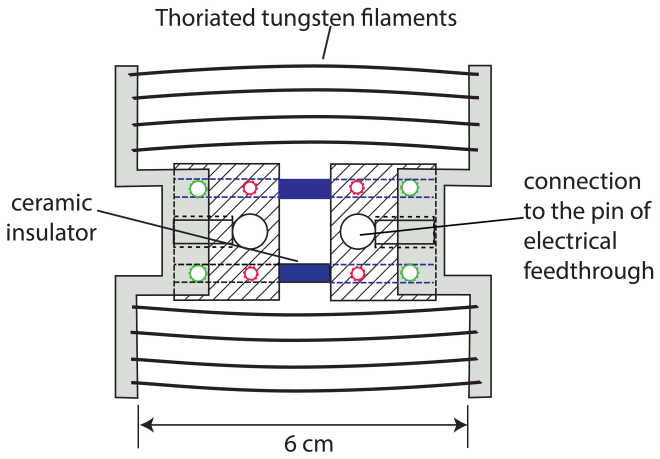

Figure 4.4: Auxiliary electron source: filaments and support assembly. Thoriated tungsten filaments will be ohmically heated with an external current source to emit electrons.

electron current and energy.

4.2.1 Design of electron source

The electron source is composed of eight 1% thoriated tungsten wires, 125 μm in diameter and 6 cm in length (Fig. 4.4). Similar to an incandescent light bulb, current through the filaments from an external power source produces resistive heating, in this case resulting in the thermionic emission of electrons. The energy of the electrons emitted is determined by a bias voltage applied to the filaments. The current of emitted electrons is determined by the heater current through each filament, and the length and number of filaments. Since the total current output of the heater supply is limited (25 A), there is a trade off between the current on each filament and the number of filaments. Also, the lifetime of the filaments decreases with increasing current through each filament. With fixed heater current, using longer filaments is another method to increase the emitted electron current. However, voltage variation along the filaments in the presence of the heater current due to the filament resistance produces a spread in the energies of the injected electrons which increases with the length of the filaments. Accounting for all these factors, the design of the electron source (length and number of filaments) has been optimized to maximize the emitted electron current.

The auxiliary electron source is installed at the bottom of the ICP system in place of the bottom

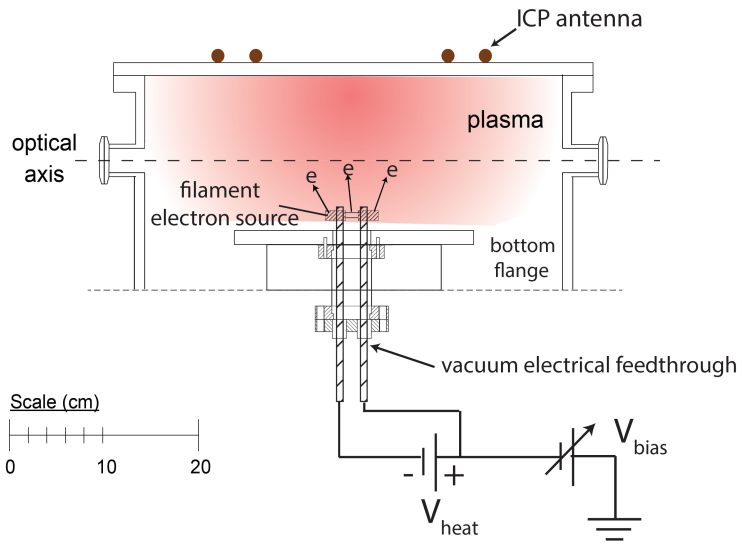

Figure 4.5: Schematic diagram of the energetic electron source installed on the ICP system. The electric circuit, including the heater voltage (V_{heat}) and the bias voltage (V_{bias}), is also shown.

electrode, at the edge of the plasma and as far from the line of sight of the optical measurements as possible (Fig. 4.5). The distance from the filaments to the optical axis is ∼6 cm, and the distance from the filaments to the top of the chamber is ∼14 cm. To control the injected electron flux and energy independently, the filaments are heated by a 40 V, 25 A DC power supply and biased by a 1 A, -50 to +50 V DC power supply (Fig. 4.5). The electrical connections to the filaments are made via a vacuum electrical feedthrough (rated to 185 A, 12 kV) and stainless steel electrodes to which the ends of the filaments are spot-welded (Fig. 4.4). The electrodes attach to rods that make an electrical connection through a vacuum feedthrough and have "wings" that set the electrode spacing to the design value of the filament length. The lifetime of the filaments is typically ∼10 hours of operation. The design allows for removal of the electrode assembly as a rigid unit to facilitate filament replacement.

4.2.2 Characterization of electron source

The emitted electron density and energy ranges of the electron source have been studied. The emission current of the filaments was found to range from 0 to ∼1.2 A with increasing heater current (Fig. 4.6). In addition, the energy of the emitted electrons is set by the voltage applied

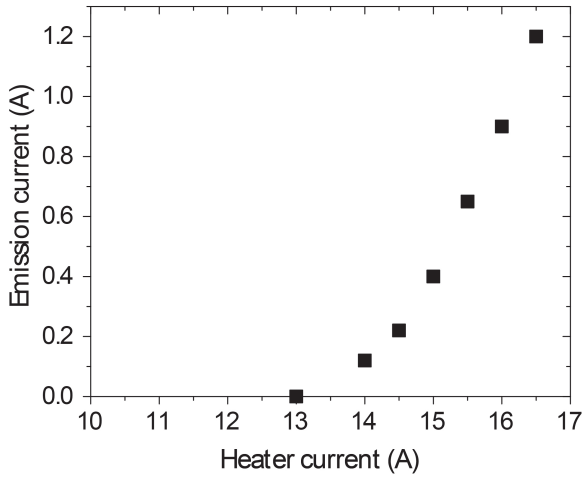

Figure 4.6: Electron injection current vs heater current

to the filaments, which is the sum of the heater voltage and the bias voltage (0-60 V). For the maximum expected heater current of 1.2 A, the corresponding voltage drop between the filament ends is 10 V.

4.3 Effect of electron injection on ICP EEDFs

Previous experiments and simulations have illustrated that EEDFs are altered by injecting energetic electrons into the plasma [106, 30, 115, 104, 45]. The modified EEDFs were shown to depend on both the 'bulk' discharge conditions and properties of the added electrons. For example, Z. C. Lu *et al.* [30] reported measurements of EEDFs with truncated high-energy tails when energetic electrons were injected (Fig. 4.7). The depletion of the EEDF tail changed with the injected electron current and with the discharge pressure.

In this section, the effect of emitted electrons on Ar ICP EEDFs are investigated using the harmonic probe method (Sec. 3.2.4) as a function of multiple control parameters, including the electron injection current, filament bias voltage, source pressure and discharge power. The characterization of the modified ICP source here provide guidance in systematically controlling the EEDFs and selecting source operating conditions for evaluating OES diagnostics in subsequent chapters.

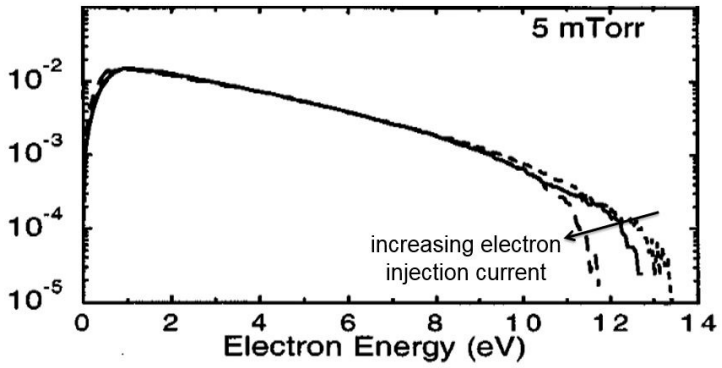

Figure 4.7: EEDFs with truncated high-energy tails when energetic electrons were injected. The depletion of the EEDF tail increases with the injected electron current [30].

4.3.1 Electron injection current

At a fixed plasma condition (15 mTorr, 100 W, Ar ICP) and filament bias (-50 V), probe measurements were made as a function of electron injection current (from 0 to 1 A). The voltage corresponding to the location of the knee in the $I - V$ trace is the plasma potential (V_p). As shown in Fig. 4.8a, the plasma potential decreases as the electron injection current is increased. The reduction in plasma potential with increasing electron injection may be attributed to the extra negative charge introduced by the dc electron current [106, 30].

The EEDFs in ICPs with different filament emission currents are obtained from Langmuir probe measurements described in Sec. 3.2.4 (Fig. 4.8b). The T_x and x values are determined by fitting the probe-derived EEDFs to the 'x-form' (Eq. 2.4) representation. Specifically, trial EEDFs are produced using the 'x-form' with assumed T_x and x values. The values of T_x and x are determined as those which minimize the difference between the assumed and measured EEDFs. Figure 4.9 plots EEPF (EEDF/$\sqrt{E}$) result for the Ar ICP with 1A electron injection current obtained from the probe and its fit to the 'x-form'. The 'x-form' is found to be a good representation of the EEDF here.

The electron temperature (T_x) plotted in Fig. 4.10b) was observed to drop from 3.2 to 2.3 eV as the electron injection current increases from 0 A (ICP only) to 1 A. Suppression of the electron temperature when electrons are injected into the discharge has also been reported by other groups [45, 116, 106]. The shape parameter x remains fairly constant at the value of $\sim$1 as the electron

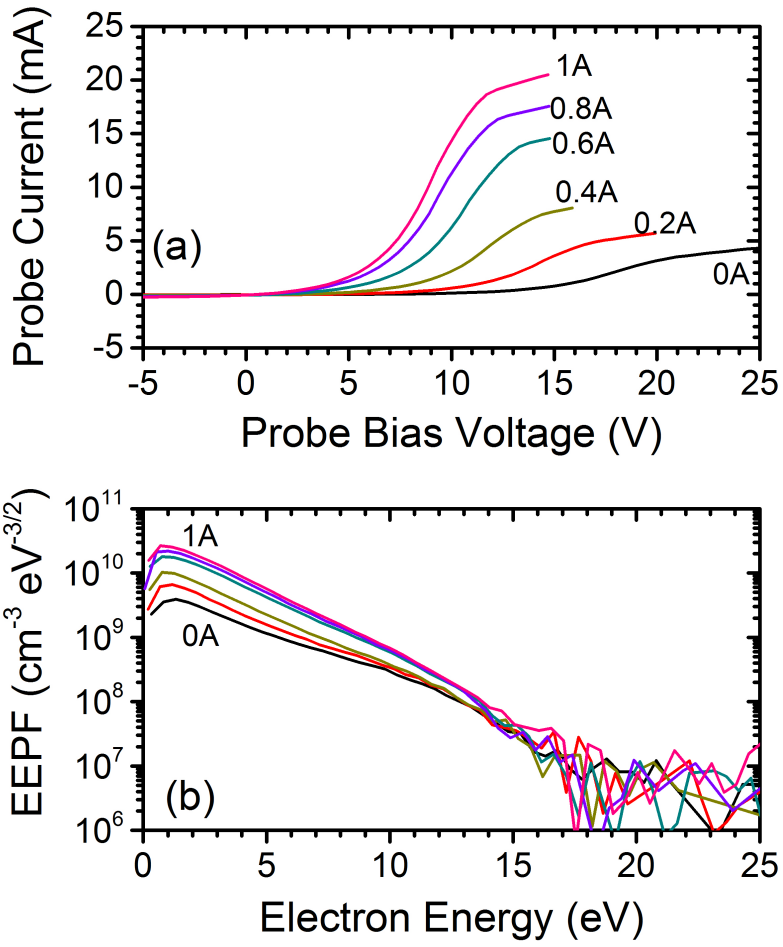

Figure 4.8: Langmuir probe $I-V$ traces and derived EEPFs ((EEDF/$\sqrt{E}$)) for an Ar ICP (100 W, 15 mTorr) with electron injection (-50 V bias) as a function of electron injection current.

injection current increasing (Fig. 4.10c). Due to the low T_x and n_e, the EEDFs measured by our probe system become noisy above ~15 eV, indicating a high degree of uncertainty for high electron energies (Fig. 4.8b). Thus, the effect of electron injection on the 'bulk' EEDF shape is modest, and information about the tail of the distribution cannot be determined by Langmuir probe.

Another effect of electron injection is the large increment in electron density (n_e) (Fig. 4.10d). This effect was also observed by Haas *et al.* [45, 116] when they injected 'hot' electrons into the 'bulk' discharge. The modification of n_e is proportional to the power absorbed by the discharge from the injected electrons. For a -50 V filament bias voltage, the injected electrons have energies

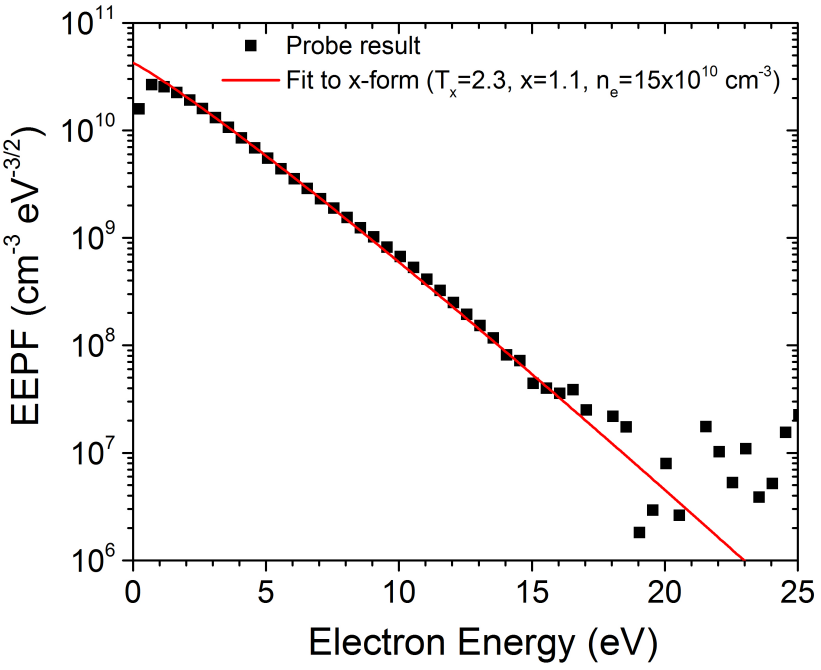

Figure 4.9: Electron energy probability function (EEDF/$\sqrt{E}$) for an Ar ICP (100 W, 15 mTorr) with electron injection (1A, -50 V filament bias). Squares are probe data. Solid line is a fit to generalized x-form EEDF.

above the ionization threshold energy of Ar (15.76 eV) and therefore contribute to the ionization of Ar neutral atoms, and a higher n_e. Here, n_e increases from 3.5 to 18.2×10^{10}cm^{-3} as the electron injection current increases from 0 to 1 A.

4.3.2 Filament bias voltage

As a second control parameter, the bias voltage on the filaments was varied to control the injected electron energy for fixed plasma operating parameters (15 mTorr, 100 W, Ar ICP) and electron injection current (1 A). The average potential difference between the filaments and the center of the discharge is used to estimate the average energy of injected electrons:

$$E_{\text{inj}} = e(V_p - V_{\text{bias}} - 1/2\ V_{\text{filament}})\ , \tag{4.1}$$

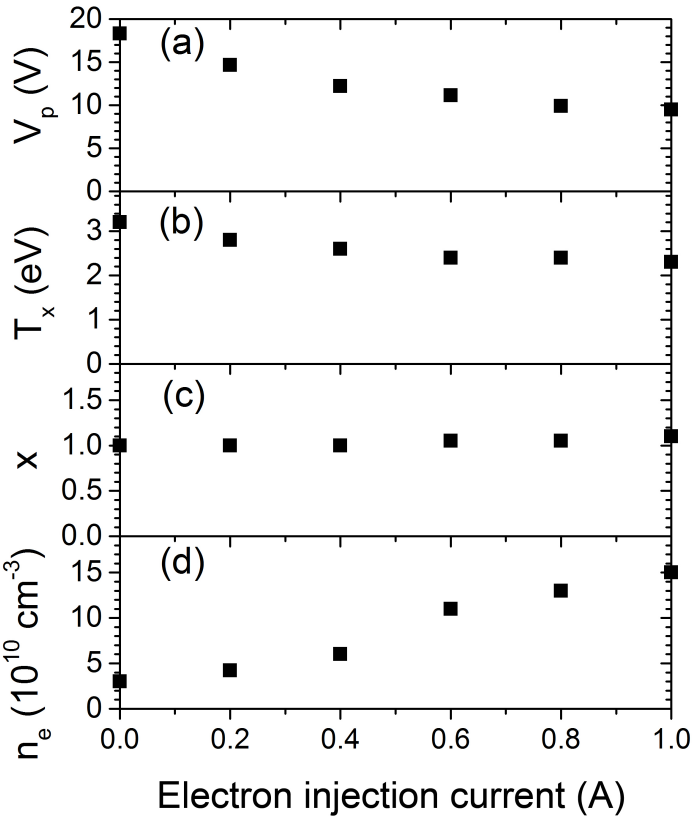

Figure 4.10: EEDF parameters for an Ar ICP (100 W, 15 mTorr) with electron injection (-50 V bias) as a function of electron injection current, including: (a) plasma potential, V_p, (b) electron temperature, T_x, (c) shape parameter, x and (d) electron density, n_e.

where V_p is the plasma potential, V_{bias} is the bias voltage on the filaments and V_{filament} is the voltage drop across the filaments. The filament bias voltage was set to be 0, -10, -30 and -50 V, respectively, and the corresponding E_{inj} was estimated as 15, 24, 45 and 65 eV.

The plasma potential drops when the injected electron current is turned on (Fig. 4.11a), but the reduction in the plasma potential with increasing injected electron energy is much smaller. This is thought to be because the reduction in plasma potential is associated with the amount of extra negative charge injected into the plasma, which varies with the electron injection current more strongly than with injected electron energy.

T_x decreases from 3.1 eV in the absence of injected electrons (E_{inj}=0 eV case) to 2.6 eV when

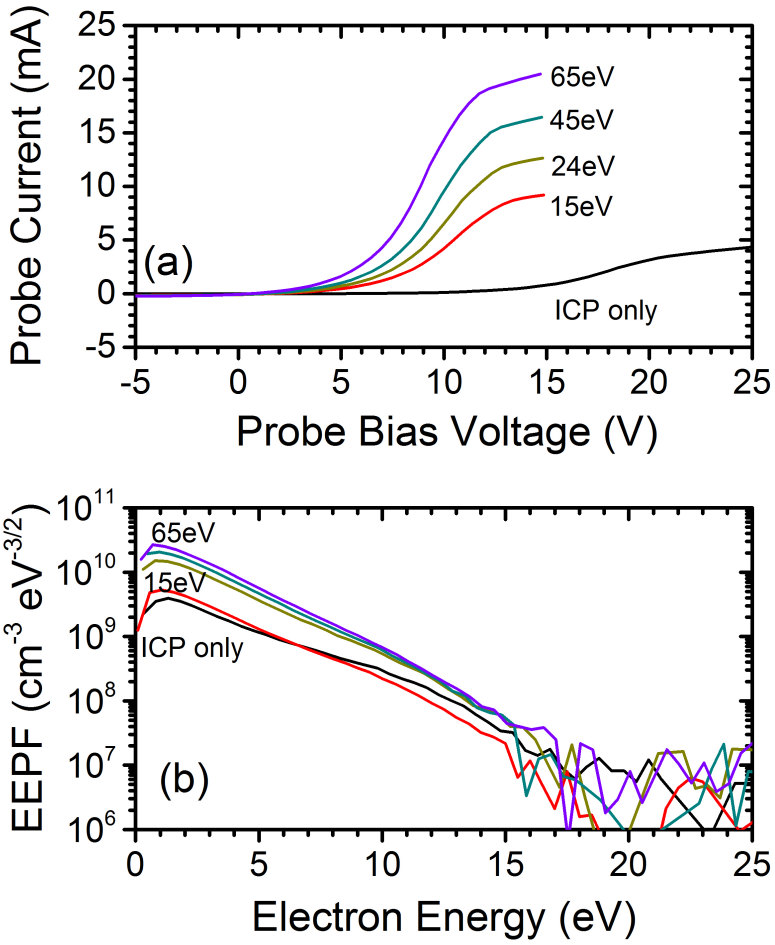

Figure 4.11: Langmuir probe $I-V$ traces and derived EEPFs ((EEDF/$\sqrt{E}$)) for an Ar ICP (100 W, 15 mTorr) with electron injection (1 A) as a function of injected electron energy.

15 eV electrons are injected, but only changes an additional 0.3 eV as the injected electron energy increases from 15 eV to 65 eV (Fig. 4.12b). Meanwhile, the EEDF shape parameter x exhibits little dependence on the energy of injected electrons (Fig. 4.12c).

The modification of n_e is dominated by the total power absorbed by the discharge from the injected electrons. The power carried by the injected electrons increases from 0 to ~65 W as the injected electron energy increases from 0 to 65 eV. For this range of injected power, the increment in n_e is from 4 to 18.2×10^{10}cm^{-3} (Fig. 4.12d). A jump in n_e is observed when E_{inj} crosses the argon ionization energy, 15.76 eV.

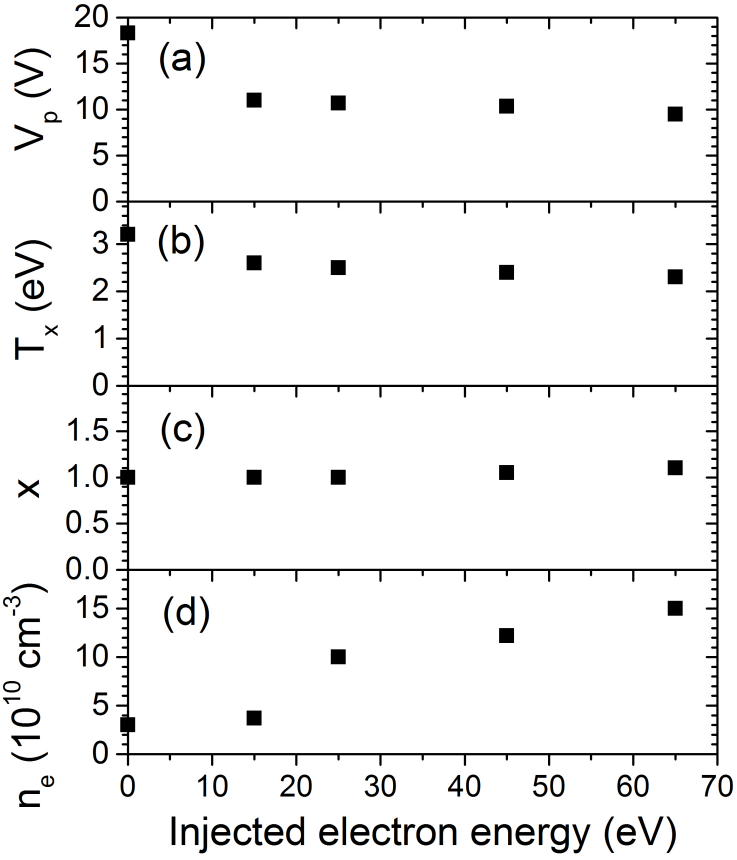

Figure 4.12: EEDF parameters for an Ar ICP (100 W, 15 mTorr) with electron injection (1 A) as a function of injected electron energy, including: (a) plasma potential, V_p, (b) electron temperature, T_x, (c) shape parameter, x and (d) electron density, n_e. The "0 eV" case corresponds to the ICP discharge without electron injection.

4.3.3 Source pressures

Filament electrons (1 A, 65 eV) were also injected into ICP plasmas with different operating parameters to evaluate EEDF modification. The discharge power was fixed at 100 W and the source pressure was varied from 2.5 to 30 mTorr. As shown in Fig. 4.13a, a decrease in T_x with increasing operating pressure is observed for both the ICP-only case (triangle) and ICP with electron injection (square). However, the electron temperature difference (ΔT_x) caused by the injected electrons exhibits little dependence on the discharge pressure (Fig. 4.13a).

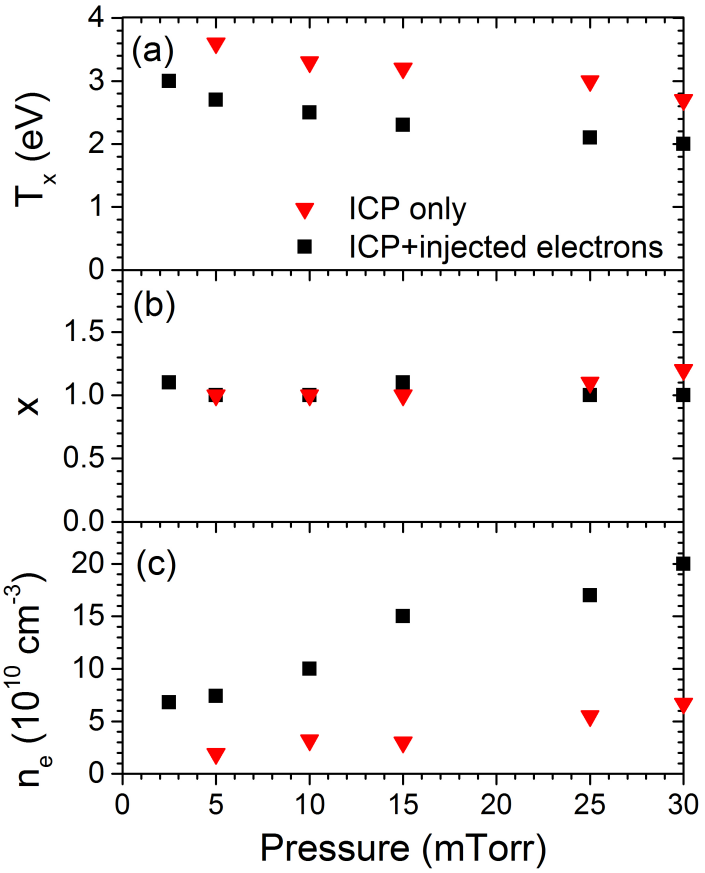

Figure 4.13: EEDF parameters for a 100 W Ar ICP plasma (triangles) and a 100 W Ar ICP plasma with electron injection (1A, 65 eV) (squares) as a function of discharge pressure from 2.5 to 30 mTorr, including: (a) electron temperature, T_x, (b) shape parameter, x and (c) electron density, n_e.

The electron densities of both the ICP only plasma and the ICP plasma with emitted electrons increase with increasing source pressure (Fig. 4.13c). However, the modification of electron density (Δn_e) by the emitted electrons is more significant at higher pressures.

4.3.4 RF power level

At a fixed pressure, the primary effect of increasing RF power levels is to increase the plasma density [82, 37]. In contrast, the electron temperature and the EEDF shape parameter x are expected to remain fairly constant as a function of power. These general trends remain the same when auxiliary

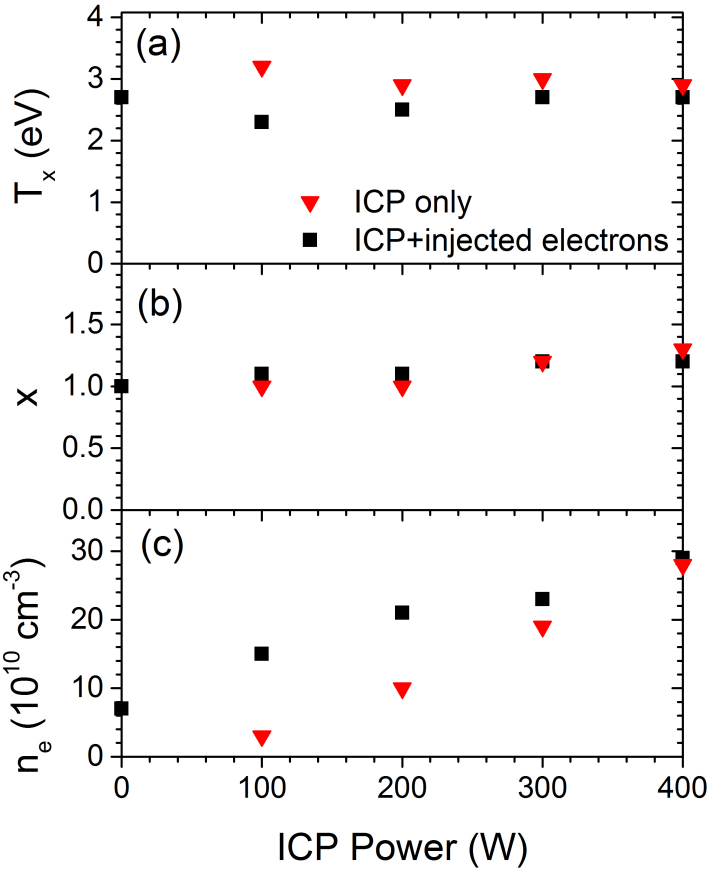

Figure 4.14: EEDF parameters for a 15 mTorr Ar ICP plasma (triangles) and a 15 mTorr Ar ICP plasma with electron injection (1A, 65 eV) (squares) as a function of discharge power from 0 to 400 W, including: (a) electron temperature, T_x, (b) shape parameter, x and (c) electron density, n_e. For "0 W" case, the ICP plasma was turned off.

energetic electrons are injected (Fig. 4.14).

The modification of the 'bulk' EEDF parameters (ΔT_x, Δn_e) by electron injection becomes less significant at higher discharge powers since the relative density of the injected electrons to that of the 'bulk' plasma ($n_{\text{filament}}/n_{\text{bulk}}$) is lower.

4.3.5 Discussion

The Langmuir probe measurements presented here show negligible change in EEDF shape over an energy range of 0 to ~15 eV. The Langmuir probe method is well-suited for determining EEDFs

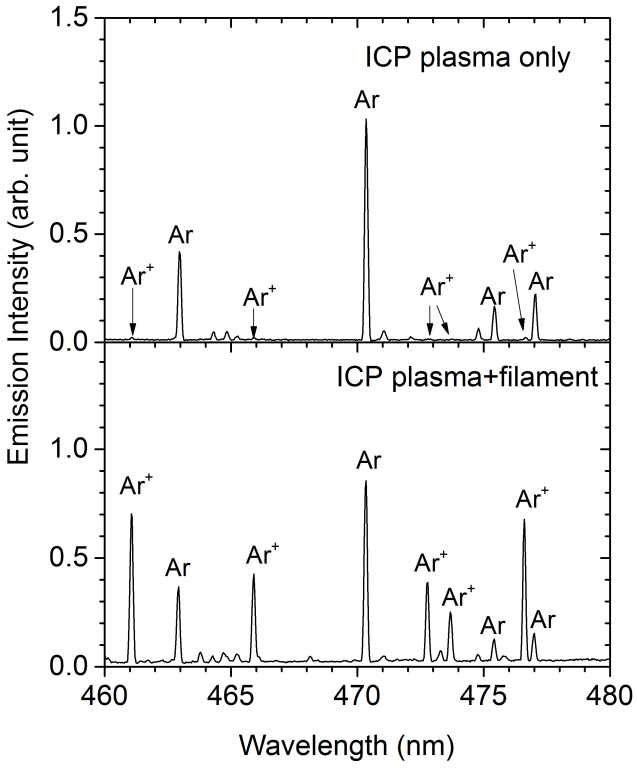

Figure 4.15: Portion of an Ar emission spectra (15 mT, 100 W ICP plasma) with and without injected filament electrons (1 A, 65 eV). Some intense Ar^+ and Ar neutral emission lines are labeled.

in the low electron energy range, but the accuracy diminishes at higher energies. The high energy portion of the EEDF is buried in the probe noise, and therefore cannot be used to characterize the EEDF shape at higher electron energies.

4.4 OES evidence of enhanced high energy tail

OES diagnostic methods are generally quite sensitive to high-energy range of the EEDF due to the high electron excitation threshold energies of Ar neutral (>13 eV) and Ar^+ emitting states (>35 eV) from the neutral ground state. Therefore, Ar emission spectra were recorded to look for qualitative evidence of high energy electrons in the presence of electron injection. Detailed analysis of the tail distribution will be presented in the following chapters.

From recorded Ar emission spectra, evidence of enhanced high energy tails in ICP discharges with injected electrons is observed. As shown in Fig. 4.15, the intensities of Ar^+ emission lines increase by orders of magnitude when energetic electrons are injected. The excitation threshold energies for the Ar^+ emitting states from the neutral ground state is ~35 eV. Therefore, the number of 'hot' electrons with energies greater than ~35 eV increases by orders of magnitude when filament electrons are injected with a sufficiently high filament bias voltage. In principle, these additional 'hot' electrons can result from either a large increase in 'bulk' temperature/density, or an enhanced EEDF tail. If the changes in the Ar^+ emission intensities are attributed to the changes in 'bulk' temperature/density, the intensities of Ar neutral emissions would be expected to increase by orders of magnitude as well, which is not what was observed, i.e., the Ar neutral emission lines only change by 30% or less. Therefore, the change in spectra is attributed to the injected energetic electrons. In the subsequent chapters, the "enhanced tail" EEDFs generated in this way will be used in the evaluation the OES diagnostics.

4.5 Conclusion

The sample OES results illustrate "enhanced tail" EEDFs can be generated by electron injection from heated filaments. The dependence of EEDF tails on the energy and flux of injected electrons cannot be characterized by our Langmuir probe method. Therefore, OES diagnostics will be explored in the widest range of electron injection properties (0-1 A for electron injection current and up to -50 V for filament bias voltage, respectively). The effect of electron injection is more significant when the relative density of the injected electrons compared to the 'bulk' plasma ($n_{\text{filament}}/n_{\text{bulk}}$) is higher. Therefore, the evaluation of OES diagnostics as a function of electron injection properties is conducted in an 100 W, 15 mTorr Ar-containing ICP in which the electron density is low and the optical signal is sufficient for the emission analysis. In addition, the effect of electron injection varies with the 'bulk' dischrage conditions (source pressure and discharge power). Filament electrons (1 A, -50 V bias voltage) will then be injected into Ar ICPs at over a range of 'bulk' discharge pressure (5-35 mTorr) and power (100-400 W) to produce EEDFs used for examining OES diagnostics.

Chapter 5

OES diagnostic of EEDF tail using Ar emissions

Optical emission spectroscopy (OES) is an attractive option for measuring the high-energy tail of EEDFs in low temperature plasmas, since the electron energy thresholds for ground state excitation of rare gas atoms are generally high relative to average electron energies in the electron temperature range of interest (1-10 eV). As discussed in Chapter 2, information about EEDFs in low temperature argon-containing plasmas can be determined from the relative intensities of argon emissions. There are several reasons motivating the use of argon emissions alone in the OES diagnostic for non-Maxwellian EEDFs. First, incorporating only Ar emissions in the emission model analysis is much simpler than modeling emissions from multiple gas atoms, since fewer production and depopulation processes for emitting states need to be considered. Second, the use of Ar emissions has been successfully demonstrated as a means for determining Maxwellian EEDFs and non-Maxwellian EEDFs with depleted tails [52, 117, 51, 59, 74]. The study of measuring enhanced EEDF 'tails' using Ar emissions, presented here, will complement prior work and if successful, will widen the range of applicability. Third, Ar containing plasmas have been widely used in the fabrication of integrated circuits (IC), such as etching [9, 118, 119, 120, 121, 122], deposition [123, 124, 125, 126] and ion implantation [127, 128, 129]. Therefore, diagnostics making use of the spectrum of light emitted by argon in plasmas may be readily implemented on many plasma process tools without perturbing plasma conditions and introducing contaminants.

As discussed in Sec. 4.4, when energetic electrons (∼65 eV) were injected into an ICP discharge (100 W, 15 mTorr), the modified ICP EEDF measured by Langmuir probes was found to be approximately Maxwellian up to an electron energy of ∼15 eV, above which the EEDF could not be resolved due to the noise. However, a large increment in Ar^+ emission intensities when the auxiliary electron source was turned on indicates that there is an additional population of electrons above ∼35 eV (excitation threshold energy of Ar^+ emitting states from Ar neutral ground state). The focus of this chapter is this unknown population of energetic electrons. The approach presented here makes use of independent measurements of the low energy "bulk" portion of the EEDF made with a Langmuir probe so that the OES analysis is used only for the high energy "tail" portion. The emission model analysis (described generally in Chapter 2) has been modified for quantitative determination of EEDF tails. The primary objective is to characterize the capabilities and limitations of the argon-based OES diagnostic for enhanced EEDF tails.

Limitations of the argon emission model in detecting non-Maxwellian EEDFs were already evident in studies of ICP plasmas without injection of energetic electrons [59]. In this case, Langmuir probe measurements showed a "depleted tail" EEDF well represented by the (T_x, x) form. However, OES analysis using the argon $3p^5 4p$ excited states produced a high uncertainty in the value of x, although the T_x values resulting from OES were in good agreement with probe values. OES analysis to determine both x and T_x did succeed when the analysis included emissions from both $3p^5 4p$ and $3p^5 5p$ states. Inclusion of the $3p^5 5p$ states adds spectral lines populated from the argon ground state by collisions with electrons in an energy range for which depletion of the population due to $x > 1$ is significant. This example highlights the importance of using a set of spectral lines with excitation energy thresholds covering the energy range over which the EEDF is to be determined.

The accuracy of the OES-derived EEDFs would ideally be assessed by comparison with an independent measurement. Because the focus of this chapter is the high energy "tail" of the EEDF, the obvious comparison with Langmuir probe measurements is not possible, due to lack of signal for the latter in the energy range of interest. An alternative approach is therefore taken in this study. This approach takes advantage of the ability to control the energy and flux of the auxiliary electrons injected into the ICP. By systematically varying the energy and flux of injected electrons as well as discharge pressure and power, trends in the shape of the tail portion of the EEDF can be compared with expectation based on injected electron characteristics and the effect

of electron neutral collisions. In this way, although the accuracy of the OES approach cannot be directly tested, conditions under which plausible results are obtained can be characterized.

The OES diagnostic implemented in this chapter builds on the emission model analysis which makes use of Ar ($3p^5 4p \rightarrow 3p^5 4s$ and $3p^5 5p \rightarrow 3p^5 4s$) emissions and an '$x$-form' representation of the EEDF [59, 74]. This chapter begins, therefore, with the verification of the presence of energetic electrons through a comparison of OES results for the ICP with and without injected electrons. Knowing the limitations for measuring enhanced EEDF tails from the prior work [59, 74], the OES method was also modified in two ways. First, a mathematical representation of the EEDF allowing for a wide range of shapes is introduced. Second, Ar^+ emission lines which have a high excitation energy threshold and are therefore more sensitive to differences in the EEDF tail are added to the emission analysis.

While values of x between 0 and 1 produce EEDFs with enhanced tail populations compared to a Maxwellian, it is possible that EEDFs will have a shape that does not exactly match the x-form. In the extreme low-collisionality limit, for example, the injected electrons could be clustered close to the average injection energy, appearing as a bump superimposed on the tail of the "bulk" distribution, while in the high-collisionality limit their distribution my be indistinguishable from that of the bulk. In order to capture a range of possible tail EEDFs, from a near-Maxwellian (at higher temperature than the bulk electrons) to a high energy bump, a different mathematical representation called the log-normal distribution is introduced, as described in Chapter 2. Based on the log-normal function, the shape of the distribution is set by adjustable parameters selected to provide a best fit between the predictions of the emission model and the corresponding set of measured emission intensities.

After measuring the tail EEDF while making use of Langmuir probe measurements of the "bulk" portion of the EEDF in the OES analysis, a further investigation explored the use of OES for both "bulk" and "tail" regions of the EEDF. In the latter study, different sets of emission lines are used for the bulk and tail regions, respectively.

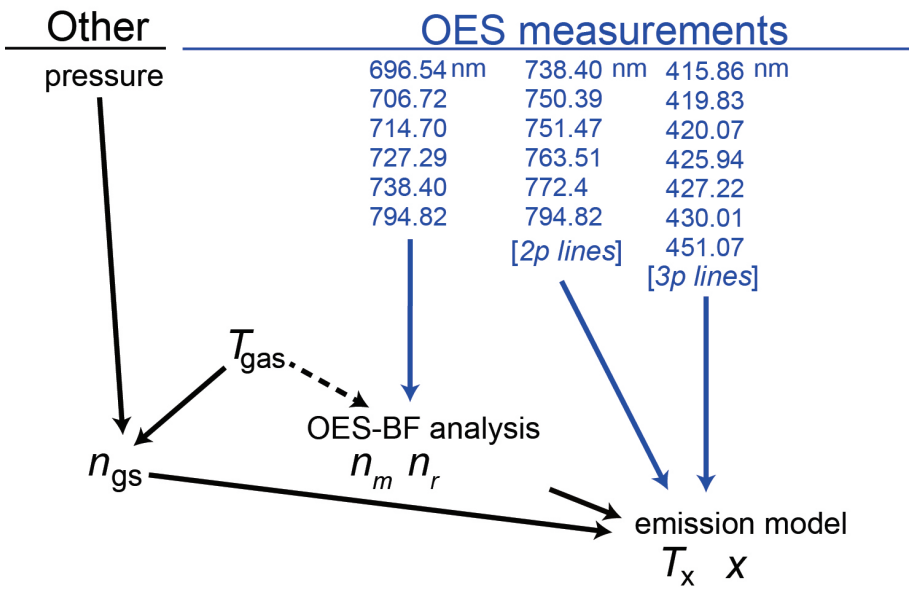

Figure 5.1: Flow chart for OES analysis to determine plasma parameters using Ar $3p^5 4p$ (2p) and $3p^5 5p$ (3p) emissions. A dashed line indicates that the analysis is only weakly dependent on the quantity.

5.1 The use of Ar neutral emissions in OES diagnostic for EEDF tails

The emission model analysis described in Chapter 2 using Ar $3p^5 4p$ and $3p^5 5p$ (also referred as 2p and 3p, respectively) emissions has been adapted for measurements of EEDF tails. Two EEDF representations are used in the emission model: (1) the x-form and (2) the sum of the x-form (for the 'bulk' EEDF) and the log-normal distribution (described in Sec. 2.3.1 for the 'tail' EEDF). Of the two, the x-form has the advantage of only two fit parameters, while the use of the log-normal for tail electrons allows greater flexibility in the EEDF shape, but with greater uncertainty in the result due to the additional fit parameters.

5.1.1 Determining x-form EEDFs using Ar neutral emissions

The extended corona model predicts relative intensities of Ar emissions by combining an assumed EEDF with known excitation cross sections [56, 57, 60, 58, 130] and the number densities of lower levels, including the ground state (n_{gs}) and metastable levels (n_m, n_r), as captured in Eqs. 2.1 and

2.2. The ground state density is estimated from the gas pressure and temperature [59] and the metastable and resonance densities are determined from the emission spectra, based on the degree of radiation trapping as discussed in Section 2.3.2. With these values as model inputs, the EEDF (x, T_x) is determined as that which minimizes the difference (χ^2) between predicted and measured spectra. A flow chart of the analysis showing the general procedure and wavelengths used is shown in Fig. 5.1.

5.1.2 Evaluation of the OES diagnostic with the 'x-form' representation of the EEDF

OES measurements of EEDFs in a 100 W Ar-containing plasma (15 mTorr Ar, 15 mTorr He and 3 mTorr Ne) with electron injection (filaments biased at -50 V) as a function of electron injection current (0, 0.2, 0.4, 0.7 and 1 A) were conducted using the 'x-form' EEDF representation. Langmuir probe measurements were also conducted to serve as a benchmark for the OES results for the low energy range of the EEDF. From these measurements, two aspects of the OES diagnostic are investigated: (1) if the use of Ar neutral emissions alone is adequate to detect the presence of an enhanced EEDF tail, and (2) if the enhanced tail EEDF produced by electron injection is well-characterized by the x-form. In this investigation, a single fit of x and T_x is attempted over the full range of electron energy, encompassing both bulk and tail regions. Because an enhanced tail is expected, the analysis is expected to yield $x < 1$.

The evaluation of this OES diagnostic was conducted in a series of source operating conditions in which the disturbance from electron injection to the 'bulk' discharge becomes more significant gradually. As discussed in Sec. 4.3, the effect of the injected electrons is more significant at a lower ICP power, but at higher injected electron energy and flux. Therefore, the source operating conditions of the sample measurements were selected to be a 100 W Ar-containing plasma (15 mTorr Ar, 15 mTorr He and 3 mTorr Ne) with electron injection (-50 V bias) at a series of filament emission currents (0, 0.2, 0.4, 0.7 and 1 A).

The emission spectra were recorded using a photomultiplier tube (PMT) in conjunction with a monochromator (Fig. 3.2). The EEDFs were determined by analyzing the extracted Ar 2p and 3p emission intensities using the extended corona model (Sec. 2.3).

The emission intensities from selected Ar neutral 2p, 3p and Ar^+ emitting states used in the

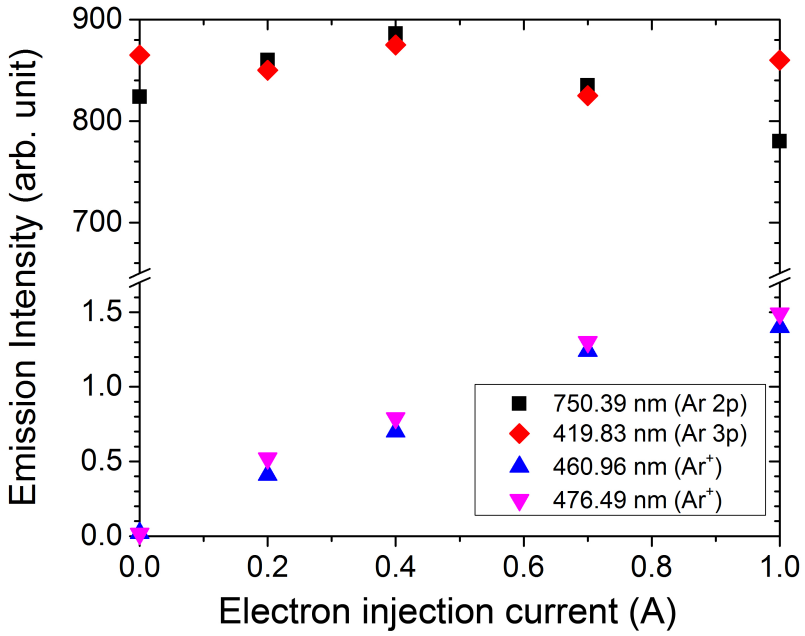

Figure 5.2: Variation of selected Ar emission intensities with the electron injection current for a 100 W Ar-containing plasma (15 mTorr Ar, 15 mTorr He and 3 mTorr Ne) with electro injection (-50 V bias). The plotted 419.83 nm line intensity is scaled by a factor of 50.

emission analysis are plotted as a function of electron injection current (Fig. 5.2). As seen in Fig. 5.2, the Ar neutral 2p (750.39 nm) and 3p (419.83 nm) emissions are essentially independent of the electron injection current, suggesting these lines are mainly excited by electrons in the 'bulk' portion of the EEDF. On the other hand, the Ar^+ emissions which has high excitation threshold energies (~35 eV) increase as the electron injection current increases, indicating the presence of more energetic electrons.

The EEDF measurements at two extreme electron injection current cases (0 and 1 A) are presented as sample results. For the ICP only case, the OES measurement yields T_x=3 eV, x=1.4. The sensitivity of the OES-derived T_x and x can be seen by examining the χ^2 difference between the model and experimental line ratios as a function of T_x and x used in the model calculation (Fig. 5.3a). The estimated uncertainty is ±0.1 eV for T_x and ±0.1 for x (for a ±10% increase in the value of minimum χ^2). When the energetic electrons (1 A, -50 V bias) are injected into the plasma, the OES measurement yields T_x=1.5 eV, x=0.7, which implies an enhanced EEDF tail relative to

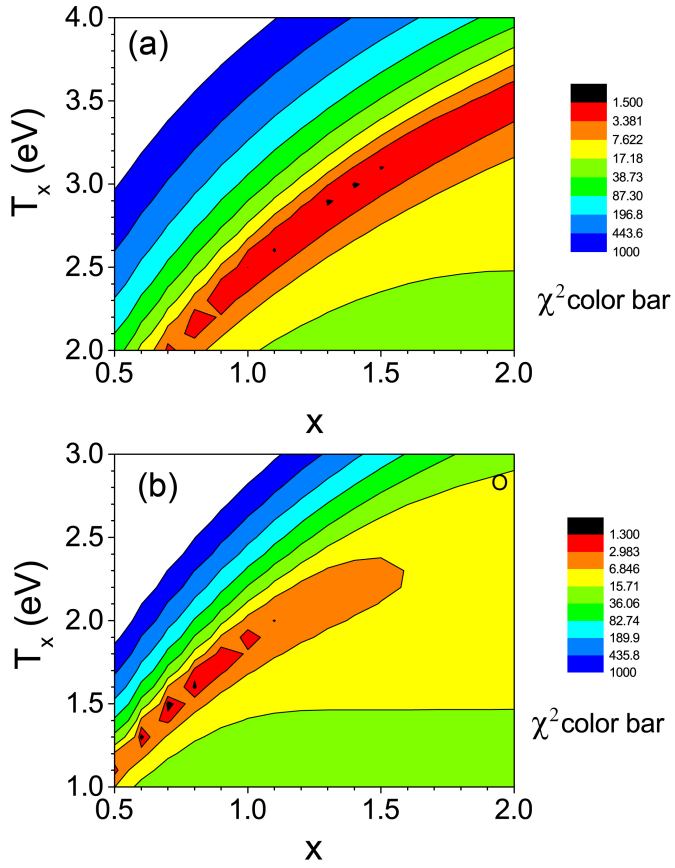

Figure 5.3: Contour plot of χ^2-values in OES fitting process for 100 W Ar-containing plasma (15 mTorr Ar, 15 mTorr He and 3 mTorr Ne) (a) without electron injection and (b) with electron injection (1A, -50 V filament bias). The lower χ^2 values correspond to a better quality fit.

the Maxwellian distribution. The sensitivity of the OES-derived T_x and x is about ± 0.2 eV for T_x and ± 0.1 for x by examining the contour plot of Figure 5.3b.

The EEDF results obtained from the probe and OES method are compared in Fig. 5.4. As seen in Fig. 5.4, Langmuir probe measurements are well suited for determining EEDFs in the 0-20 eV energy range of the EEDF, but the energy dependence above 20 eV cannot be resolved due to noise. The EEDFs generated by the OES-derived T_x and x are in arbitrary unit. For plotting with the probe EEDF results, the overall magnitude of the OES-derived EEDFs are set using the electron density obtained from the probe. For the ICP only case, the OES result generally agrees with the probe measurement (Fig. 5.4a). Both the OES and the probe results exhibit EEDFs with 'depleted tail'. For 1 A electron injection current case, the EEDF with enhanced high energy tail

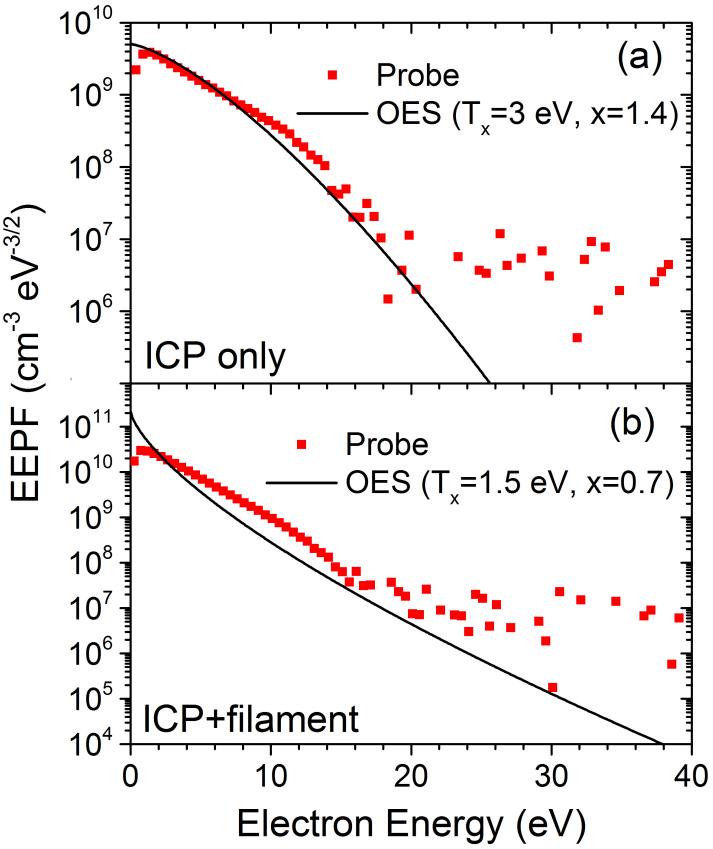

Figure 5.4: EEDFs for a 100 W Ar-containing plasma (15 mTorr Ar, 15 mTorr He and 3 mTorr Ne) with and without electron injection (1 A, -50 V bias). Squares are from probe values, and the line is the OES results.

generated using x<1 does not agree with the probe result (Fig. 5.4b). The χ^2 difference between the raw probe measurement and the OES-derived x-form fit in the 0-20 eV energy range can be used as a quantitative measure of goodness of the OES results. To distinguish this χ^2 analysis from the one used in the OES fitting process, it is referred as χ_0^2. The χ_0^2 value for the 1 A electron injection current case is $\sim 10^3$ which is orders of magnitude larger than the value for the ICP only case ($\chi_0^2 \simeq 10$), indicating the OES measurement is inconsistence with the probe values for the 1 A electron injection current case. Similar inconsistence between the probe EEDF results and the OES-derived x-form EEDFs were observed for all the other electron injection current cases (0.2, 0.4, 0.7 A) as well. Therefore, the conclusion of this study is that the generalized 'x-form' (x, T_x)

is not suited to describing EEDF tails produced by electron injection.

5.1.3 Describing EEDF as the sum of 'bulk' + 'tail' component

In order to expand the range of tail EEDF shapes in the OES analysis, a log-normal distribution (Eq. 2.5) is used here to represent EEDF tails, in combination with an x-form fit for the bulk electrons based on probe measurements. Using the OES diagnostic to determine both the 'bulk' and the 'tail' EEDF will be addressed in subsequent chapters.

Langmuir probe characterization of EEDFs produced by the modified ICP source (Chapter 4) shows that the 'x-form' works well for describing the low energy energy ($\lesssim$15 eV) of these EEDFs. The x-form representation of the 'bulk' EEDF was fitted to the raw probe measurements in the 0-20 eV energy range.

There are three free parameters in the log-normal distribution to describe EEDF tails: (1) tail electron density (n_{tail}), (2) the shape parameter (s) and (3) the cutoff energy of the tail (E_{cut}). It is difficult to uniquely determine these 3 free parameters simultaneously. The approach used here is to fix one of the three parameters at a selected value based on physical reasoning, while the other two are regarded as variables and determined from the analysis of emission intensities. For example, if we assume the energy of injected electrons cannot exceed the maximum potential difference between the filaments and the center of the discharge, E_{cut} can be fixed based on the knowledge of the filament settings (i.e., bias voltage and heater voltage) and the plasma potential. Therefore, in that case, only the density and the shape of the EEDF tail need to be determined.

5.1.4 OES diagnostic with tail electrons represented by log-normal distribution

The emission spectra for Ar-containing ICP with electron injection as a function of electron injection current recorded in Sec. 5.1.2 were re-analyzed using the modified emission model which makes use of Ar neutral emissions and the log-normal EEDF tail representation. From the analysis results, whether the use of Ar neutral emissions in the OES diagnostic allows detection of the presence of an enhanced EEDF tail is examined. Probe measurements of the 'bulk' EEDFs (T_x, x and n_e) are used in the emission model analysis to determine the EEDF tail distributions (Table 5.1).

The tail density (n_{tail}) is regarded as the only variable in the OES analysis to determine the EEDF tail distribution. The cutoff energy of the tail (E_{cut}) is fixed at the average energy of emitted

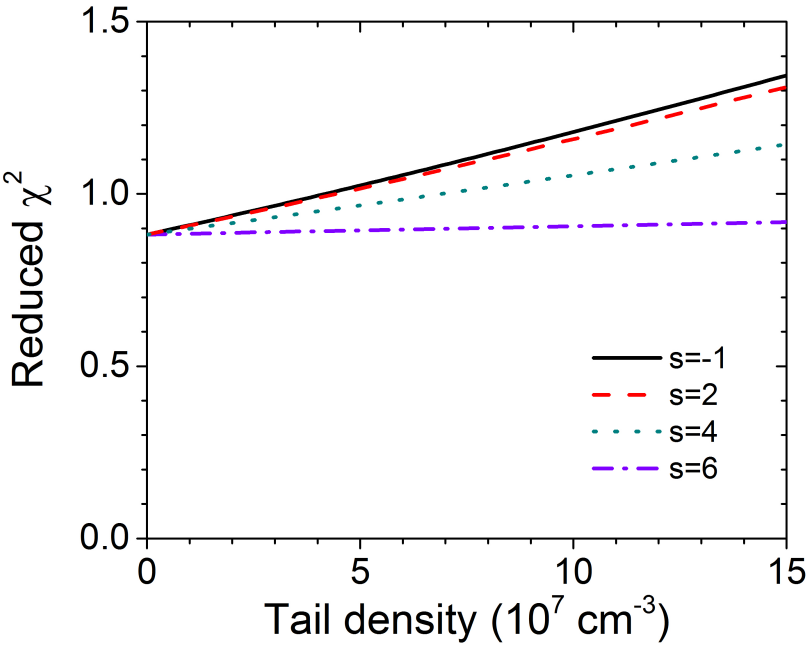

Figure 5.5: Tail density dependence of goodness of fit measure, reduced χ^2 (i.e., χ^2 divided by the number of degree of freedom) at different shape values for a 100 W Ar-containing plasma (15 mTorr Ar, 15 mTorr He and 3 mTorr Ne) with electron injection (1A, -50 V bias).

electrons (65 eV) defined by Eq. 4.1. The emission model analysis was repeated for a sequence of test shape parameter (s) values (i.e., s=-1, 2, 4 or 6) to allow for EEDF tail shapes ranging from a smoothly varying near-Maxwellian to a spike localized near E_{cut}. For the ICP only case, a zero n_{tail} is yielded for all the selected tail shapes, which indicates the absence of an enhanced tail. However, for the ICP discharge with electron injection (i.e., 0.2, 0.4, 0.7 and 1 A) in which evidence of an enhanced EEDF tail has been observed, a value of zero for n_{tail} is also extracted at all the selected tail shapes. For example, n_{tail}=0 for 1 A electron injection current was derived from the emission analysis by examining Figure 5.5 which plots the χ^2 difference between the model and experimental line ratios as a function of the tail density used in the model calculation. The minimum χ^2 values, corresponding to the best fit, are localized at n_{tail}=0 for all the selected shapes. Therefore, the use of Ar neutral emissions in the OES diagnostic is not capable of detecting enhanced EEDF tails in the ICP discharge with electron injection over the operating conditions tested in the present experiment.

Table 5.1: Plasma parameters in 100 W Ar-containing ICP (15 mTorr Ar, 15 mTorr He and 3 mTorr Ne) with electron injection (-50 V filament bias) as a function of electron injection current. The number densities listed are only for Ar. The deceased ground state density is caused by the decreasing gas temperature as the electron injection current increasing.

parameter	0 A	0.2 A	0.4 A	0.7 A	1 A
T_{gas} (K)	540	580	610	625	650
n_0 (Ar) (10^{13} cm^{-3})	21.5	20.	19	18.6	18
OES-BF					
n_m (Ar) (10^8 cm^{-3})	503	340	345	314	360
n_r (Ar) (10^8 cm^{-3})	220	80	94	80	106
probe EEDF					
V_p (V)	18.6	14.5	10.9	10.4	8.7
n_e (10^{10} cm^{-3})	3.5	5	8.5	15.1	18.2
T_x (eV)	3.5	3	2.9	2.7	2.5
x	1.3	1.2	1.2	1.1	1.1

5.1.5 Discussion

Having seen the limitations of this OES diagnostic, it is worth considering why the use of Ar 2p and 3p emissions fail to detect the enhanced EEDF tail. As described in Sec. 2.2, the emission intensity depends on multiple plasma parameters, including the ground state density (n_0), metastable and resonance densities (n_m and n_r) and the EEDF. When 'hot' electrons are injected, not only an enhanced EEDF tail is present, but the other parameters are also modified (see Table 5.1). The changes in the 'bulk' EEDF have been discussed in Sec. 4.3.1. Changes in all of the plasma parameters listed in Table 5.1 except for V_p affect the Ar 2p and 3p emission intensities.

An examination of these effects leads to the conclusion that the observed changes in the Ar 2p and 3p emission intensities are dominated by the changes in 'bulk' plasma parameters resulting from auxiliary electron injection rather than the effect of an enhanced EEDF tail. For example, Fig. 5.6 shows the relative intensities of selected Ar 2p and 3p emissions for ICP discharge only and with 1 A electron injection (-50 V filament bias) in which the disturbance from electron injection to the emission intensities is most significant. The 750.39 and 751.47 nm lines are dominated by ground state excitations, with an energy threshold of ∼13 eV. If the presence of an enhanced EEDF tail was the only effect of electron injection, the intensities of these two lines is expected

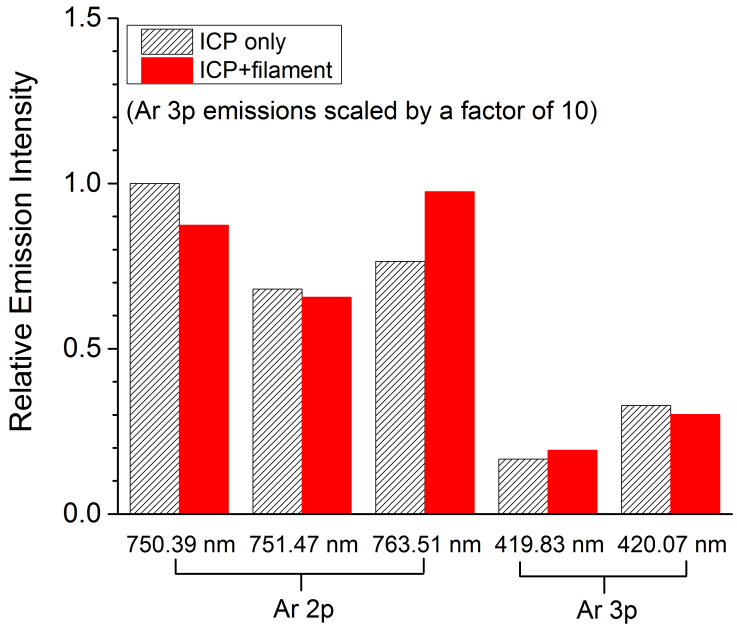

Figure 5.6: Relative emission intensities of selected Ar 2p and 3p emission lines for a 100 W Ar-containing ICP (15 mTorr Ar, 15 mTorr He and 3 mTorr Ne) with and without electron injection (1A, -50 V bias). All the emission intensities plotted are normalized to the intensity of the 750.39 nm peak for ICP only case.

to increase. However, the decrease in these emission intensities is attributed to a corresponding decrease in electron temperature (T_x) (see Table 5.1). As seen in the EEDFs obtained from the probe for 1 A electron injection current (Fig. 5.7), the number of electrons with energies above excitation thresholds of Ar 2p (∼13 eV) and 3p (∼15 eV) is dominated by the x-form 'bulk' EEDF while the enhanced EEDF tail produced by electron injection is smaller than the noise level of the probe results. Another observation is that the intensity of the 763.51 nm line, which is dominated by excitations from metastable levels with ∼2 eV threshold energies, increases most among the Ar 2p and 3p emissions when 'hot' electrons are injected, even though under these conditions, the metastable density decreases significantly. This is an indication of an abundance of 'low' energy electrons rather than of 'hot' electrons, attributed to an increased n_e together with a decreased T_x (see Table 5.1). Furthermore, the ground state excitation threshold energies (∼15 eV) for 3p emissions (i.e., 419.83 nm) are higher than those (∼13 eV) for 2p emissions (i.e., 750.39 and 751.47 nm). Therefore, in the presence of an enhanced EEDF tail, the intensities of 3p emissions

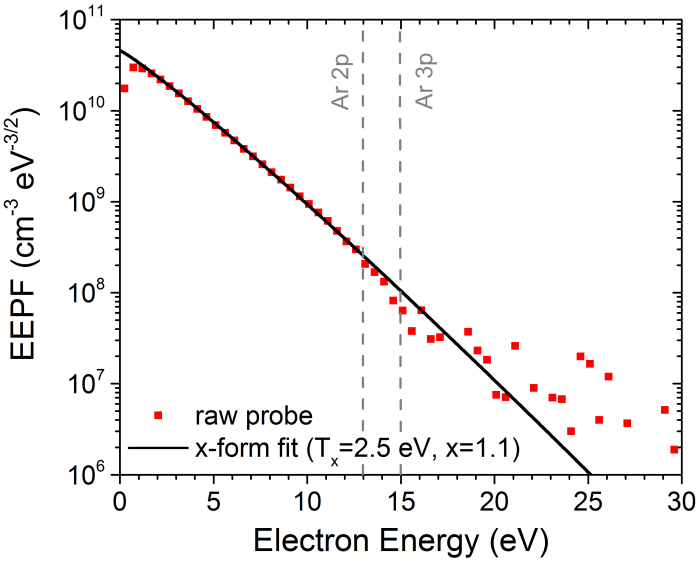

Figure 5.7: EEDF results for a 100 W Ar-containing ICP (15 mTorr Ar, 15 mTorr He and 3 mTorr Ne) with electron injection (1A, -50 V bias). Squares are the raw probe results. Line is the fitted x-form result. Vertical gray lines show approximate ground state excitation threshold energies for Ar 2p and 3p emissions.

are expected to increase more than those of the 2p emissions. The changes in the 419.83 nm line intensity does increase, but the difference between 2p and 3p emissions is not dramatic. From the qualitative analysis of Ar 2p and 3p emissions above, for the source operating conditions tested, the changes in selected Ar 2p and 3p emission intensities are not dominated by the effect of an enhanced EEDF tail.

The effect of enhanced EEDF tails on the Ar 2p and 3p emission intensities can be estimated quantitatively by calculating the contributions from the electrons in the 'bulk' and the 'tail' portion of the EEDF. Based on an analysis to be presented later, n_{tail}=17×10^7 cm^{-3}, E_{cut}=65 eV, s=4.4 are thought to be good description for the EEDF tail for 1 A electron injection current case. The 'bulk' EEDF parameters for 1 A case obtained from the probe are listed in Table 5.1. From the results calculated using the emission model (Fig 5.8), it is observed that the intensities of 2p and 3p emissions are determined by the 'bulk' EEDF (T_x, x, n_e) rather than the EEDF tail distribution. Therefore, it is difficult to extract information about enhanced EEDF tails from just Ar 2p and 3p emission lines for the tested source operating conditions.

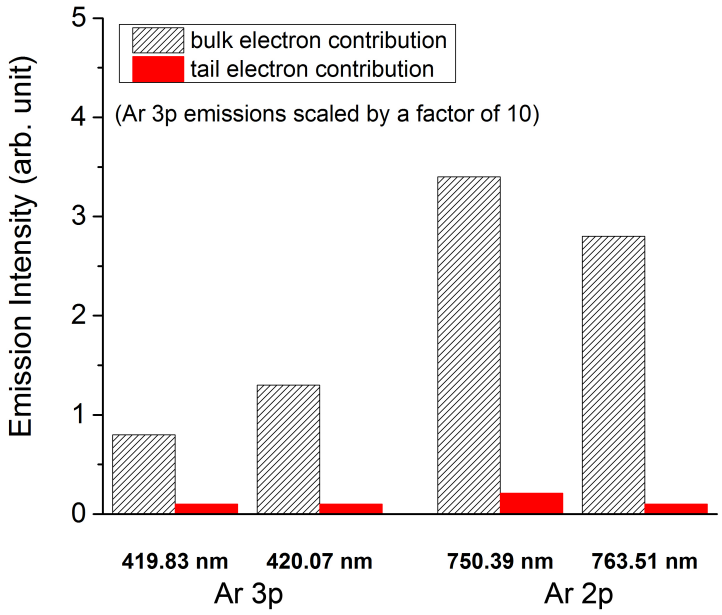

Figure 5.8: 'Bulk' and 'tail' EEDF contributions for selected Ar 2p and 3p emission lines for a 100 W Ar-containing ICP (15 mTorr Ar, 15 mTorr He and 3 mTorr Ne) with and without electron injection (1A, -50 V bias).

5.2 OES diagnostic for EEDF tails using Ar neutral and Ar^+ emissions

Considering the relatively low excitation energy levels for Ar neutral emissions, one possible improvement to the OES diagnostic is to include Ar^+ emission lines in the emission analysis. The Ar^+ emission lines have excitation threshold energies (∼35 eV) much higher than Ar neutral emissions (∼13 eV), and therefore are much more sensitive to differences in the EEDF in the energy range of the injected electrons. For example, the Ar^+ emission intensities increase by several orders of magnitude when electrons are injected, while the Ar neutral emission intensities change little (Fig. 4.15). This suggests that more information about enhanced EEDF tails can be extracted by using Ar^+ emissions in addition to Ar neutral emissions in the OES analysis. Using a log-normal representation of the EEDF tail in combination with the x-form for the bulk, success of the OES analysis will be evaluated by examining trends as injected electron parameters are varied.

5.2.1 Adapting the emission model to include Ar^+ emissions

In order to include Ar^+ emissions to the emission model, the populating and depopulating processes of Ar^+ emitting states must be considered. In contrast to the Ar neutral excited levels, an Ar^+ emitting state can be reached by either excitation from the neutral ground state,

$$Ar + e^-(E > 35\ eV) \rightarrow Ar^{+*}\ , \tag{5.1}$$

or excitation from the ion ground state,

$$Ar^+ + e^-(E > 19.5\ eV) \rightarrow Ar^{+*}\ . \tag{5.2}$$

For a Maxwellian EEDF in a typical low-temperature plasma (T_e <10 eV), there are very few electrons with the 35 eV required for the simultaneous excitation and ionization process (Eq. 5.1). However, for EEDFs with enhanced tails, the contributions from both excitation channels need to be taken into account. The excitation cross sections of Ar^+ emitting states from the neutral and the ion ground states can be found in Ref. [56, 97, 131]. The Ar^+ ground state density is assumed to be equal to the electron density, which is obtained from Langmuir probe measurements. In principle, neutral and ion argon metastables can also be excited into the Ar^+ emitting states. However, these two mechanisms are neglected in this emission model since the density of Ar neutral and ion metastables are sufficiently small compared to the ground state densities. In addition to the electron-impact excitation processes, there are two other mechanisms which are important for modeling Ar neutral emissions: (1) radiation trapping and (2) electron quenching (described in Chapter 2). Since the densities of Ar ion metastables are small, the radiation trapping is neglected. Lastly, electron quenching can be neglected as the radiative lifetimes of Ar^+ emitting states are short such that depopulation of Ar^+ emitting states is overwhelmingly dominated by radiative decay.

5.2.2 Determining EEDF tails using the emission model

The procedure of determining EEDF tails and the wavelengths of Ar and Ar^+ emissions used are summarized in Fig. 5.9. In order to prevent the emission model analysis from being dominated by

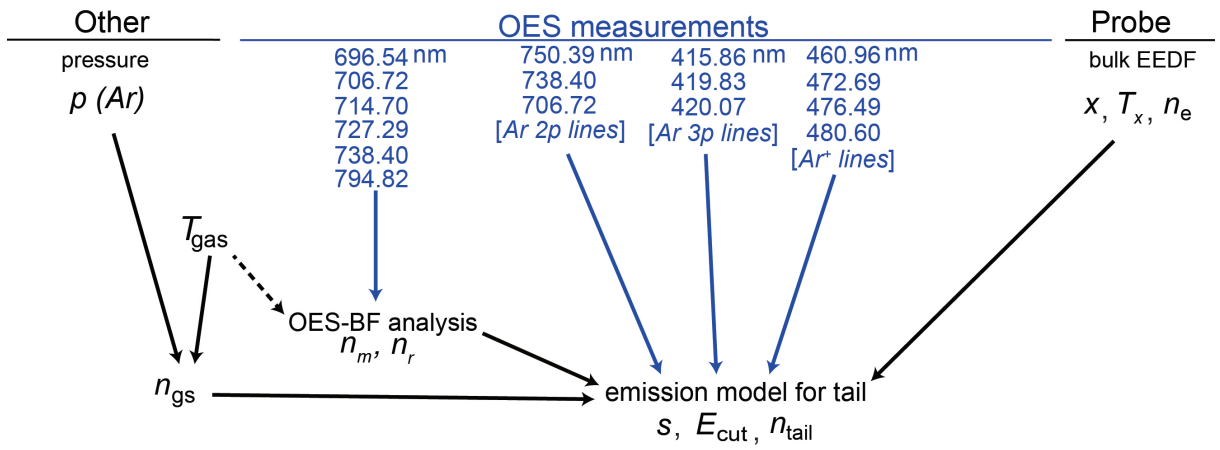

Figure 5.9: Flow chart for OES analysis using both Ar neutral and Ar^+ emission lines. The bulk EEDF is determined from with a Langmuir probe and used in the EEDF tail determination.

Ar neutral emission lines, a similar number of Ar 2p, 3p and Ar^+ emission lines are employed. The 'bulk' EEDF obtained from Langmuir probe measurements are used when fitting the OES results to obtain the EEDF tails.

5.2.3 OES measurements of enhanced EEDF tails

A sequence of tests were conducted to evaluate the OES diagnostic. The initial test was using the OES diagnostic to look for an absence of tail electrons ($n_{\text{tail}} = 0$) for the ICP only case, and $n_{\text{tail}} \neq 0$ for cases including electron injection. The second test was to quantitatively measure the n_{tail} variation as a function of electron injection current, and compare the trend with expectation based on physical reasoning. The third test was a more complete characterization of the EEDF tail, which involves simultaneous determination of n_{tail} and s.

Qualitative measurements of n_{tail}. In a initial test of the OES analysis with the inclusion of Ar^+ lines, log-normal fits to EEDF tails were made in a 100 W Ar-containing plasma (15 mTorr Ar, 15 mTorr He and 3 mTorr Ne) with electron injection (filaments biased at -50 V) as a function of electron injection current (0, 0.2, 0.4, 0.7 and 1 A). It is expected that the energetic electron density, $n_{\text{tail}} = 0$ for ICP only case, and $n_{\text{tail}} \neq 0$ when the filaments are turned on.

In order to determine the tail EEDF from emission model analysis, several plasma parameters

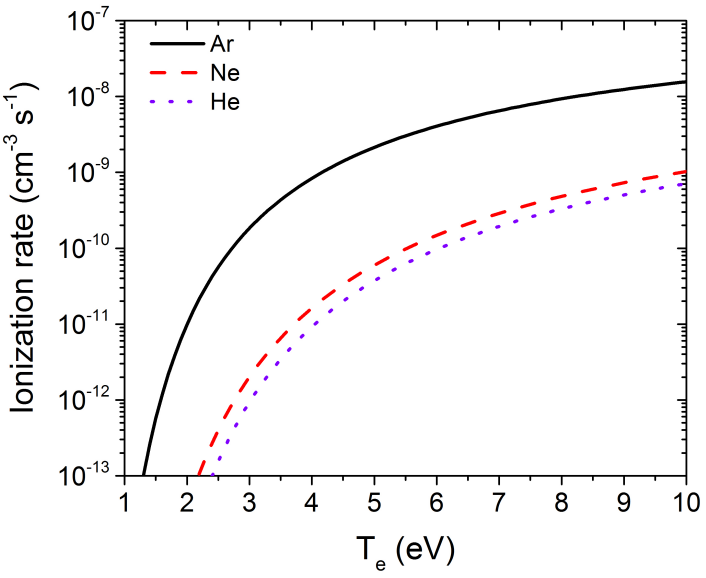

Figure 5.10: Ionization rate for Ar, Ne and He versus electron temperature T_e.

are required as inputs, including the 'bulk' EEDF (T_x, x and n_e), the Ar metastable densities (n_m, n_r) and the Ar ground state density (n_0). Since the Ar ionization rate is orders of magnitude higher than Ne and He when the electron temperature is in 1-10 eV range (Fig. 5.10), the measured electron density is assumed to be a good estimate for the Ar^+ ground state density, even in the mixed-gas plasma. From the Langmuir probe measurements of EEDFs, a decrease in the electron temperature (T_x) and an increase in the electron density (n_e) were observed with increasing electron injection current (see Table 5.2).

In this initial test, the tail density (n_{tail}) was treated as the only variable among the three parameters in the log-normal representation of the EEDF tail. The cutoff energy of the tail (E_{cut}) is estimated as the average energy of the injected electrons, defined by the average potential difference between the filaments and the center of the discharge:

$$E_{\text{inj}} = E_{\text{cut}} = e(V_p - V_{\text{bias}} - 1/2\ V_{\text{filament}})\ , \tag{5.3}$$

where V_p is the plasma potential, V_{bias} is the bias voltage on the filaments and V_{filament} is the average voltage drop across the filaments which is ~-10 V. E_{cut} values, held fixed during the OES analysis, are listed in Table 5.2. The emission model analysis was repeated for each case with different shape

Table 5.2: Measured emission model inputs and EEDF tail parameters for 100 W Ar-containing ICP (15 mTorr Ar, 15 mTorr He and 3 mTorr Ne) with electron injection (-50 V filament bias) as a function of electron injection current. Number densities for Ar metastable and resonance levels are from OES branching fraction measurements (Sec. 2.3.2). Number densities for Ar, Ne and He neutral ground state atoms are calculated by ideal gas law based upon gas temperatures and argon partial pressure. V_p is the plasma potential. 'Bulk' EEDF parameters are based on probe measurements using generalized x-form (T_x, x). The ground state density of Ar^+ is estimated by n_e, obtained from the probe. Neon and helium ground state densities are not used in the argon OES analysis.

	Electron injection current (A)				
parameter	0 A	0.2 A	0.4 A	0.7 A	1 A
T_{gas} (K)	540	580	610	625	650
n_0 (Ar) (10^{13} cm^{-3})	21.5	20.	19	18.6	18
n_0 (Ne) (10^{13} cm^{-3})	4.3	5	3.8	3.7	3.6
n_0 (He) (10^{13} cm^{-3})	21.5	20.	19	18.6	18
OES-BF					
n_m (Ar) (10^8 cm^{-3})	503	340	345	314	360
n_r (Ar) (10^8 cm^{-3})	220	80	94	80	106
probe EEDF					
V_p (V)	18.6	14.5	10.9	10.4	8.7
n_e^x / n_0 (Ar^+) (10^{10} cm^{-3})	3.5	5	8.5	15.1	18.2
T_x (eV)	3.5	3	2.9	2.7	2.5
x	1.3	1.2	1.2	1.1	1.1
EEDF tail from OES					
E_{cut} (estimated) (V)	65	69	66	65	64
s (fixed)	4.4	4.4	4.4	4.4	4.4
n_{tail} (10^7 cm^{-3})	0	2.9	5	13.5	17

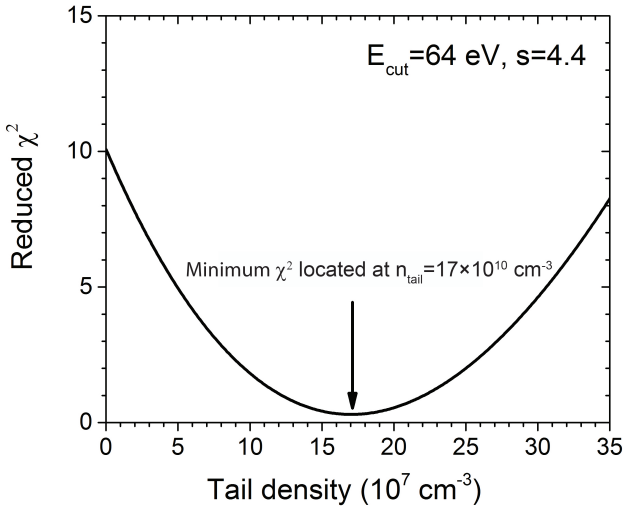

Figure 5.11: Tail density dependence of goodness of fit measure, reduced χ^2 (χ^2 divided by the number of degree of freedom) for a 100 W Ar-containing plasma (15 mTorr Ar, 15 mTorr He and 3 mTorr Ne) with electron injection (1A, -50 V bias).

parameters (s) values (i.e., s=-1, 2, 4 or 6) to allow for EEDF tail shapes ranging from a smoothly varying near-Maxwellian to a spike localized near $E_{\rm cut}$. For all the values of the shape parameter examined, the OES analysis yield $n_{\rm tail}$=0 for the ICP-only case ($I_{\rm inj}$=0 A), which indicates the absence of an enhanced EEDF tail. For the ICP discharge with electron injection (0.2, 0.4, 0.7 and 1 A), non-zero values of $n_{\rm tail}$ were obtained for all the tested tail shapes, indicating the presence of an enhanced EEDF tail.

Quantitative measurements of $n_{\rm tail}$. In the second test, the tail density ($n_{\rm tail}$) was quantitatively determined in a 100 W Ar-containing plasma (15 mTorr Ar, 15 mTorr He and 3 mTorr Ne) with electron injection (filaments biased at -50 V) as a function of electron injection current (0, 0.2, 0.4, 0.7 and 1 A). The energetic electron density, $n_{\rm tail}$, is expected to increase with increasing electron injection current.

Using pre-set $E_{\rm cut}$ (see Table 5.2) and s values, the tail density ($n_{\rm tail}$) can be quantitatively determined using Ar neutral and Ar^+ emissions. Based on an OES analysis to be presented later, there is evidence that s=4.4 produces good EEDF tail results for the tested source operating conditions. As an example, the tail density for 1 A electron injection current is measured to be

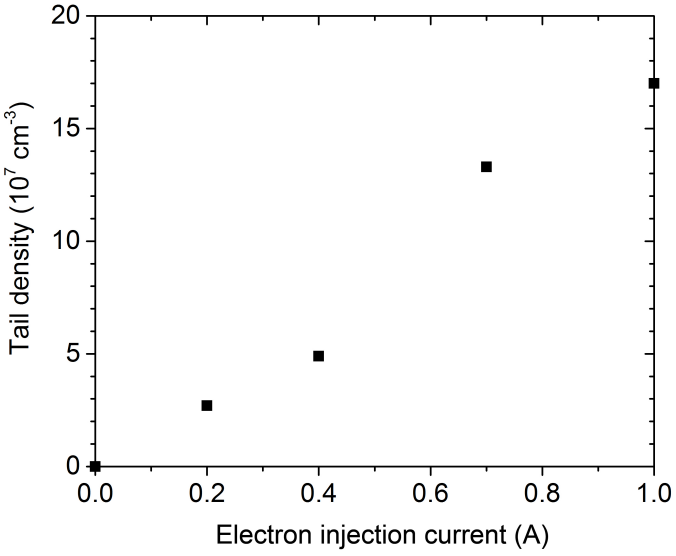

Figure 5.12: OES derived tail density as a function of electron injection current for a 100 W Ar-containing ICP (15 mTorr Ar, 15 mTorr He and 3 mTorr Ne) with electron injection (-50 V bias).

17×10^7 cm^{-3}. The sensitivity of the OES derived tail density can be seen by examining Figure 5.11 which plots the χ^2 difference between the model and experimental line ratios as a function of the tail density used in the model calculation. The minimum χ^2 value, corresponding to the best fit, is well localized in the neighborhood of 17×10^7 cm^{-3}. The uncertainty is about $\pm15\%$ for n_{tail} (for a $\pm10\%$ increase in the value of minimum χ^2).

The OES-derived tail density (n_{tail}) were examined as a function of electron injection current. In principle, the injected electron flux is proportional to the electron injection current. Therefore, as we increase the electron injection current, a higher EEDF tail density is expected. This trend is well reflected in the OES-derived tail density (see Fig. 5.12). The non-Maxwellian EEDF results represented by the sum of the 'x-form' and the log-normal distribution versus electron injection current are plotted in Fig 5.13. The magnitude of the enhanced EEDF tail scales with the electron injection current, as expected.

Simultaneous determination of tail density and shape. The third test is a more complete characterization of the EEDF tail, which might involve simultaneous determination of n_{tail} and s. However, there is not enough information in the Ar neutral (2p and 3p) and Ar^+ emissions to

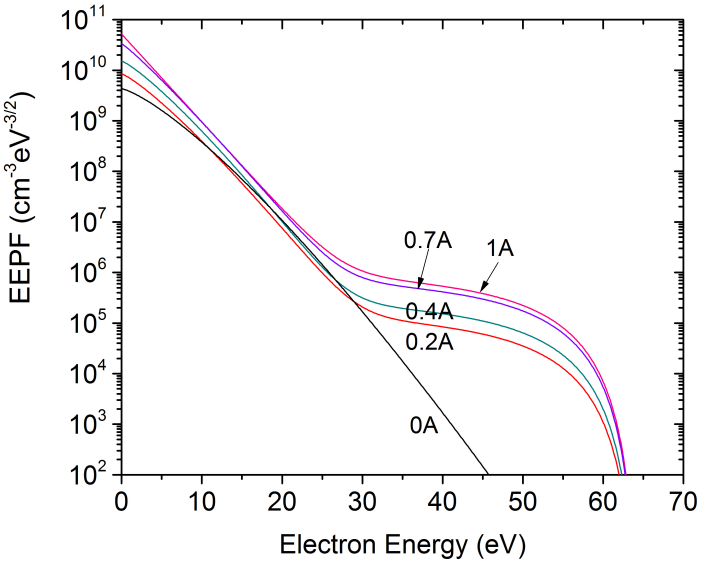

Figure 5.13: EEDFs represented by the sum of 'x-form' and log-normal distribution for a 100 W Ar-containing ICP (15 mTorr Ar, 15 mTorr He and 3 mTorr Ne) with electron injection (-50 V bias) as a function of electron injection current. The 'bulk' EEDFs represented by the 'x-form' are measured using the Langmuir probe (Table 5.2). The 'enhanced EEDF tails' described by log-normal distribution are determined from the OES method.

simultaneously constrain in the values of both s and n_{tail}. This is illustrated in the χ^2 contour plot of Figure 5.14 for the 1 A electron injection current case, which does not exhibit a unique χ^2 minimum. Many trial tail EEDFs described by the pair of parameters running along the line from $n_{\text{tail}} = 2\times10^7$ cm^{-3} and s= -0.8 to $n_{\text{tail}} = 20\times10^7$ cm^{-3} and s= 4.5 have fits of roughly equal quality (within 10% of the minimum χ^2 value). Three pairs of parameters (referred as result A, B and C) in the 'best-fit area' are selected (Fig. 5.14) to generate corresponding EEDF tails. The non-Maxwellian EEDFs which are sum of these OES-derived tail EEDFs and the 'bulk' EEDF (T_x= 2.5 eV, x= 1.1) measured by probe are plotted in Fig. 5.15. The OES measurements yield dramatically different shapes of the enhanced EEDF tails, while the information from Ar neutral (2p and 3p) and Ar^+ emissions is not enough to distinguish between them.

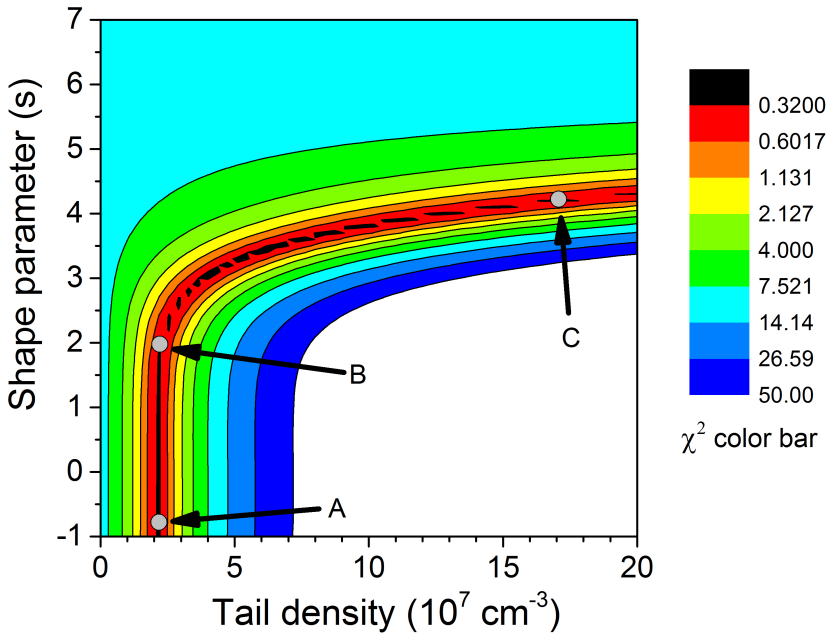

Figure 5.14: Contour plot of χ^2-values for 100 W Ar-containing plasma (15 mTorr Ar, 15 mTorr He and 3 mTorr Ne) with electron injection (1A, -50 V bias). The lower χ^2 values correspond to a better quality fit. Three sets of best fit with dramatic n_{tail} and s values are labeled as A, B and C.

5.3 Discussion

The study presented in this chapter illustrates that the use of the Ar emissions alone in the OES diagnostic is capable of quantitatively determining the density of EEDF tails when other parameters for the log-normal representation are known. The OES diagnostic successfully captured the variation of EEDF tail density (n_{tail}) in a 100 W Ar-containing ICP discharge (15 mTorr Ar, 15 mTorr He and 3 mTorr Ne) with electron injection from 0-1 A, over a range of 0-17$\times 10^7$ cm^{-3} in n_{tail}. However, the information carried by the Ar emissions is not enough to simultaneously determine both the density and the shape of EEDF tails.

Another limitation of this OES diagnostic is that the 'bulk' EEDF used in the emission model analysis is obtained from Langmuir probe measurements. In other words, the diagnostic described in this chapter is not an all-optical diagnostic for non-Maxwellian EEDFs. The study of an all-OES diagnostic for both the 'bulk' and the 'tail' EEDFs will be discussed in subsequent chapters.

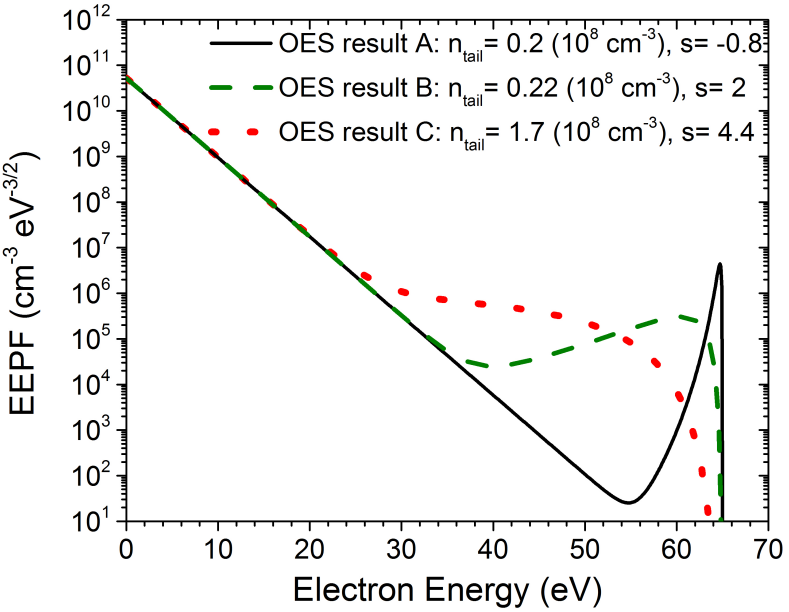

Figure 5.15: EEDFs generated by adding different OES-derived EEDF tails to the 'bulk' EEDF measured by the probe (T_x=2.5 eV, x=1). The three sets of n_{tail} and s results have equally good fits, but correspond to quite different EEDFs.

Considering the capabilities and limitations of using Ar emissions alone to measure enhanced EEDF tails, the OES diagnostic discussed in this chapter is not a tool that can be used to fully determine EEDF tail distributions. However, there are still some possible applications of this OES diagnostic. For example, considering its simplicity and non-invasive nature, this OES diagnostic may be used to qualitatively detect the presence of enhanced EEDF tails in low temperature Ar-containing plasmas used in industrial and laboratory applications. Also, when EEDF tails are partially known/understood, this OES diagnostic may be a good choice to measure the tail density, or capture some relative changes in the tail density.

Chapter 6

OES diagnostic of EEDF tails using Ar, Ne and He emissions

The extended corona emission model is applicable to all rare gases (He, Ne, Kr, Ar and Xe) for which excitation cross sections and other atomic parameters are known. As discussed in Sec. 2.2, Malyshev and Donnelly [132, 78, 77] have developed the trace rare gas optical emission spectroscopy (TRG-OES) method, which makes use of emissions from multiple rare gases to measure EEDFs. In particular, a small amount (∼5% of total feed gas) of He, Ne, Ar, Kr and Xe with known concentrations are added to the other gases used in the plasma. Due to the wide range of excitation threshold energies for ground state excitation of rare gases (23 eV, 19 eV, 13 eV, 11 eV and 9.5 eV for He, Ne, Ar, Kr and Xe respectively), different energy ranges of the EEDF are sampled by studying the emissions from the various atomic species. Therefore, TRG-OES can in principle measure non-Maxwellian EEDFs with complex structures. This TRG-OES method has been used to measure electron temperature (T_e) in Cl_2 [77, 78, 79, 110, 111, 133, 109], O_2 [112, 113], and fluorocarbon-containing [134] ICPs and CCPs. Note that in these measurements, the T_e or EEDF were basically determined from Ar, Kr and Xe emissions, since very little emission was detected from Ne or He due to the limited number of plasma electrons with an energy greater than their higher excitation threshold energies. In some cases, however, such as low power (<∼100 W) Chlorine [110, 111] and Oxygen ICPs [109, 112] and fluorocarbon-containing CCPs [134], the TRG-OES derived T_e values were higher than the Langmuir probe results, indicating the presence of enhanced

high-energy EEDF tails. Under these circumstance, Donnelly *et al.* found an Ne (585.2 nm)-to-Ar (750.4 nm) emission ratio was useful as a qualitative indicator of the relative population of high-energy electrons [112]. Furthermore, Zhu and Pu [114] measured bi-Maxwellian EEDFs (i.e., with "enhanced tail," as described in Sec. 2.3.1) in Ar-containing ICPs at 10 mTorr, 12 W and 200 W using argon and krypton emissions.

As discussed in Chapter 5, the use of Ar neutral and Ar^+ emissions in the emission analysis is not enough to *simultaneously* constrain in the values of both the density and the shape of an enhanced EEDF tail in the OES fitting process. Therefore, in this chapter, Ne and He emissions are also included in the emission analysis to provide more information about EEDF tails. The primary objective is to characterize the capabilities and the limitations of the OES method involving simultaneous use of multiple rare gases for EEDF tails. In this chapter the description of the 'bulk' EEDF will be provided by Langmuir probe measurements. An all-optical method for non-Maxwellian EEDFs where the bulk parameters are also obtained from OES measurements will be addressed in the subsequent chapter.

The OES diagnostic developed in this chapter is intended to provide a *quantitative* determination of enhanced EEDF tails, as compared to a *qualitative* indication as in most of the previous TRG-OES studies. Therefore, the emissions used in this OES method is different from the TRG-OES method. In Chapter 5, we have seen that the OES emission analysis including Ar neutral emissions only is generally not effective in resolving the EEDF tails produced by electron injection, but results improve when Ar^+ emissions are added to the analysis. Here, Ne and He emissions which have excitation threshold energies of ~19 eV and ~23 eV for Ne and He respectively are used to provide information about the 'middle' energy portion of EEDF tails which is missed by using Ar neutral emissions (~13 eV) and Ar^+ emissions (~35 eV). One reason Ne and He emissions are generally not employed in the TRG-OES method is because their intensities are too weak to be accurately measured. This may be attributed to two reasons. First, only small amounts (~1% of total feed gas) of Ne and He were typically added to the reactive gases. Second, the plasmas examined with TRG-OES may not have enough 'hot' electrons to produce sufficient Ne and He emissions. In this study, in contrast to prior reports about the TRG-OES method, large amounts of Ne (10% of total feed gas) and He (45% of total feed gas) were added to make sure their emissions could be detected accurately and employed in the emission analysis. In addition, in preliminary

OES results (Chapter 5), Ar^+ emissions with higher excitation threshold energies than Ne and He were measured and successfully employed in the OES diagnostic. Therefore, sufficient Ne and He emissions are expected from the modified ICP system used for the evaluation of the OES diagnostic.

The OES diagnostic described in this chapter was evaluated in a modified ICP source in which EEDF tails can be controlled systematically (as described in Chapter 4). There are several 'knobs' used to control the EEDF tails, including the electron injection current, filament bias voltage and the 'bulk' discharge conditions (source pressure and discharge power). The changes in EEDF tails have been determined as a function of these control parameters using the OES diagnostic, and the results compared to expected trends in the EEDF tail parameters.

6.1 Determining EEDF tails using the emission model

As a preliminary step to adding Ne and He emissions to the emission model, we consider the processes populate and depopulate Ne and He emitting states. A Ne/He emitting state can be reached by either electron-impact excitation from the neutral ground state,

$$\mathrm{Ne(gs)} + e^-(E > 19\ eV) \rightarrow \mathrm{Ne}^* \ , \tag{6.1}$$

$$\mathrm{He(gs)} + e^-(E > 23\ eV) \rightarrow \mathrm{He}^* \ , \tag{6.2}$$

or by electron-impact excitation from metastable levels,

$$\mathrm{Ne(met.)} + e^-(E > 2\ eV) \rightarrow \mathrm{Ne}^* \ , \tag{6.3}$$

$$\mathrm{He(met.)} + e^-(E > 2\ eV) \rightarrow \mathrm{He}^* \ . \tag{6.4}$$

The electron-impact excitation cross sections for population of Ne and He emitting states from ground state and metastable levels have been well studied [135, 67, 70, 68, 69]. The ground state densities of Ne and He are obtained from their partial pressures and the gas temperature. To include the metastable excitation components, the metastable Ne and He densities are required. In principle, the Ne metastable densities are determined from the emission spectra, based on the degree of radiation trapping (OES-BF) as discussed for argon in Sec. 2.3.2. While this was indeed

done, in the present experiment the Ne metastable density was found to be negligible for the Ar/Ne/He mixed gas plasma. The He metastable density cannot be obtained using the OES-BF method but may be in principle measured by white light optical absorption spectroscopy (OAS) as discussed in Sec. 3.2.2. In practice, however, no metastable He atoms were detected for any of the plasma conditions considered in this chapter. This is in sharp contrast to the Ar metastable levels that are highly populated under these plasma conditions. There are two reasons for this difference. First, the electron energy thresholds for the production of metastable He and Ne levels is higher than that of argon, with correspondingly lower excitation rates. Second, and more importantly, the energies of He and Ne metastable levels are greater than the ionization energy of Ar. Collisions between a metastable Ne and He atom and a ground state Ar atom results in the ionization of the Ar atom and the quenching of the Ne or He metastable atom to the ground state. This *Penning ionization* process [136] is very effective in destroying any Ne and He metastable atoms created in the Ar/Ne/He mixed gas plasma used in this work. The low metastable Ne and He densities simplify the emission model handling of these levels in the present work. First, electron-impact excitation of metastable atoms is neglected. Second, radiation trappings of emissions terminating on metastable levels is negligible. The radiative lifetimes of the Ne and He emitting states are also short enough that electron-quenching can also be ignored for these atoms. These simplifications will not apply to all possible plasma systems, but are generally valid for all the plasma conditions considered in this work.

The procedure for applying the OES analysis to determine EEDF tail parameters using the log-normal representation and the wavelengths of Ar, Ne He emissions used are summarized in Fig. 6.1. Emissions from different species with different excitation threshold energies are employed to provide information about different portions of the EEDF. If the emission model analysis is dominated by emissions from a single species, information carried by emissions from other species is washed out, defeating the purpose of using emissions from multiple rare gases. Therefore, a similar number of Ar neutral, Ar^+, Ne and He emission lines are employed.

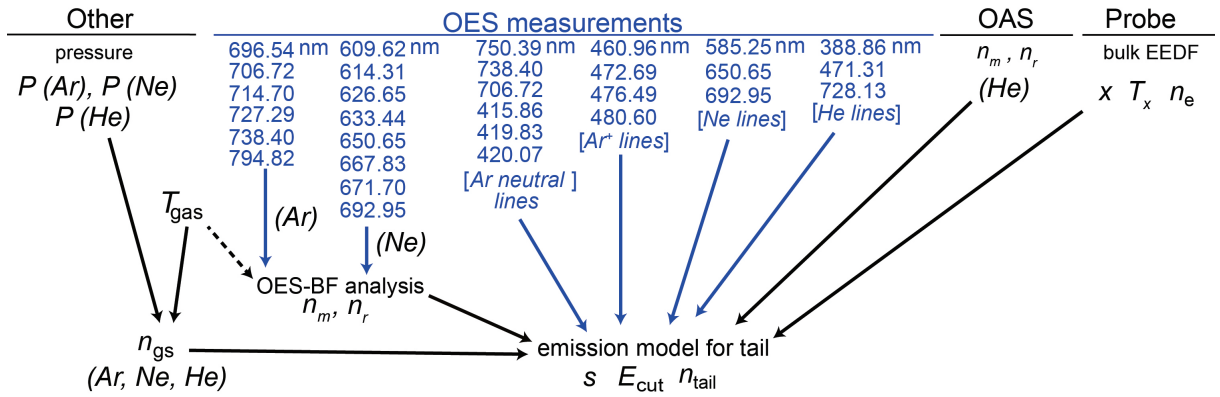

Figure 6.1: Flow chart for OES analysis using Ar, Ne and He emission lines. The 'bulk' EEDF is determined from probe and the He metastable densities are obtained from white light absorption (OAS) measurements.

6.2 Evaluation of the OES diagnostic for EEDF tails using Ar, Ne and He emissions

In this section, improvements when Ne and He emissions are included along with argon emissions in the OES analysis are investigated using OES measurements of the EEDF in the modified ICP source. For illustrating purpose, an overview of the capabilities of the OES diagnostic for one set of plasma condition, i.e., 100 W Ar-containing ICP (15 mTorr Ar, 15 mTorr He and 3 mTorr Ne) with electron injection (1 A, -50 V bias) is presented.

In this effort to measure EEDFs in a ICP with electron injection, the 'total' non-Maxwellian EEDF is characterized by 6 parameters. The three 'bulk' EEDF parameters (T_x, x and n_e) are obtained from fits to the Langmuir probe measurements (see Table 5.2). Of the three 'tail' parameters ($E_{\rm cut}$, s and $n_{\rm tail}$) two are extracted from the OES diagnostic: the tail density ($n_{\rm tail}$) and the shape parameter(s). The remaining tail parameter, the cutoff energy ($E_{\rm cut}$), is estimated from the voltages on the filament power supplies and the voltage difference between the filaments and the center of the plasma. For a bias voltage supply setting of -50 V, this corresponds to $E_{\rm cut}$=64 eV (See Table 5.2). The statistical goodness of χ^2 measure of OES analysis results using different sets of emission lines are presented in contour plots of Figure 6.2. When using Ar emissions only, numerous trial tail EEDFs described by the pair of parameters, $n_{\rm tail}$ and s, have roughly equal

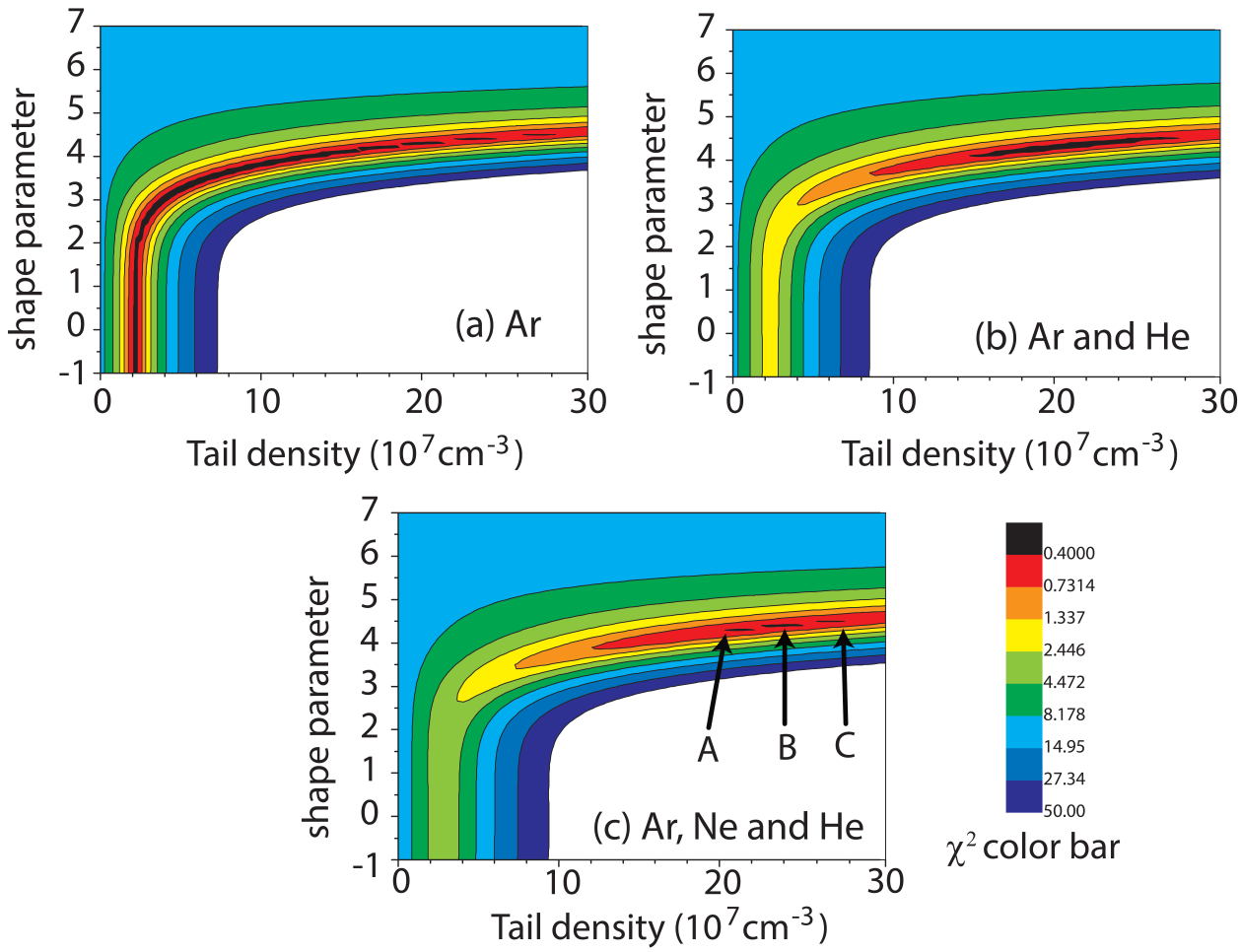

Figure 6.2: Contour plots of χ^2-values in comparing computed and measured emission intensities for a 100 W Ar-containing ICP (15 mTorr Ar, 15 mTorr He and 3 mTorr Ne) with electron injection (1 A, -50 V bias) using (a) Ar emissions alone, (b) Ar and He emissions and (c) a mix of Ar, Ne and He emissions. The smaller χ^2 values (darker area) correspond to a better quality fit. On plot (c), the parameter set (n_{tail} and s) corresponds to the minimum χ^2 is labeled as result B. And the parameter sets on the edges of the 'best-fit area' (within $\pm$10% increase of the value of minimum χ^2) are labeled as result A and C.

quality fits (within 10% of the minimum χ^2 value) to the observed OES line ratios (Fig. 6.2a). For these cases, s ranges from -1 to 4.5, and n_{tail} ranges from 2×10^7 to 28×10^7 cm^{-3} confirming that the argon-only analysis does not yield a unique results. With He emissions included along with argon (no Ne) in the emission analysis, the OES-derived results are better constrained in the range from 15 to 28×10^7 cm^{-3} for n_{tail} and 3.9 to 4.5 for s, respectively (Fig. 6.2b). A mix of Ar, Ne and He emissions (Fig. 6.2c) further improves the discrimination between the trial tail EEDFs.

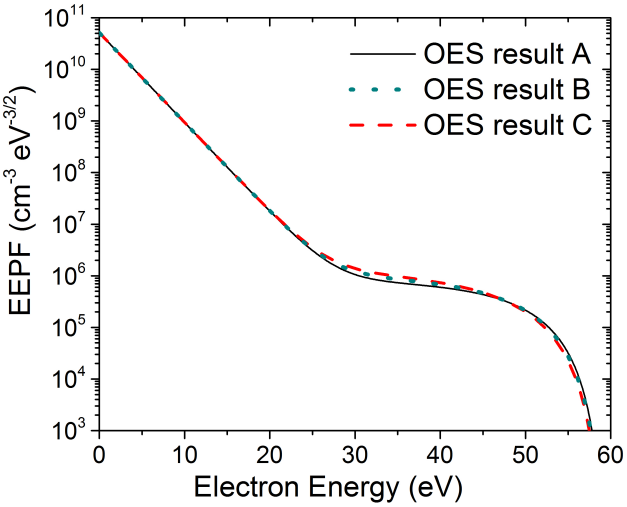

Figure 6.3: EEDFs represented by the sum of 'bulk' and 'tail' EEDF for a 100 W Ar-containing ICP (15 mTorr Ar, 15 mTorr He and 3 mTorr Ne) with electron injection (1 A, -50 V bias). The 'bulk' EEDF represented by the 'x-form' representation is measured by the Langmuir probe. The EEDF 'tails' described by the log-normal distribution are determined from the OES method.

Using all of the Ar, Ne and He lines listed in Fig. 6.1. The minimum χ^2 value which is ~0.3, corresponding to the best fit, is located at 24×10^7 cm^{-3} for n_{tail} and 4.4 for s (labeled as result B in figure 6.2c). The estimated uncertainty is about ±15% for n_{tail} and ±3% for s, respectively (within 10% of minimum χ^2 value). The variation in the tail EEDF parameters associated with these uncertainties hardly affect the shape of the final 'bulk+tail' EEDF. This is illustrated in Fig. 6.3 which includes three EEDFs calculated from bulk EEDF parameters (T_x=2.5 eV, x=1.1) obtained from Langmuir probe measurements along with tail parameters from the center and edges of the 'best-fit area' in the OES analysis (Fig. 6.2c). These three EEDFs show little difference from on another, indicating the shape of the non-Maxwellian EEDF can be robustly defined at least in this case with a high (1 A) electron injection current and resulting large tail component.

The uncertainty in the OES-derived EEDF parameters increases when the electron injection current is smaller. This is demonstrated in the χ^2 contour plot of Fig. 6.4, which shows results of an analysis of the 0.2 A electron injection current case, using all the Ar, Ne and He emission lines. The minimum χ^2 value which is ~2.8, corresponding to the best fit, is located at 0.8×10^7 cm^{-3} for n_{tail} and 3.3 for s (labeled as result B in figure 6.2c). The estimated uncertainty is about ±40%

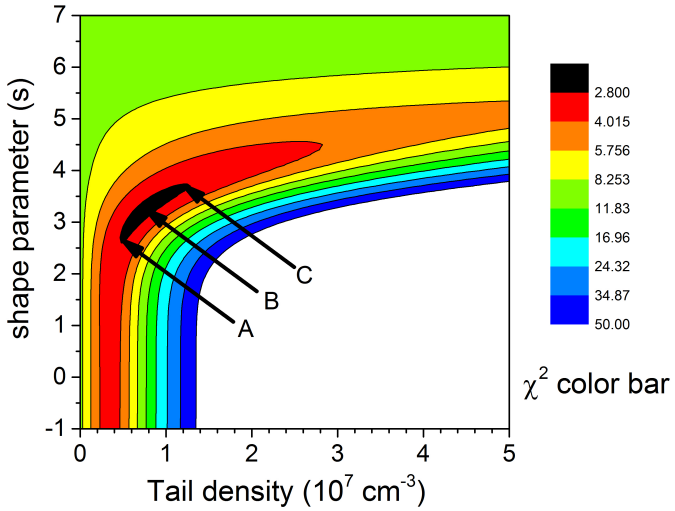

Figure 6.4: Contour plot of χ^2-values in comparing computed and measured emission intensities for a 100 W Ar-containing plasma (15 mTorr Ar, 15 mTorr He and 3 mTorr Ne) with 0.2 A electron injection (-50 V bias). The parameter set (n_{tail} and s) corresponds to the minimum χ^2 is labeled as result B. And the parameter sets on the edges of the 'best-fit area' are labeled as result A and C.

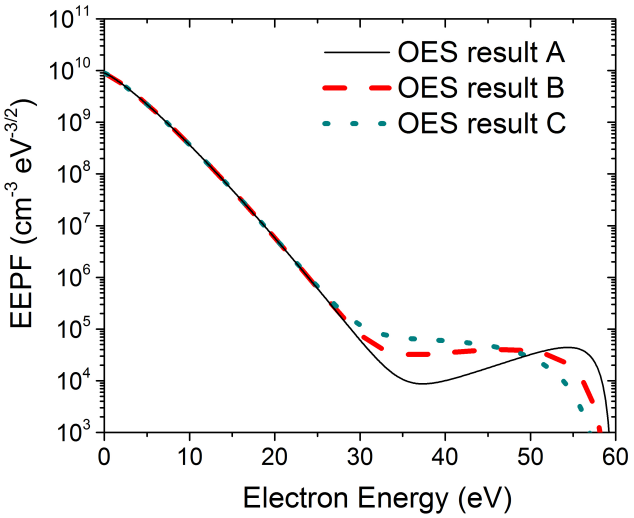

Figure 6.5: EEDFs represented as the sum of 'bulk' and 'tail' EEDFs for a 100 W Ar-containing ICP (15 mTorr Ar, 15 mTorr He and 3 mTorr Ne) with electron injection (0.2 A, -50 V bias). The 'bulk' EEDFs are measured with the Langmuir probe and the EEDF 'tails' are determined from the OES method.

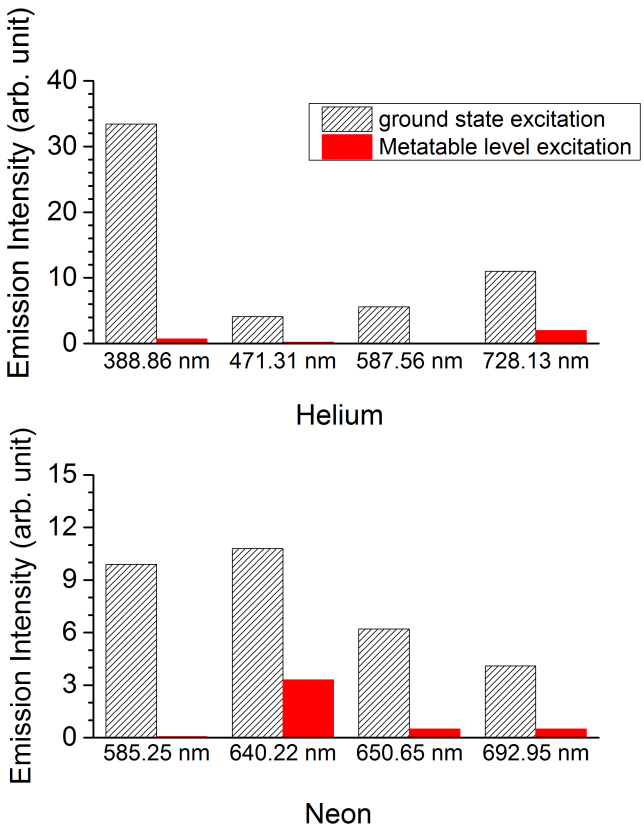

Figure 6.6: Metastable and ground state contributions determined by the emission model for selected Ne and He emission lines for a 100 W Ar-containing ICP (15 mTorr Ar, 15 mTorr He and 3 mTorr Ne) with electron injection (1A, -50 V bias).

for n_{tail} and ±15% for s, respectively (for a ±10% increase in the value of minimum χ^2). The best-fit parameters (labeled as result B) and the pairs of parameters on the edges of the 'best fit area' (labeled as result A and C) in Fig. 6.4 are used to generate the EEDFs shown in Fig. 6.5. Unlike the 1 A filament emission case, the three curves for the 0.2 A case are noticeably different. Nonetheless, a tail is at least observed for all three cases. The larger apparent spread, compared to the 1 A injection case, is partially due to the smaller overall size of the tail component. Indeed, the absolute uncertainty in n_{tail} is in fact smaller at 0.2 A than at 1 A, with uncertainties of $\pm 0.3\times10^7$ cm^{-3} and $\pm 3.6\times10^7$ cm^{-3} for the two cases, respectively. In principle, the OES fitting process can be evaluated by checking the absolute value of the minimum χ^2. However, this is true only when uncertainties are known, including (1) the uncertainties of the emission intensity measurements and (2) the uncertainties in the emission model inputs, such as the known cross sections, the ground state density, metastable and resonance densities. In the present experiment, the latter is neglected since the uncertainties in the emission model inputs have not been examined. The uncertainties of the emission measurements (σ) are accounted in the calculation of the χ^2 value (Eq. 2.7). But σ is simply set to be 3% for all the spectra measurements which may not be correct. For the sample data shown here, a larger minimum χ^2 value (∼2.8) was observed in the 0.2 A case than that (∼0.4) in the 1 A case. This could indicate the OES results are more accurate in the 1 A case than those in the 0.2 A. However, in the 0.2 A case, the uncertainties of the emission measurements (σ) used should have been higher than 3% due to the weak emission signal and thus high relative noise level. Therefore, the absolute value of the minimum χ^2 is not meaningful in the present experiment.

Recall from Section 6.2 that the role of metastable Ne and He atoms was neglected from the OES analysis since their densities were too low to measure. Nonetheless, owing to the unlikelihood of Ne and He atoms excited from the ground state, due to their high excitation thresholds, the contribution of metastable atom excitation may distort the Ne and He emission results when their densities are non-zero but too small to measure. This can be tested by calculating the metastable contributions using Ne and He metastable densities of 0.5×10^8 cm^{-3}, which is the minimum density that can be measured by OAS in the present experiment. The results are shown Fig. 6.6. With the exception of the Ne (640.22 nm) line (which is excluded from the analysis) the Ne and He lines are all dominated by ground state excitation.

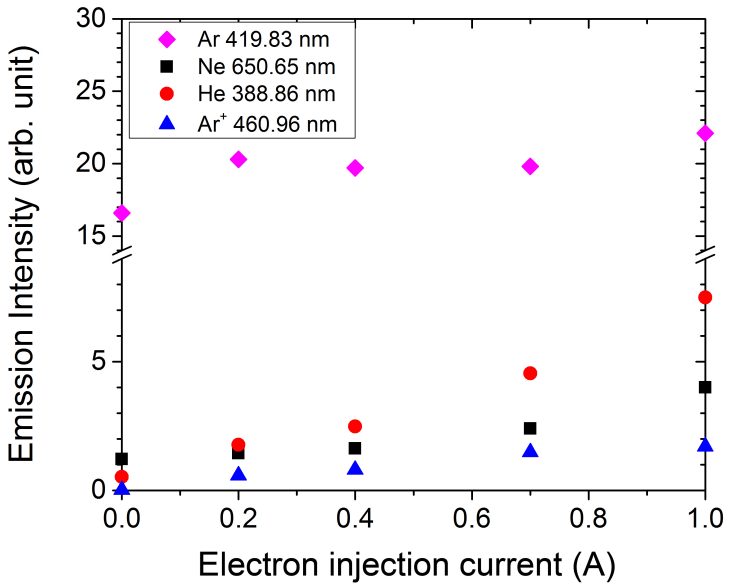

Figure 6.7: Increase in selected Ne He and Ar^+ emission intensities with electron injection current (-50 V), indicates growing population of energetic electrons for a 100 W Ar-containing ICP discharge (15 mTorr Ar, 15 mTorr He and 3 mTorr Ne).

6.3 OES measurements of enhanced EEDF tails

The preceding section gave an overview of the capabilities of the OES diagnostic for one set of plasma conditions. A more comprehensive test of the diagnostic can be obtained by conducting measurements in the modified ICP source as a function of source operating conditions, including (1) electron injection current, (2) filament bias voltage, (3) source pressure, and (4) discharge power. The OES diagnostic can be evaluated by comparing the variation of OES-derived EEDF tails with expectations based on each varied control parameter combined with physical reasoning.

6.3.1 Electron injection current

In the first experiment, the diagnostic is evaluated as a function of electron injection current. Energetic electrons are injected into a 100 W Ar-containing ICP discharge (15 mTorr Ar, 15 mTorr He and 3 mTorr Ne) at a fixed filament bias voltage (-50 V) as a function of the electron injection current (0, 0.2, 0.4, 0.7 and 1 A). The injected electron flux is proportional to the electron injection current. Therefore, the primary expectation is that the electron density of the enhanced EEDF

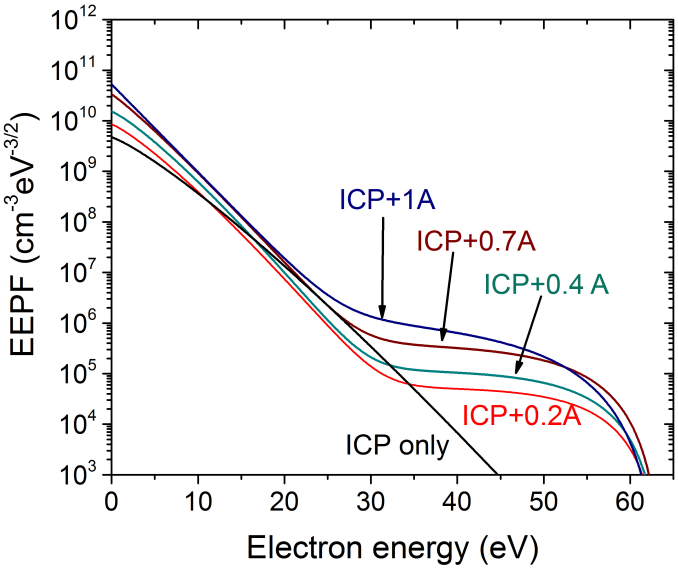

Figure 6.8: EEDFs represented by the sum of 'bulk' and 'tail' EEDFs for a 100 W Ar-containing ICP with electron injection (-50 V bias) as a function of electron injection current. The 'bulk' EEDFs are measured using the Langmuir probe method (see Table 5.2), and the 'enhanced EEDF tails' are determined from the OES method using Ar, Ne and He emissions.

tail increases with the electron injection current. The shape of the EEDF tail is expected to be insensitive to the electron injection current.

From the raw emission spectra, one can qualitatively understand the changes of the EEDF tail as a function of electron injection current. The Ne, He and Ar^+ emissions which all have high excitation threshold energies increase as the electron injection current increases, indicating an increase in concentration of energetic electrons (Fig. 6.7). On the other hand, the Ar neutral 419.83 nm line, which is excited mainly by electrons in the 'bulk' portion of the EEDF, is essentially independent of the electron injection current. As the electron injection current increases from 0 A (ICP only case) to 1 A (ICP plus injected electrons), the electron temperature (T_x) decreases while the electron density (n_e) increases (Table 5.2). The effects of these two changes in the 'bulk' EEDF have opposite effect on the excitation rate, so that the Ar neutral emission intensity changes little.

Input parameters used in the emission model analysis are listed in Table 5.2, with output parameters describing the 'tail' EEDF are listed in Table 6.1. Two parameters, the tail density (n_{tail}) and the shape parameter (s) were obtained from fitting the OES results while the third tail

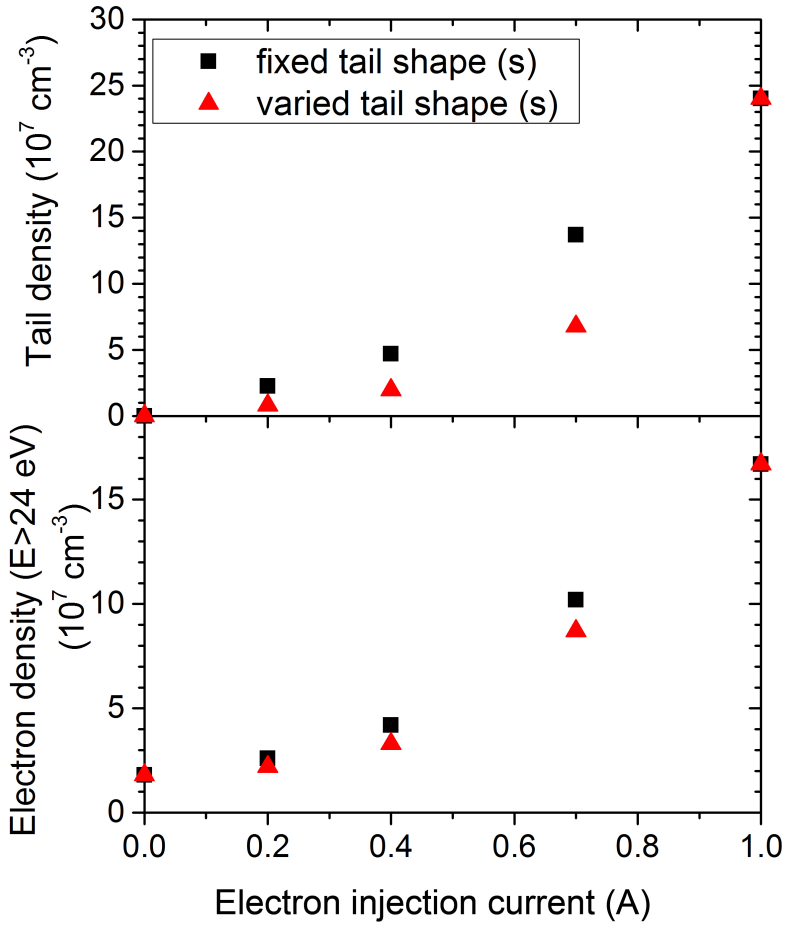

Figure 6.9: OES results for the Ar-containing ICP discharge as a function of electron injection current (a) tail density and (b) density of electrons with energies above 24 eV. Squares represent values obtained with a fixed shape parameter s, and triangles are obtained from the simultaneous measurements of n_{tail} and s.

Table 6.1: EEDF tail parameters based on a log-normal representation in the OES analysis for a 100 W Ar-containing ICP discharge (15 mTorr Ar, 15 mTorr He and 3 mTorr Ne) with electron injection (-50 V bias) as a function of electron injection current. The cutoff energy of the EEDF tail (E_{cut}) is estimated using Eq. 7.2 and the values in Table 5.2. Two sets of tail densities n_{tail} are determined: One allowing the shape parameter s to vary, and the other assuming a fixed value of s.

	Electron injection current (A)				
parameter	0 A	0.2 A	0.4 A	0.7 A	1 A
E_{cut} (estimated) (eV)	65	69	66	65	64
s allowed to vary					
n_{tail} (10^7 cm^{-3})	0	0.8	2	6.8	24
s	-1	3.3	3.5	3.7	4.4
s fixed at 4.4					
n_{tail} (10^7 cm^{-3})	0	2.3	4.7	13.7	24

parameter (E_{cut}) was fixed as an input to the analysis based on the power supply settings and the probe-measured plasma potential, which varied with energetic electron injection. In principle, an increase in the electron injection current would lead to an increase in the tail density (n_{tail}). This trend is well reflected in Fig. 6.8 showing the EEDF results as the sum of the 'bulk' (from the probe) and 'tail' EEDFs (from the OES method) versus electron injection current. The shape of the EEDF tail changes little as the electron injection current increases, which is also expected.

Since the shape of the EEDF tail is expected to be insensitive to the electron injection current, one can also fit n_{tail} using a fixed tail shape (s) which serves as a check for simultaneous determination of n_{tail} and s. For this test, s was fixed at 4.4 which corresponds to value obtained at 1 A electron injection current, where the uncertainties in the shape determination were smallest. Figure 6.9a shows the variation in the tail density versus electron injection current with both a fixed s and with s determined by the analysis. Both data sets increase with the electron injection current. Note that for $s \gtrsim 2.5$ a significant fraction of the 'tail' EEDF occurs at low energies normally considered to be part of the 'bulk' distribution. In these cases, n_{tail} is not exactly representative of the number of 'hot' electrons. Hence, another way to evaluate the OES results is to determine the density of electrons above a certain threshold energy. Figure 6.9b plots the population of 'hot' electrons for a threshold of 24 eV which is close to the excitation threshold of He emitting states. The 'hot' tail density results with a fixed s and with s determined by the OES analysis are in

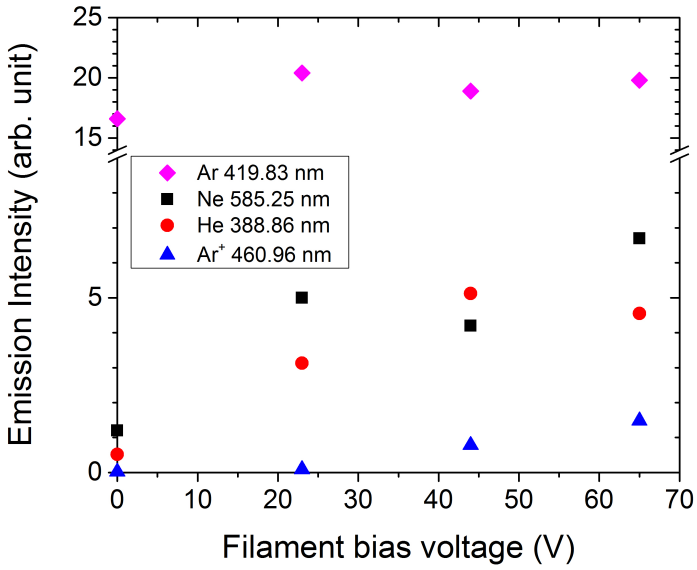

Figure 6.10: Variation of selected emission intensities with the filament bias voltage for a 100 W Ar-containing ICP discharge (15 mTorr Ar, 15 mTorr He and 3 mTorr Ne) with electron injection (1 A).

agreement, and they both increase with electron injection current, as expected.

6.3.2 Filament bias voltage

In the second experiment, the OES diagnostic is evaluated as a function of the filament bias voltage. The bias voltage on the filaments was varied between 0 and -50 V to control the injected electron energy for fixed ICP operating parameters (100 W, 15 mTorr Ar, 15 mTorr He and 3 mTorr Ne) and electron injection current (1 A). The maximum energy of the injected electrons is expected to increase as the filament bias voltage decreases. The electron velocity varies as the square root of the injected electron energy. Hence, despite the constant electron injection current, the density of injected electrons (proportional to the current divided by the velocity) decreases weakly with the bias voltage (due to the square root dependence of velocity on the injected electron energy).

The plasma parameters used in the emission model analysis for determining EEDF tails are listed in Table 6.2. For the log-normal EEDF tail distribution, two parameters, the tail density (n_{tail}) and the shape parameter (s) were obtained from fitting the OES results while the third tail parameter (E_{cut}) was estimated using Eq. 7.2 based on the power supply settings and probe-

measured plasma potential, which varied with energetic electron injection.

The Ne, He and Ar^+ emissions increase as the magnitude of filament bias voltage increases (Fig. 6.10), indicating an increase in concentration of electrons with energies above the excitation threshold energies of those emissions. Note that a larger bias voltage is required for an increase in the Ar^+ emissions (excitation threshold energy ~35 eV) than the Ne and He emissions (~19 eV and ~23 eV, respectively). On the other hand, the Ar neutral 419.83 nm line is mainly excited by the 'bulk' electrons such that the emission intensity of this line is insensitive to the filament bias voltage. Although the electron density increases by a factor of five from the ICP only case to the -50 V filament bias case, the emission intensity of this line changes little due to a compensating effect of a decrease in the electron temperature (see Table 6.2).

The EEDFs generated using the OES-derived tail parameters summed with the 'bulk' x-form EEDF obtained from the probe as a function of filament bias voltage are shown in Fig. 6.11. Note that the energies of injected electrons also strongly affects the 'bulk' EEDF. Increasing the injected electron energy leads to a decrease in the bulk electron temperature (T_x) and an increase in the electron density (n_e) (see Table 6.2). This trend has also been observed when characterizing the filament electron source in Chapter 4. Therefore, the electron temperature for the -10 V case seems to be an outlier.

Fig. 6.11 also illustrates variations in the EEDF tail with changes in the filament bias voltage. However, it is important to stress that the curves in Fig. 6.11 are calculated with a pre-set value for E_{cut} based on Eq. 7.2 that varies with the bias voltage. Hence, the maximum energy of the log-normal tail distribution is being set by the user and is not a free parameter extracted from the OES fitting, only n_{tail} and s are obtained from the fit. The extracted values of n_{tail} and s vary significantly with the bias voltage. Nevertheless, it is hard to interpret these raw numbers. For example, the tail density (n_{tail}) is much larger at -50 V bias than -10 V bias; but, due to the larger s value at -50 V than -10 V, many of the 'tail' electrons have a low electron energy. Even with a small s=2.3, which should provide a 'bump' near E_{cut}, the -10 V bias case exhibits no obvious tail component. At -10 V filament bias, the cutoff energy of the EEDF tail is estimated to be 25 eV. The x-form 'bulk' EEDF is orders of magnitude higher than the OES-derived log-normal EEDF tail at this energy range (0-25 eV). As a result, the 'final' EEDF result for -10 V filament bias case in Fig. 6.11 is dominated by the x-form EEDF and the EEDF tail cannot be observed.

Table 6.2: Measured emission model inputs and EEDF tail parameters based on a log-normal representation in the OES analysis for a 100 W Ar-containing ICP discharge (15 mTorr Ar, 15 mTorr He and 3 mTorr Ne) with electron injection (1 A) as a function of filament bias voltage. The cutoff energy of the EEDF tail (E_{cut}) is estimated using Eq. 7.2 and the values in Table 5.2. The tail densities n_{tail} and the shape parameter s are determined from the OES analysis.

	Filament bias voltage (V)			
parameter	0 V (ICP only)	-10 V	-30 V	-50 V
T_{gas} (K)	540	610	630	650
n_0 (Ar) (10^{13} cm^{-3})	21.5	19	18.6	18
n_0 (Ne) (10^{13} cm^{-3})	4.3	3.8	3.7	3.6
n_0 (He) (10^{13} cm^{-3})	21.5	19	18.6	18
OES-BF				
n_m (Ar) (10^8 cm^{-3})	503	328	290	360
n_r (Ar) (10^8 cm^{-3})	220	99	43	106
probe EEDF				
V_p (V)	18.6	7.8	8.5	8.7
n_e (10^{10} cm^{-3})	3.5	4.5	8.4	18.2
T_x (eV)	3.5	3.7	2.9	2.5
x	1.3	1	1.0	1.1
EEDF tail parameters (E_{cut} fixed)				
E_{cut} (eV) (fixed)	25	23	44	64
n_{tail} (10^7 cm^{-3})	0	1.1	3.6	24
s	0	2.3	3	4.4
EEDF tail parameters (s fixed)				
E_{cut} (eV)	10	30	62	64
n_{tail} (10^7 cm^{-3})	0	4	7	24
s (fixed)	4.4	4.4	4.4	4.4

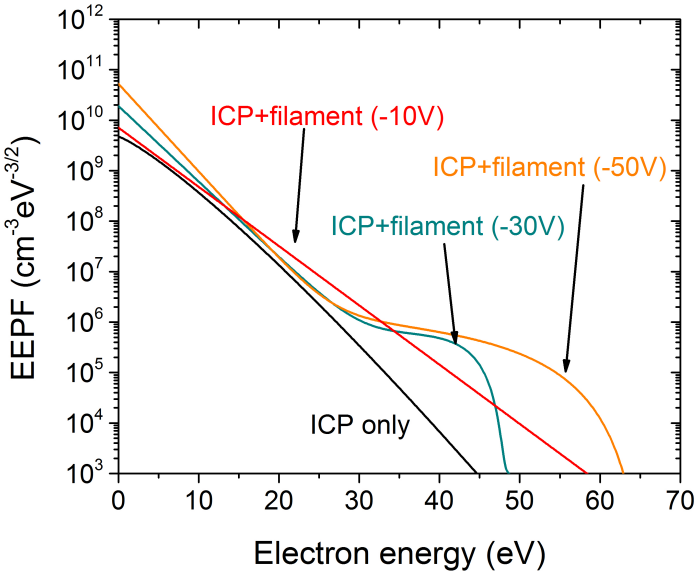

Figure 6.11: EEDFs represented by the sum of 'bulk' and 'tail' EEDFs for a 100 W Ar-containing ICP with electron injection (1 A) as a function of filament bias voltage (reversed sign). The 'bulk' EEDFs are obtained from the probe (see Table 6.2). The 'enhanced EEDF tails' are determined from the OES method. The tail density (n_{tail}) and the shape parameter (s) are determined by assuming fixed cutoff energies of the EEDF tail (E_{cut}).

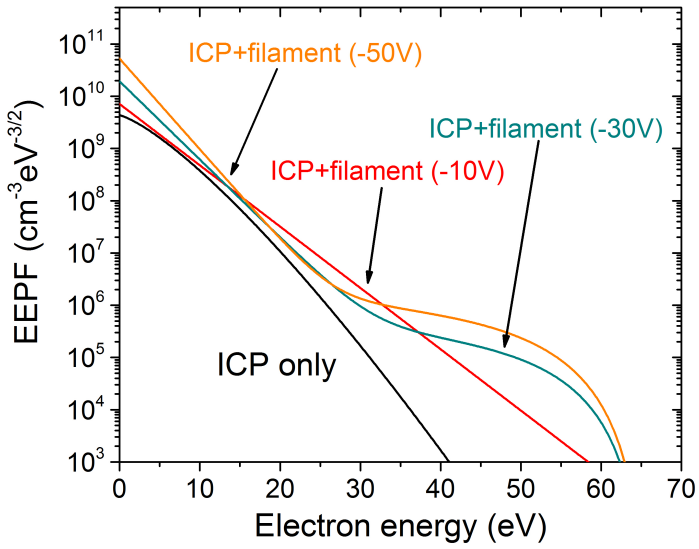

Figure 6.12: EEDFs results for the Ar-containing plasma with electron injection (1 A) as a function of filament bias voltage. The tail density (n_{tail}) and the cutoff energies of the EEDF tail (E_{cut}) are determined by assuming a fixed shape parameter (s).

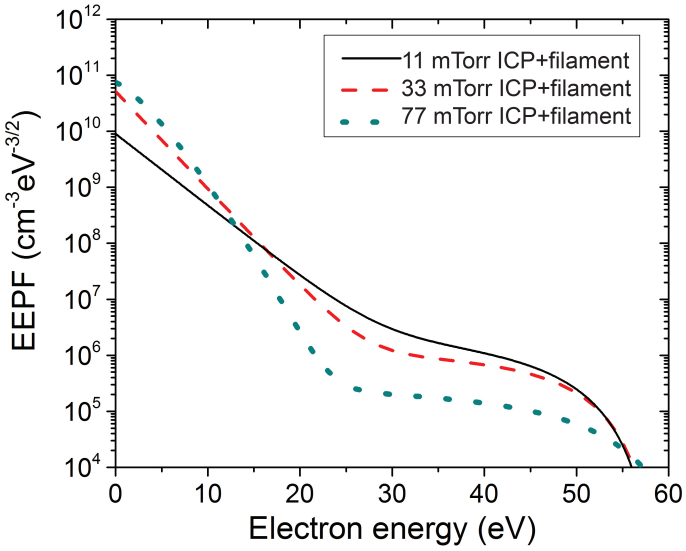

Figure 6.13: EEDFs for a 100 W Ar-containing plasma with electron injection (1 A, -50 V bias) as a function of source pressure. The x-form 'bulk' EEDF is obtained from Langmuir probe measurements. The tail density (n_{tail}) and the shape parameter s are determined from the OES method using fixed cutoff energies of EEDF tails (E_{cut}) estimated from Eq. 7.2.

In general, one may want the OES diagnostic to obtain E_{cut} from the fitting process rather than having this value pre-set. In the present experiment, the value of E_{cut} is essentially known via the user's control of the bias voltage. In other applications, however, this value may not be known. Due to the difficulties in extracting three parameters at the same time, if one wants to vary E_{cut}, either n_{tail} or s needs to be fixed. Fig. 6.12 illustrates an attempt to extract E_{cut} and n_{tail} while s was held fixed at 4.4 (the value measured at -50 V filament bias with a fixed E_{cut}). On one hand, the EEDF tails in Fig. 6.12 are similar to those in Fig. 6.11, with the maximum energy of the tails increasing with the filament bias voltage. While the trend of E_{cut} holds qualitatively, the quantitative results are less encouraging. For unknown reasons, similar E_{cut} values are found for both the -30 V and -50 V bias voltages (see Table 6.2). Additional future efforts will be required to determine the best way to extract values of E_{cut} using OES emissions.

Table 6.3: EEDF tail parameters based on a log-normal representation in the OES analysis for a 100 W Ar-containing ICP discharge with electron injection (1 A, -50 V) as a function of the total pressure (11, 33 and 77 mTorr) with a fixed gas admixture (45% Ar, 10% Ne and 45% He). The cutoff energy of the EEDF tail (E_{cut}) is estimated using Eq. 7.2. The tail densities n_{tail} and the shape parameter s are determined from the OES analysis.

	Total pressure		
parameter	11 mTorr	33 mTorr	77 mTorr
T_{gas} (K)	650	650	650
n_0 (Ar) (10^{13} cm^{-3})	6	18	54
n_0 (Ne) (10^{13} cm^{-3})	1.2	3.6	10.8
n_0 (He) (10^{13} cm^{-3})	6	18	54
OES-BF			
n_m (Ar) (10^8 cm^{-3})	240	360	360
n_r (Ar) (10^8 cm^{-3})	23	108	80
probe EEDF			
V_p (V)	10.2	8.7	7.9
n_e (10^{10} cm^{-3})	6.8	18.5	32
T_x (eV)	3.4	2.5	2.3
x	1	1.1	1.3
EEDF tail parameters			
E_{cut} (estimated) (eV)	66	64	65
n_{tail} (10^7 cm^{-3})	51	24	4.5
s	4.1	4.4	4.2

6.3.3 Source pressure

A third test of the diagnostic is found by having filament electrons (1 A, -50 V bias) injected into 100 W mixed-gas ICP plasmas at different total pressures (11, 33 and 77 mTorr) with a fixed gas admixture (45% Ar, 10% Ne and 45% He). The energy decay of the injected electrons due to inelastic collisions can be described using the energy relaxation length λ_{in}, the distance the electron propagates before losing a substantial portion of its energy [13],

$$\lambda_{in} = \sqrt{\frac{\lambda_m \lambda_{inel}}{3}}\,, \tag{6.5}$$

where λ_m is the mean free path for elastic momentum transfer of the electrons, and λ_{inel} is the mean free path length for inelastic collision process. λ_{in} varies inversely with the discharge pressure. When the pressure is low (11 mTorr), λ_{in} (20 cm) is larger than the distance from the filament electron source to the chamber wall ($\sim$14 cm), which indicates energetic electrons may pass through the main plasma and reach the chamber wall without colliding. When the pressure is high (77 mTorr), λ_{in} (3 cm) is smaller than the distance from the filament electron source to the discharge center ($\sim$6 cm), which means injected energetic electrons may lose most of their energy before reaching the OES line of sight. For the 33 mTorr case, λ_{in} (8 cm) is similar to the distance from the filament electron source to the discharge center ($\sim$6 cm). The electron density for the injected electrons varies with the effective confinement time. At low pressures this is simply the time to cross from the filaments to the far wall of the chamber. At higher pressures, electrons collide with atoms and is 'bounce' around within the plasma before escaping. Hence, the tail density is expected to initially increase with pressure before decreasing at very high pressures due to their loss of energy which makes 'tail' electrons indistinguishable from the bulk.

The plasma parameters used in the emission model analysis for determining EEDF tails are listed in Table 6.3. For the log-normal EEDF tail distribution, two parameters, the tail density (n_{tail}) and the shape parameter (s) were obtained from fitting the OES results while the third tail parameter (E_{cut}) was estimated as Eq. 7.2. EEDF results obtained as a function of pressure are listed in Table 6.3 and plotted in Fig. 6.13. The electron temperature (T_x) decreases and the electron density (n_e) increases as the source pressure is increased (see Table 6.3). The density of the EEDF tail (n_{tail}) decreases as the source pressure increases for the three tested cases. From

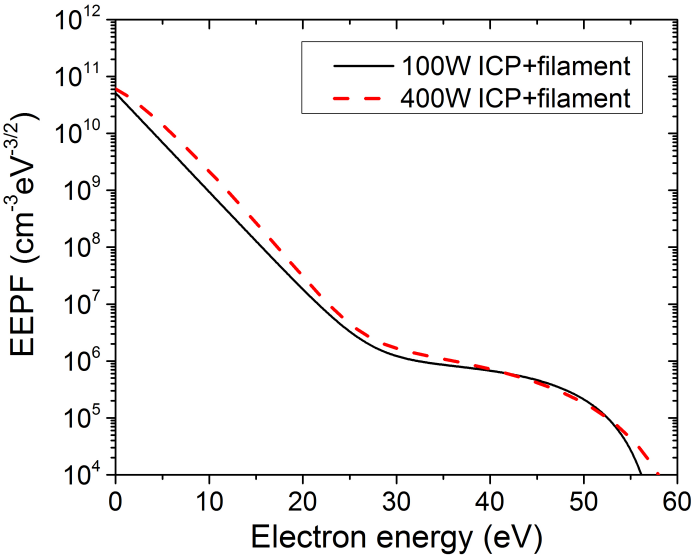

Figure 6.14: EEDFs for a 100 W Ar-containing ICP with electron injection (1 A, -50 V bias) as a function of discharge power. The tail density (n_{tail}) and the shape parameter s are determined using the OES diagnostic by using fixed cutoff energies of the EEDF tail (E_{cut}).

measurements at only three source pressures, it is hard to understand the dependence of the tail density on the source pressure. But the trend in tail density measured observed for the three source pressures matches the general expectation.

6.3.4 ICP discharge power

The fourth and final test of the diagnostic was obtained with filament electrons (1 A, -50 V bias) injected into the mixed-gas ICP plasma (15 mTorr Ar, 15 mTorr He and 3 mTorr Ne) at different ICP discharge powers (100 W and 400 W). The primary effect of increasing the ICP discharge power should be to increase the 'bulk' plasma density (n_e), with little change to the EEDF tail. Nevertheless, electron-electron collisions and instabilities may affect the 'cooling' of the injected energetic electrons, which depend on the 'bulk' electron density. Hence, small variations in the shape of the EEDF tail with the ICP discharge power can not be ruled out.

The plasma parameters used in the emission analysis, and the OES-derived EEDF tail parameters as a function of discharge power are listed in Table 6.4. From the EEDF results in Table 6.4, it is seen that the bulk electron density (n_e) does indeed increase as the discharge power increases.

Table 6.4: EEDF tail parameters based on a log-normal representation in the OES analysis for a Ar-containing ICP discharge (15 mTorr Ar, 15 mTorr He and 3 mTorr Ne) with electron injection (1 A, -50 V) as a function of ICP power (100 W and 400 W). The cutoff energy of the EEDF tail (E_{cut}) is estimated using Eq. 7.2. The tail densities n_{tail} and the shape parameter s are determined from the OES analysis.

	Discharge power	
parameter	100 W	400 W
T_{gas} (K)	650	730
n_0 (Ar) (10^{13} cm^{-3})	18	16
n_0 (Ne) (10^{13} cm^{-3})	3.6	3.2
n_0 (He) (10^{13} cm^{-3})	18	16
OES-BF		
n_m (Ar) (10^8 cm^{-3})	360	500
n_r (Ar) (10^8 cm^{-3})	80	170
probe EEDF		
V_p (V)	8.7	11
n_e (10^{10} cm^{-3})	18.5	30
T_x (eV)	2.5	2.8
x	1.1	1.2
EEDF tail parameters		
E_{cut} (estimated) (eV)	64	66
n_{tail} (10^7 cm^{-3})	24	31
s	4.4	4.7

The EEDF tails at these two ICP power levels, however, are about the same. The change in the 'bulk' n_e with ICP power may not be enough to seriously affect the EEDF tail distribution.

6.4 Conclusion

Compared to only using Ar and Ar^+ emissions (Chapter 5) adding Ne and He emission lines improves the ability of the OES diagnostic to measure non-Maxwellian EEDFs with enhanced tails. For example, both the density and shape of the tail component could be measured simultaneously in experiments made with injected electrons. Tail components were quantitatively measured in a wide variety of plasma systems as a number of control parameters were varied, i.e., pressure (11, 33 and 77 mTorr), power (100 and 400 W), filament bias voltage (0-50 V), emission current (0-1 A). Qualitatively, the trends of the results were about what one might expect, i.e., the tail component increase with the injected current. A quantitative test of the method, however, is hampered by the inability to perform independent (non-OES) measurements of the tail component with a Langmuir probe owing to the low sensitivity of probes in the high energy range where the tail is most evident.

A number of limitations were found. First, the log-normal distribution used to describe the tail-component of the EEDF uses three parameters E_{cut}, n_{tail} and s, but only the n_{tail} and s values were generally obtained in the OES fitting. While this was not much of a limitation in the present experiment where E_{cut} could be determined from the control parameter settings, a robust method for extracting all three parameters will be required for a full diagnostic.

A second limitation is the use of Ar/Ne/He gas mixture. In general, adding more gases to the plasma increases the complexity of the gas handling system and increases the number of gas-phase reactions possible in the plasma. Once again, this was not a true limitation in the present experiment since the system was capable of 3 gas mixtures and arbitrarily large amounts of Ne and He could be added to the Ar plasma without effecting the plasma conditions all that much. In this context, the 5:1:5 Ar:Ne:He mixture used in this work is somewhat arbitrary. A different gas mixture may be more beneficial for other plasma systems particularly when the trace-gases are added as a tracer to a more reactive gas.

A third limitation of the method presented in this chapter is that the 'bulk' EEDF description was based on Langmuir probe measurements. As such, the method is not non-invasive, and requires

two separate types of equipment and analysis. Overcoming this limitation with an all-optical OES diagnostic is the topic of the next chapter.

Chapter 7

Full OES diagnostic of 'bulk+tail' EEDFs

The OES results obtained in the last two chapters did not use an all-optical method. As illustrated in Fig. 7.1a, the parameters describing the 'bulk' component of the EEDF (T_x, x, n_e) were obtained from Langmuir probe measurements. The OES diagnostic was only used to determine parameters describing the EEDF tail. Using a combination of probe and OES methods is not fully non-invasive. To remove the need for the probe, an optical diagnostic is sought to measure the 'bulk' EEDF parameters that have previously been measured by the probe.

In this chapter, we implement an all-OES diagnostic for non-Maxwellian "enhanced tail" EEDFs which are represented by the sum of 'bulk' and 'tail' EEDFs. As described previously, there are too many free parameters in the 'bulk+tail' EEDF representation to be uniquely determined in a single OES fitting operation. Instead, a two stage process is used. The general process is illustrated in Fig. 7.1b. In the first stage, the 'bulk' EEDF using the x-form representation (T_x, x and n_e) is determined from the analysis of selected Ar emissions. This step is essentially the same as that used previously to characterize Maxwellian (and near-Maxwellian) EEDFs [76, 59]. In the second stage of fitting, a log-normal representation for the 'tail' EEDF (n_{tail}, E_{cut} and s) is obtained from an analysis of Ar, Ne He and Ar^+ emission lines as described in Chapter 6. Note that when measuring the 'bulk' parameters in Stage I, contributions from the 'tail' distribution are neglected, as they are unknown at that time. If the 'tail' contribution to exciting emitting states

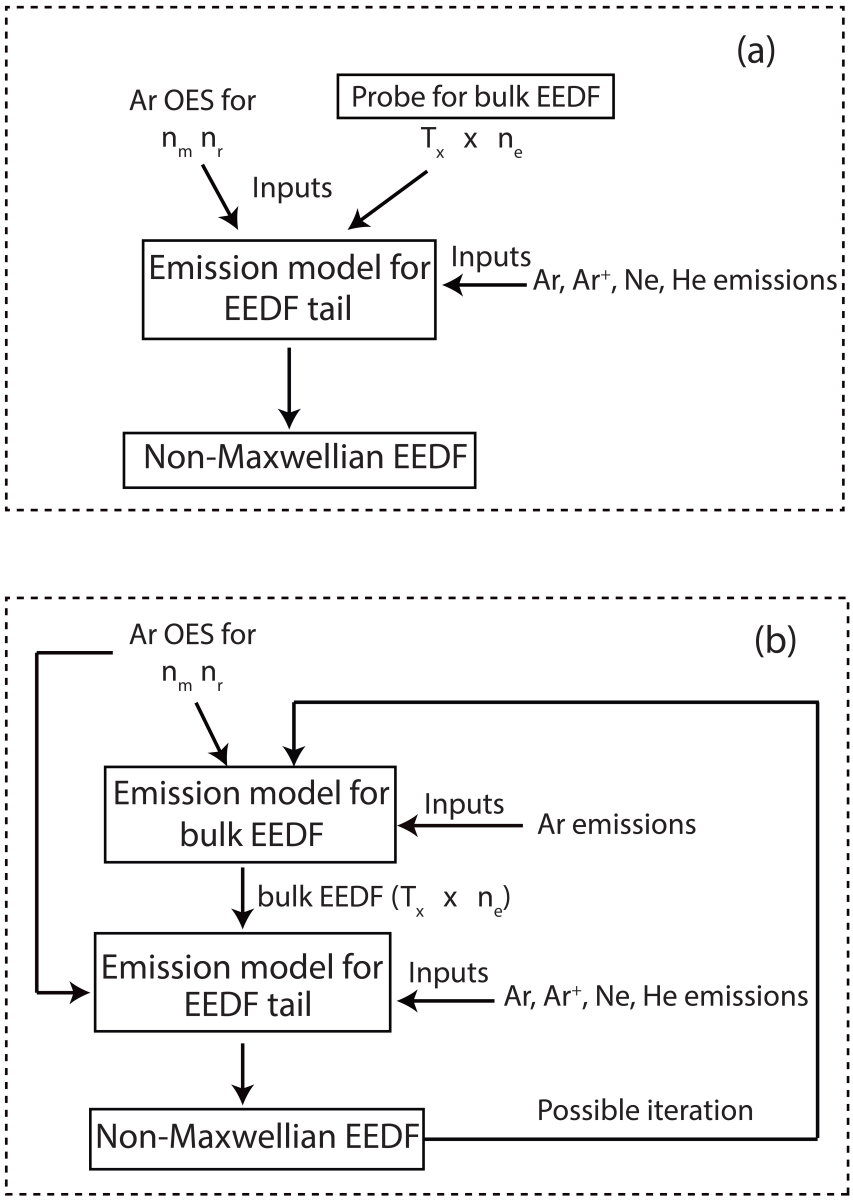

Figure 7.1: Flow chart for determining non-Maxwellian EEDFs represented as the sum of 'bulk' + 'tail' EEDFs using (a) the OES/probe method (probe for 'bulk EEDFs and OES method for 'tail EEDFs, respectively) and (b) the all OES method.

is significant, however, their omission may distort the extracted 'bulk' parameters. For example, the electron temperature (T_x) may be overestimated. In principle, an iterative approach can be applied to solve this problem (as illustrated in Fig. 7.1b). Specifically, in the first iteration, the 'bulk' EEDF is obtained while neglecting any possible tail contribution. These bulk parameters are

used to obtain a set of tail parameters. In the second iteration, we re-conduct the emission analysis for the 'bulk' EEDF including the contributions to emission intensities from the 'tail' electrons. This can be used to obtain a revised tail fit, and the process repeated until the results converge. Nevertheless, this iterative approach is not needed for the sample measurements of 'bulk' EEDFs presented here. The disturbance from EEDF tails to the OES-derived 'bulk' EEDFs is minimized by selecting Ar emission lines with low excitation threshold energies and therefore dominated by the contributions from 'bulk' electrons in the emission analysis. The accuracy of the all-OES diagnostic of non-Maxwellian EEDFs is evaluated by comparing results with those obtained from the combined OES/probe method employed in the previous chapter.

7.1 OES diagnostic for 'bulk' EEDFs

Development of an all-OES diagnostic of non-Maxwellian EEDFs involves adapting the OES analysis (described in Chapter 2) to the 'bulk' and 'tail' EEDF separately. A flow chart of the analysis showing the general procedure and wavelengths employed is shown in Fig. 7.2. Both Ar 2p and 3p emissions with small excitation threshold energies compared with Ne, He and Ar^+ emissions are used in the emission analysis to determine the 'bulk' EEDF [59, 74]. The same set of Ar, Ne and He emission lines are used here for determining EEDF tails as described in Chapter 6.

The first step in the two stage fitting process is to estimate the 'bulk' EEDF x-form parameters. Using the emission analysis to determine 'bulk' EEDFs is discussed in detail in Chapter 2. OES measurements of 'bulk' EEDFs conducted in the modified ICP source as a function of electron injection current are presented and compared with Langmuir probe measurements.

7.1.1 Determining T_x and x using the OES diagnostic

The extended corona model predicts relative intensities of Ar emissions by combining an assumed EEDF (T_x, x) with known excitation cross sections [56, 57, 60, 58, 130] and the number densities of lower levels, including the ground state (n_{gs}) and metastable levels (n_m, n_r), as captured in Eqs. 2.1 and 2.2. The ground state density is estimated from the gas pressure and temperature [59] and the metastable and resonance densities are determined from the emission spectra, based on the degree of radiation trapping, as discussed in Section 2.3.2. With these values as model inputs,

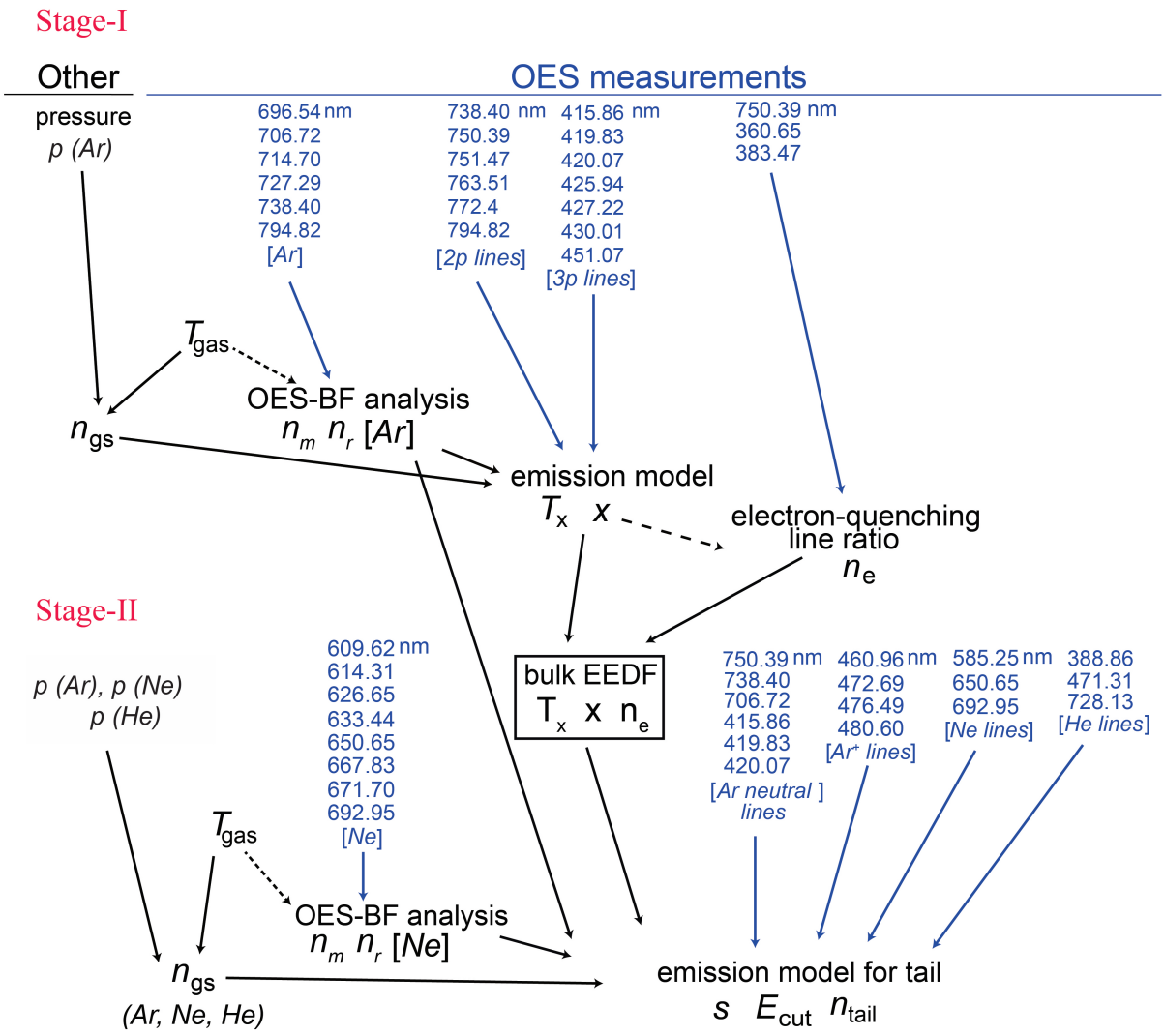

Figure 7.2: Flow chart of OES analysis for both the 'bulk' EEDF (T_x, x, n_e) and the 'tail' EEDF (s, n_{tail}, E_{cut}) using Ar, Ne and He emission lines.

x and T_x values are determined as those which minimize the difference (χ^2) between predicted and measured spectra. In order to minimize the disturbance from the EEDF tail to the determination of the 'bulk' EEDF, only the Ar neutral emissions are used in the emission analysis (Fig. 7.2). The selected argon neutral emission lines have small excitation threshold energies compared with Ne, He and Ar^+ emissions, and therefore their excitation is dominated by electrons from the 'bulk' EEDF.

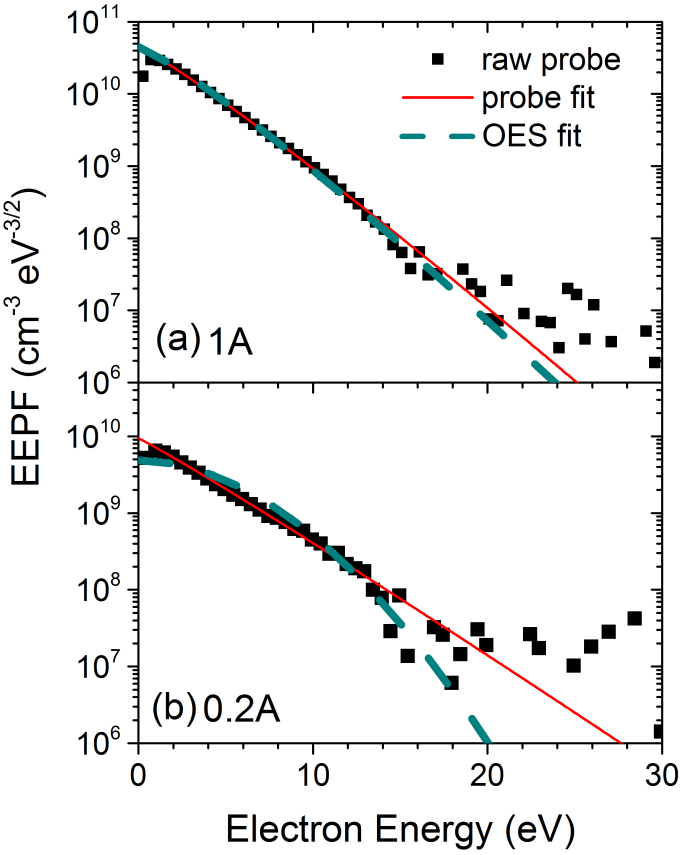

Figure 7.3: Comparison of 'bulk' EEDF results obtained from Langmuir probe measurements (squares), a fit of probe values to 'x-form' (solid line) and OES method (dashed line) for 100 W Ar- containing ICP discharge (15 mTorr Ar, 15 mTorr He and 3 mTorr Ne) with (a) 1 A and (b) 0.2 A electron injection (-50 V bias).

7.1.2 Sample OES measurements of T_x and x

The OES diagnostic for T_x and x was evaluated by measuring a 100 W ICP discharge (15 mTorr Ar, 15 mTorr He and 3 mTorr Ne) as a function of electron injection current (0, 0.2, 0.4, 0.7 and 1 A). Langmuir probe measurements were also conducted to provide a comparison to the OES results to assess the accuracy of the OES method. Also, a χ^2 sensitivity analysis was conducted for the T_x and x derived by both probe and OES methods. In this section, measurements of 0.2 A (with a small EEDF tail) and 1 A electron injection current (with a large EEDF tail) cases are presented as sample of these results.

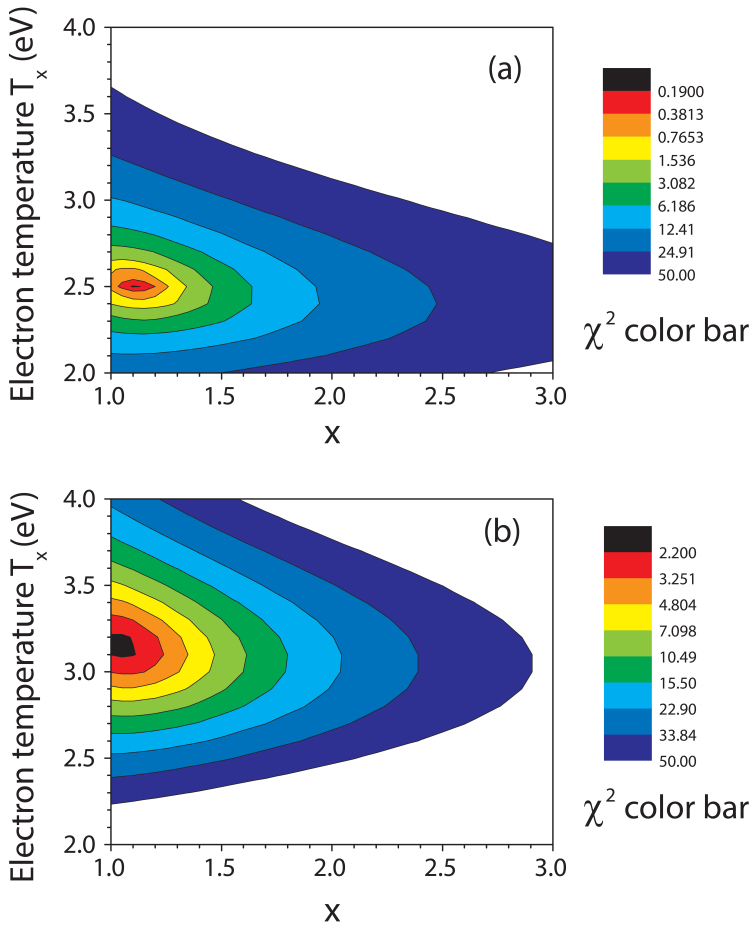

Figure 7.4: Values of reduced χ^2 resulting from a comparison of the x-form representation of the EEDF to measured probe data for a 100 W Ar-containing plasma (15 mTorr Ar, 15 mTorr He and 3 mTorr Ne) with (a) 1 A and (b) 0.2 A electron injection (-50 V). Lower values of χ^2 indicate a better quality fit.

Langmuir probe measurements and OES-derived EEDFs for the 1 A and 0.2 A electron injection current in a 100 W ICP discharge (15 mTorr Ar, 15 mTorr He and 3 mTorr Ne) are shown in Fig. 7.3. In this analysis, the 'bulk' EEDF measured by both the probe and OES methods are characterized using T_x and x of the x-form representation. The x-form was fitted to the probe values over 0-20 eV energy range to determine T_x and x values as described in Sec. 4.3.1. The probe fit yields T_x=2.5 eV, x=1.1 for 1 A electron injection current case and T_x=3.15 eV, x=1.05 for 0.2 A electron injection current case. The OES measurements yield T_x=2.4 eV, x=1.15 for the 1 A electron injection current case and T_x=3.3 eV, x=1.9 for the 0.2 A case, respectively. Agreement is observed between

the probe and OES result for the 1 A case (Fig. 7.3a). For the 0.2 A case, the extracted T_x and x parameters show a larger difference between probe and OES approaches (Fig. 7.3b). However, the significant differences between the two curves at higher electron energies (E$\gtrsim$13 eV) is in some sense irrelevant as this energy range will be described by the 'tail' component of the combined EEDF in the second stage of the fitting process.

A χ^2 sensitivity analysis was conducted for EEDFs results for the 1 A and 0.2 A electron injection current cases obtained from both probe and OES methods. The sensitivity of the probe-derived T_x and x can be seen by examining Figure 7.4 showing the χ^2 difference between the raw probe measurements and x-form fit in the 0 to 20 eV range. As can be seen in Fig. 7.4, for both cases, there is a well defined minimum in the χ^2 surface, so the extracted values of T_x and x are well localized at 2.5$\pm$0.01 eV (within 10% of the minimum χ^2 value) and 1.1$\pm$0.02 for the 1 A electron injection case and 3.15$\pm$0.05 eV and 1.05$\pm$0.05 for the 0.2 A case. The sensitivity of the OES-derived T_x and x can also be seen by examining Figure 7.5 plotting the χ^2 difference between the model and experimental line ratios as a function of T_x and x used in the model calculation for the two filament emission cases. As illustrated in Fig. 7.5a, for the 1 A electron injection current data, the OES results are reasonably well localized at T_x=2.4$\pm$0.05 eV (within 10% of the minimum χ^2 value) and x=1.15$\pm$0.05, respectively. However, for the 0.2 A electron injection current, the extracted values of T_x=3.3$\pm$0.15 eV and x=1.9$\pm$0.3 are less well located.

T_x and x values obtained from both probe and OES methods for a 100 W Ar-containing ICP as a function of electron injection current are plotted in Fig. 7.6. The probe and OES results generally agree well. The largest difference is obtained for the 0.2 A filament case described in the preceding paragraph.

7.1.3 Determining n_e using the OES diagnostic

Absolute values for the electron density (n_e) are obtained by taking the line ratio of two emission lines from excited levels with significantly different radiative lifetimes (as described in Sec. 2.3.3). In the present analysis, we use emissions from the $4p_5$ level (360.65 and 383.47 nm) for the long-lived level (170 ns) and the emissions from the $2p_1$ level as the short-lived level (20 ns) (Fig. 7.2) [61]. Following the approach of Ref. [95], the electron density is obtained from

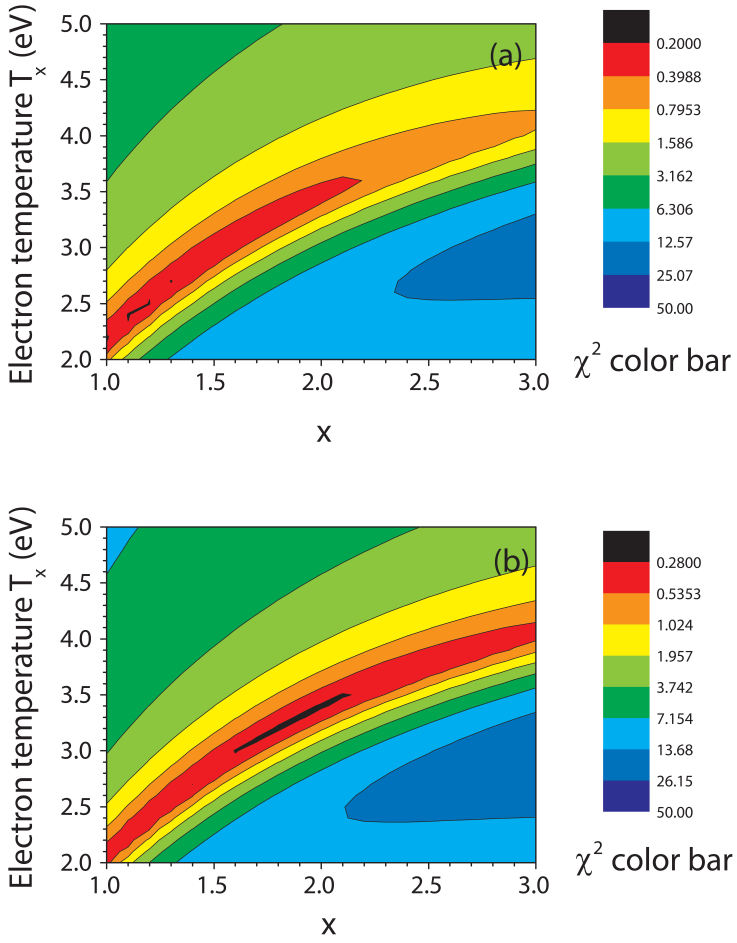

Figure 7.5: OES-derived values of χ^2 for a 100 W Ar-containing plasma (15 mTorr Ar, 15 mTorr He and 3 mTorr Ne) with (a) 1 A and (b) 0.2 A electron injection current (-50 V bias). Lower values of χ^2 indicate a better quality fit.

$$n_e = \frac{1 - \frac{I_1/I_2}{k_1/k_2}}{\left[\frac{I_1/I_2}{(k_1/k_2)\, n_{ec1}} - \frac{1}{n_{ec2}}\right]} \,, \tag{7.1}$$

where a subscript-1 refers to the $2p_1$ level and subscript-2 refers to the $4p_5$ level, I is the relative plasma photon emission rate, k is the ground state optical emission excitation rate, and n_{ec} is the 'critical' electron density (at which the electron collision loss rate equals the radiative decay rate) for each of the levels. Based upon the cross sections from Ref. [56], this dependence is estimated as $k_1/k_2 \approx (384 - 107\,T_e + 11\,T_e^2)$. The two critical electron densities are $n_{ec1} \approx 300 \times 10^{10}$ cm^{-3} and $n_{ec2} = 9 \times 10^{10}$ cm^{-3} [117]. Note that this method assumes both the $2p_1$ and $4p_5$ levels are being

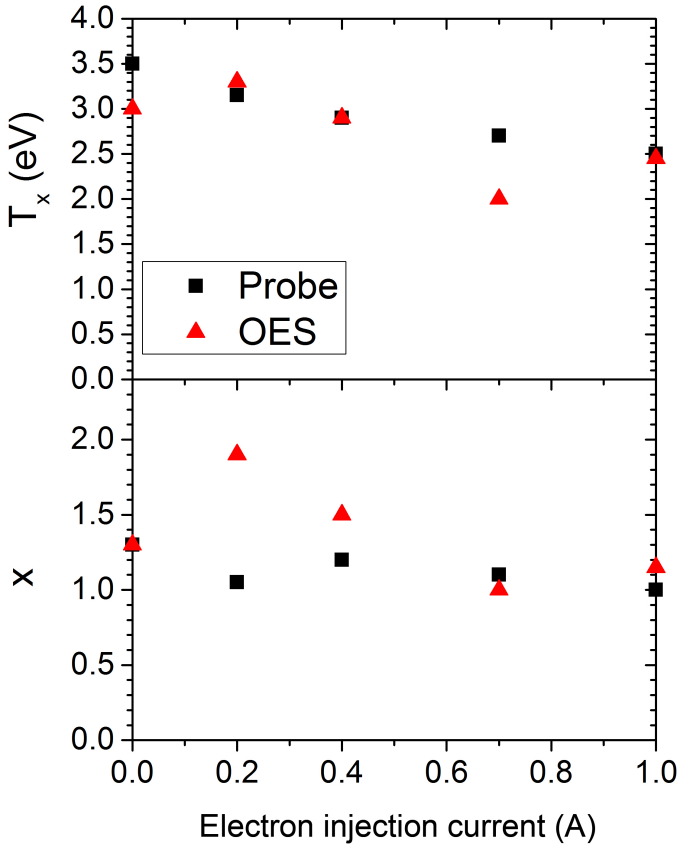

Figure 7.6: Comparison of (a) electron temperature (T_x) and EEDF shape parameter (x) values obtained from the probe and OES methods in 100 W Ar-containing plasma (15 mTorr Ar, 15 mTorr He and 3 mTorr Ne) with electron injection (-50 V) as a function of electron injection current. Squares are OES results, and triangles are probe values.

populated primarily by excitation of ground state atoms by the 'bulk' component of the EEDF.

7.1.4 Sample OES measurements of n_e

OES and Langmuir probe measurements of n_e were conducted for a 100 W Ar-containing ICP discharge (15 mTorr Ar, 15 mTorr He and 3 mTorr Ne) with electron injection (-50 V bias) as a function of electron injection current (0, 0.2, 0.4, 0.7 and 1 A). The accuracy of the OES method is evaluated by comparing with Langmuir probe results. The results are plotted in Fig. 7.7. As discussed in Sec. 4.3.1, an increase in the electron injection current leads to an increase in the

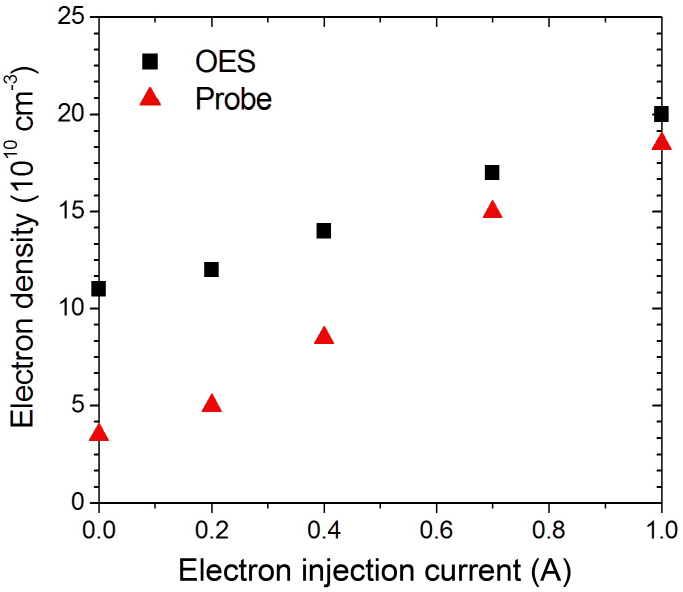

Figure 7.7: Comparison of electron density values obtained from the probe and OES method in 100 W Ar-containing plasma (15 mTorr Ar, 15 mTorr He and 3 mTorr Ne) with electron injection (-50 V) as a function of electron injection current. Squares are OES results, and triangles are probe values.

electron density (n_e). This general trend is well reflected in both the OES and probe results (Fig. 7.7), although the absolute values of the OES results are not in agreement with the probe results. This may be the result of two different things. First , the electron quenching method is generally more accurate at higher electron densities [76]. Second, the method only includes excitation by the 'bulk' component of the EEDF. In addition to being long-lived, the $4p_5$ level is also a high lying level which can be excited by electrons with E>15.06 eV. By neglecting the 'tail' component, the predicted emissions from this level may be underestimated, thereby the electron density with the OES method may be overestimated.

7.2 Full OES diagnostic of EEDF tails

In the second stage of the analysis (Fig. 7.2), the EEDF tail parameters are extracted from the OES analysis using the 'bulk' EEDF obtained in Stage I. All-OES EEDF measurements for a 100 W Ar-containing plasma (15 mTorr Ar, 15 mTorr He and 3 mTorr Ne) with electron injection (-50 V

filament bias) were conducted as a function of electron injection current. To evaluate the accuracy of this all-OES diagnostic, its EEDF tail results are compared with those obtained using 'bulk' EEDFs (T_x, x and n_e) obtained from Langmuir probe measurements (Sec. 6.3). In addition, EEDF measurements using another OES/probe (n_e) method in which n_e was obtained from probe, T_x, x and the EEDF 'tail' parameters were obtained from the OES method, were also conducted as a comparison to the all-OES and OES/probe results.

The OES/probe (n_e) measurements of EEDFs were conducted because the absolute value of n_e obtained from the OES method are not in good agreement with the probe results (Fig. 7.7). The electron density influences the 'end result' EEDF in three ways. First, n_e sets the overall magnitude of the EEDF. Second, n_e used in the analysis can affect the modeling of emission intensities via the inclusion of electron-quenching. Third, n_e is used as a proxy for the Ar^+ density which may be required to analyze Ar^+ emission lines. Comparing the OES/probe (n_e) results with the all-OES results, the effect of the OES n_e measurements on the 'end result' EEDF can be evaluated. It should also be noted that the electron density can also be measured non-invasively without relying on a Langmuir probe using microwave interferometry [13].

For the log-normal representation of EEDF tails in the OES analysis, the tail cutoff energy (E_{cut}) was held fixed, and the tail density (n_{tail}) and the shape parameter (s) were determined by the analysis. Three sets of 'bulk' EEDF parameters are used in the emission analysis: (1) probe for T_x, x n_e, (2) probe for n_e, OES for T_x, x and (3) all-OES for T_x, x, n_e. The 'bulk' EEDF results and the fitted EEDF tail parameters are both listed in Table 7.1. The EEDF results represented as the sum of 'bulk' and 'tail' EEDFs are presented in Fig. 7.8. Note that the cutoff energies (E_{cut}), used in the various cases have been determined as

$$E_{\text{inj}} = E_{\text{cut}} = e(V_p - V_{\text{bias}} - 1/2\ V_{\text{filament}})\ , \tag{7.2}$$

where V_{bias}=-50 V is the bias voltage applied to the filaments, $V_{\text{filament}}\simeq$-10 V is the voltage drop across the filaments and $eV_{\text{plasma}}\simeq$9-19 eV is the energy gained by electrons accelerating in the plasma. This V_{plasma} was obtained from Langmuir probe measurements. For a truly all-optical measurement, V_{plasma} can be estimated based on the 'bulk' electron temperature, $eV_p\simeq 4.7\times T_e$ for argon [13]. Despite differences in intermediate quantities, generally the combined 'bulk+tail'

Table 7.1: Emission model input parameters and EEDF tail parameters from fitting to the log-normal representation for 100 W Ar-containing plasma (15 mTorr Ar, 15 mTorr He and 3 mTorr Ne) with electron injection (-50 V bias) as a function of electron injection current (0-1 A). 'Bulk' EEDF parameters (T_x, x, n_e) are obtained from different methods, including the Langmuir probe, OES method and the combination of them (i.e., the probe for n_e and the OES method for T_x and x, respectively). $E_{\rm cut}$ is estimated from Eq. 7.2 (see Table 5.2). Tail density $n_{\rm tail}$ and tail shape parameter s are determined from the emission analysis.

	Electron injection current (A)				
parameter	0	0.2	0.4	0.7	1
Probe (bulk)+OES (tail)					
T_x (eV) [probe]	3.5	3.15	2.9	2.7	2.5
x [probe]	1.25	1.05	1.2	1.1	1.1
n_e (10^{10} cm^{-3}) [probe]	3.5	5	8.5	15.1	18.2
$E_{\rm cut}$ (eV) [fixed]	60	69	66	65	64
s [OES]	-1	3.3	3.5	3.7	4.4
$n_{\rm tail}$ (10^7 cm^{-3}) [OES]	0	0.8	4.7	13.7	24
Probe (n_e)+OES (bulk and tail)					
T_x (eV) [OES]	3	3.3	2.9	2.1	2.45
x [OES]	1.2	1.9	1.5	1	1.15
n_e (10^{10} cm^{-3}) [probe]	3.5	5	8.5	15.1	18.2
$E_{\rm cut}$ (eV) [fixed]	60	69	66	65	64
s [OES]	6.1	4.3	4.1	4	4.6
$n_{\rm tail}$ (10^7 cm^{-3}) [OES]	0.01	1.5	2.4	3.9	21
All OES method					
T_x (eV) [OES]	3	3.3	2.9	2.1	2.45
x [OES]	1.2	1.9	1.5	1	1.15
n_e (10^{10} cm^{-3}) [OES]	11.5	13.7	15.6	17.7	21
$E_{\rm cut}$ (eV) [fixed]	60	69	66	65	64
s [OES]	6.1	4.3	4.1	4	4.6
$n_{\rm tail}$ (10^7 cm^{-3}) [OES]	0.003	4.1	4.4	4.6	24

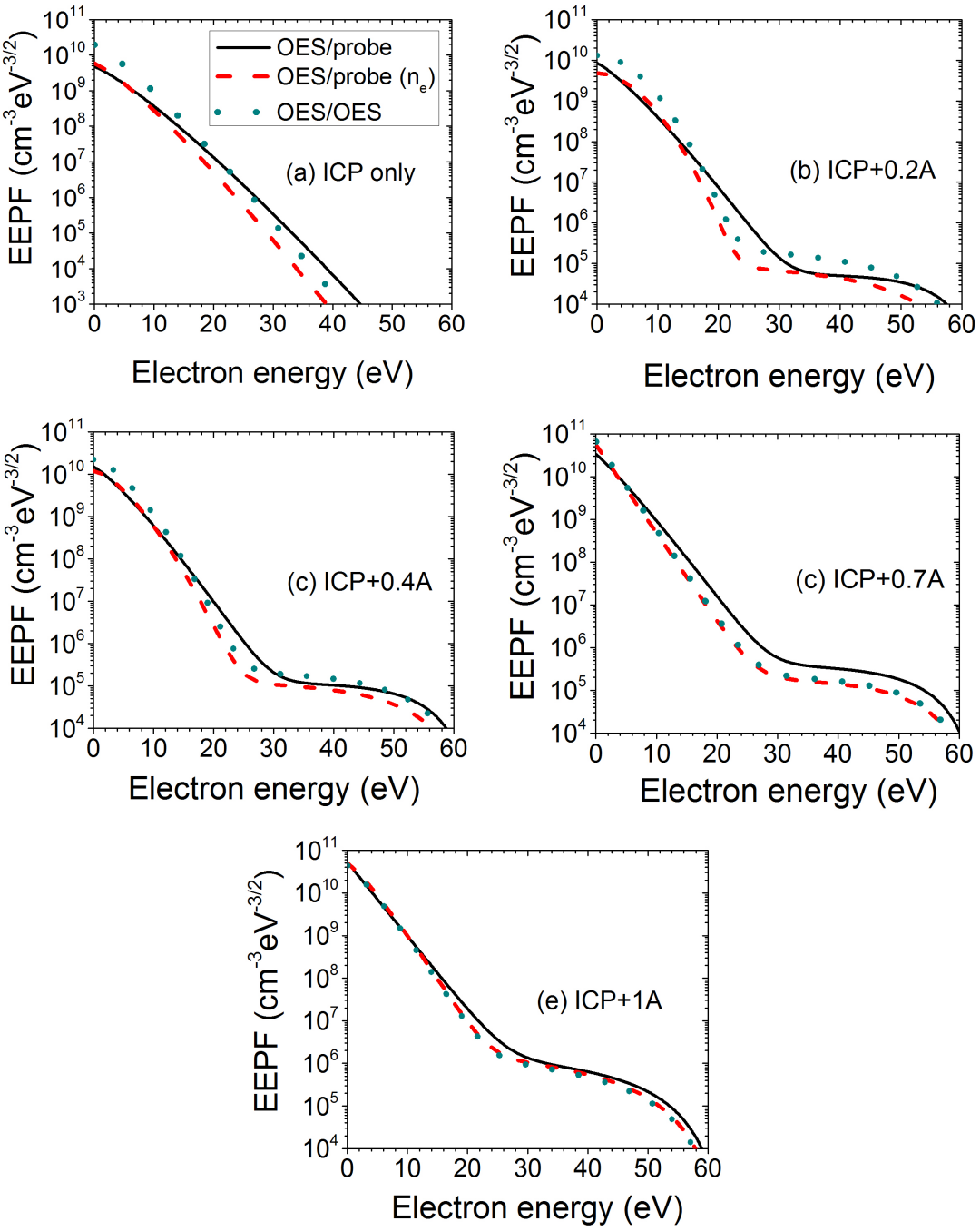

Figure 7.8: EEDFs for 100 W Ar-containing plasma (15 mTorr Ar, 15 mTorr He and 3 mTorr Ne) with electron injection (-50 V bias) as a function of electron injection current (0-1 A). Solid lines are results using 'bulk' EEDFs from Langmuir probe measurements. Dashed lines are results using T_x and x from the OES and n_e from the probe. Dotted lines are results of the all-OES method.

EEDFs obtained with three different sets of 'bulk' parameters are similar and reflect changes with injection current consistent with expected trends. Indeed, the largest differences are generally due to the differences in electron densities. As the electron injection current is increased, n_{tail} is expected to increase. This general trend is well reflected in results from all three different methods (see Table 7.1). As discussed in Chapter 6, the sensitivity of the OES/probe results for the two extreme electron injection current cases in which non-zero EEDF tails were measured, is n_{tail}=24±3.6×10^7 cm^{-3}, s=4.4±0.15 for 1 A electron injection current case and n_{tail}=0.8±0.33×10^7 cm^{-3}, s=3.3±0.5 for 0.2 A electron injection current case. A similar sensitivity was observed in the all-OES results: n_{tail}=24±4×10^7 cm^{-3}, s=4.6±0.2 for 1 A electron injection current case and n_{tail}=4.1±2.1×10^7 cm^{-3}, s=4.3±0.55 for 0.2 A electron injection current case.

7.3 Conclusion

The sample results presented in this chapter illustrate that an all-OES diagnostic for non-Maxwellian EEDFs is possible. Although there are differences in the 'bulk' EEDFs obtained from the probe and OES methods, the EEDF tails are not so sensitive to these differences. The non-Maxwellian EEDFs determined using the all-OES method is similar to those extracted using the combination of the probe and OES method. This all-OES diagnostic may potentially be applied to plasma process tools as a robust, non-invasive and easy-to-use diagnostic for non-Maxwellian EEDFs in low-temperature plasmas. One way to possibly improve the accuracy of all-OES EEDF results is the iterative approach (Fig. 7.1b). Due to the lack of time, this iterative approach has not been investigated in the present experiment, and may be studied in the future.

Chapter 8

OES diagnostics with a low resolution spectrometer

The OES results obtained in the last three chapters have employed a 'high resolution' 0.5 m monochromator with 0.14 nm resolution. This system is suitable for laboratory work, but the OES diagnostic would be far easier to implement widely if it could use a 'low resolution' spectrometer with a resolution around 1 nm. Fiber-coupled, USB spectrometers are relatively inexpensive and easy to use. Many plasma process tools used in IC manufacturing are equipped with low-resolution spectrometer to measure emission spectra for monitoring and control of plasma processes, such as endpoint detection [137, 138, 139] and monitoring plasma impurities.

The primary difficulty introduced by using a low-resolution spectrometer is suitably resolving the numerous peaks used in the analysis. Over thirty emission line were used in the all-optical OES method of the last chapter. Many of these peaks are within 0.5 nm of other Ar (or Ne or He) lines. These contaminated lines must either be eliminated from the fitting process, or only the summed contribution from both lines are used. Unless both lines are populated by similar energy electrons, the energy sensitivity is partially washed-out by using the blended lines. In either case, the effective number and quality of the lines available for the fitting process is reduced, lowering the power of the OES diagnostic.

In this chapter, a low-resolution spectrometer is used to measure Maxwellian-like and highly non-Maxwellian EEDFs. Three levels of analysis are explored. In the first, most basic approach,

a Maxwellian (or near-Maxwellian) EEDF is assumed and only a single EEDF parameter, the electron temperature (T_{eff}) is determined [140]. While not as sophisticated as the methods of the last few chapters, these electron temperature measurements can be obtained very rapidly ($\leq$0.1 s), allowing real-time, non-invasive measurement of the EEDF, which in combination with an accurate simulation would provide a feedback loop that would enable tuning of the EEDF to optimize process results. The second, slightly more sophisticated approach attempts to extract two EEDF parameters (T_x, x) used to characterize non-Maxwellian EEDFs. This method is attempted in a pure Ar ICP system which generally has EEDFs with a depleted tail. In the third approach, the low-resolution spectrometer is used to measure the high-energy tail component of a plasma with injected high-energy electrons.

8.1 Real-time OES measurements of electron temperature

Introduction

The non-invasive nature of optical diagnostics makes them an attractive option for monitoring and real-time control of plasma processes. For example, real-time end point detection is routinely used to determine the stopping point for plasma etch processes in the microelectronics fabrication industry by detecting changes in intensity in optical emissions of key gas-phase chemical species [141]. As the semiconductor industry progresses toward processes with both tighter electronic device tolerances and multiple steps within a plasma process, it is increasingly desirable to monitor the plasma state throughout the process. Electron temperature and density are relevant parameters for characterization of the dynamic behavior of processing plasmas, because gas phase reactions critical to process outcomes are driven by collisions involving energetic plasma electrons. In addition, because metastable and resonance level atoms release energy through de-excitation when they reach the substrate surface, their concentrations are sometimes relevant as well. Also, the decay of Ar resonance levels produces vacuum ultraviolet (VUV) radiation at 104.8 nm and 106.7 nm, which can also serve as an energy source that enhances surface reactions [142, 143].

This study is motivated by multiple step semiconductor etching processes, in which plasma operating parameters are varied over the course of the process to improve process outcomes. For example, through-silicon vias (TSV) join two or more chips by vertical interconnects running through

the stack to build three dimensional integrated circuits (3D IC). The interconnects are created by using plasmas to etch holes (vias) with high aspect ratio (etch depth to width ratio up to 20:1) and smooth sidewalls to optimize filling the holes with conducting materials. Aspect ratios for TSV applications are higher than those typically used in device fabrication, i.e., ∼3:1 for poly-Si gate etching. The Bosch process, created to etch high aspect ratio trenches and through holes (vias), is a multi-step plasma etch process that alternates between two plasma conditions optimized for high etch rate and polymer deposition (to inhibit lateral etching of feature sidewalls), respectively [118, 144, 119]. Plasma conditions are alternated on a one second time scale during the process, creating dynamic conditions that are challenging to monitor.

As described in Chapter 2, OES diagnostics for *static* plasma conditions have been developed to determine an extensive set of plasma parameters, including electron temperature, T_e [145, 59, 146, 94], electron density, n_e [94], and concentrations of metastable and resonance levels, n_m and n_r, respectively [75, 93, 147]. In this study, the static analysis is adapted to develop a real-time OES based diagnostic measuring T_e, n_e, n_m and n_r for Ar-containing plasmas under dynamic plasma conditions. The time resolution of this real-time OES system is designed to be comparable to the time scale of perturbations to the plasma in multi-step plasma processes, i.e, as low as one second. To evaluate the feasibility of this real-time OES diagnostic, it was tested while systematically varying operating conditions dynamically. Pressure (1-25 mTorr), power (100-1000 W) and Ar fraction (50-100%) of gas mixtures (Ar/N_2, Ar/O_2, Ar/H_2) were varied on a time scale of seconds to tens of seconds. OES measurements were made with a fiber-coupled *Verity* SD1024FH spectrometer with a 1024 pixel CCD array and 1.4 nm spectral resolution (Sec. 3.2.1) as conditions evolved, and the accuracy of the derived plasma parameters was assessed by comparing to Langmuir probe and white light absorption (OAS) measurements made under static conditions at the same operating conditions.

Development of a real-time OES diagnostic involved adapting the *static* OES analysis to a low-cost, low-resolution *Verity* spectrometer. These widely available spectrometers allow spectral measurements with ∼1 nm resolution over a wide wavelength range and with fast time response (millisecond scale). A flow chart of the analysis showing wavelengths used is shown in Figure 8.1.

The design of the real-time OES diagnostic includes both a system to dynamically control plasma operating parameters and diagnostic hardware and software. The dynamic control system is used to

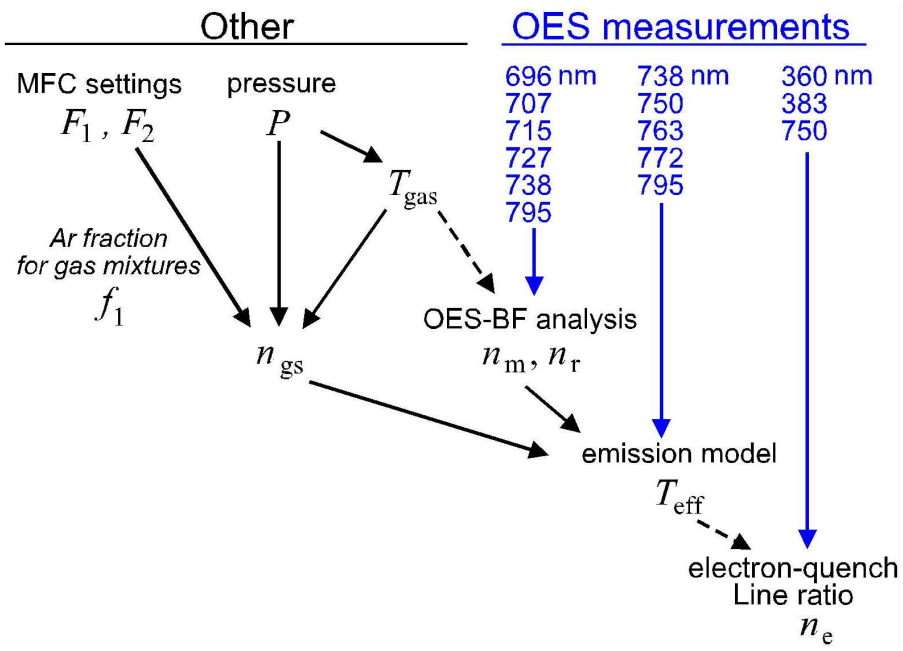

Figure 8.1: Flow chart for OES analysis to determine plasma parameters. MFC settings F_1 and F_2 refer to flow rates for up to two gases. A dashed line indicates that the analysis is only weakly dependent on the quantity.

deliberately change plasma operating parameters while the plasma is on, including pressure, power and the Ar fraction of gas mixtures, to simulate changes to the plasma in industrial multi-step plasma processes. The real-time OES system was evaluated under dynamic plasma conditions in which operating parameters were systematically varied. A detailed description follows.

8.1.1 Dynamic control of plasma conditions

To systematically vary plasma conditions, operating parameters are swept using the system pressure controller, the RF power supply for ICP power coupling, mass flow controllers and a PC running a *LabVIEW* program that controls and records operating parameters as a function of time. For experiments involving real-time changes in pressure, the pressure setpoint of a commercial pressure controller (utilizing a throttle valve in the exhaust line) is adjusted manually. During the time required to reach the new setpoint pressure (~30 seconds to increase from 1 mTorr to 25 mTorr, ~10 seconds to decrease) the pressure (measured with a capacitance manometer) is automatically recorded at intervals of 17 millisecond via the *LabVIEW* control program. The output of the RF power supply which runs the plasma is set by the control program according to user input. Typically

a 'continuous' ramp from 100-1000 W (with 15 W steps) requires ∼40 s. An instantaneous power level step change, i.e., from 1000-600 W, was also used to evaluate the time response of the real-time OES system. The Ar fraction of gas mixtures is determined by the relative flow rates of the gases. Mass flow controllers are programmed to vary the Ar fraction. It takes ∼30 s to replace the Ar gas in the chamber with an equal volume of N_2 (or H_2 or O_2). However, the effective Ar fraction under dynamic conditions depends on both the instantaneous relative flow rates and the pre-existing composition. Real-time measurements of the Ar fraction are discussed in Section 8.1.2. The time scales of changes in plasma conditions produced by this dynamic control system are comparable to those in multi-step industrial plasma processes.

8.1.2 Real-time OES system

The real-time OES system monitors the operating conditions and plasma parameters simultaneously. The plasma conditions are readily read out from the *LabVIEW* control program and imported to a real-time monitor program, developed to derive the plasma parameters from recorded emission intensities using OES analysis. The built-in clock of the real-time monitor program is used to as the time reference for all measurements.

The procedure of the real-time OES method includes three main steps: (i) acquiring a spectrum, (ii) extracting Ar emission line intensities from the spectrum, and (iii) converting emission intensities to plasma parameters (Fig. 8.1). Plasma parameters are obtained from the analysis of the small set of emission lines listed in Fig. 8.1, along with the value of the ground state Ar density. To determine plasma parameter values, emission line ratios predicted by the model for a wide range of possible plasma parameter values are compared to the measured line ratios to find the best 'fit' (as described in Chapter 2).

To implement the real-time OES system, several challenges had to be addressed. The real-time feature of this optical diagnostic is built on the millisecond-scale spectrum acquisition time of the *Verity* spectrometer, as described in Chapter 4 (Fig. 3.2). However, the fast response time is obtained at the expense of a a low spectral resolution (∼1.4 nm). First, the limited spectral resolution of the spectrometer complicate the selection of emission lines used in the OES analysis, even in pure Ar, because some Ar ($2p_x \rightarrow 1s_y$) emission lines overlap with neighboring Ar peaks (i.e., 772.38 and 772.42 nm) and can not be resolved (Fig. 8.2). The second challenge is to extract Ar emission

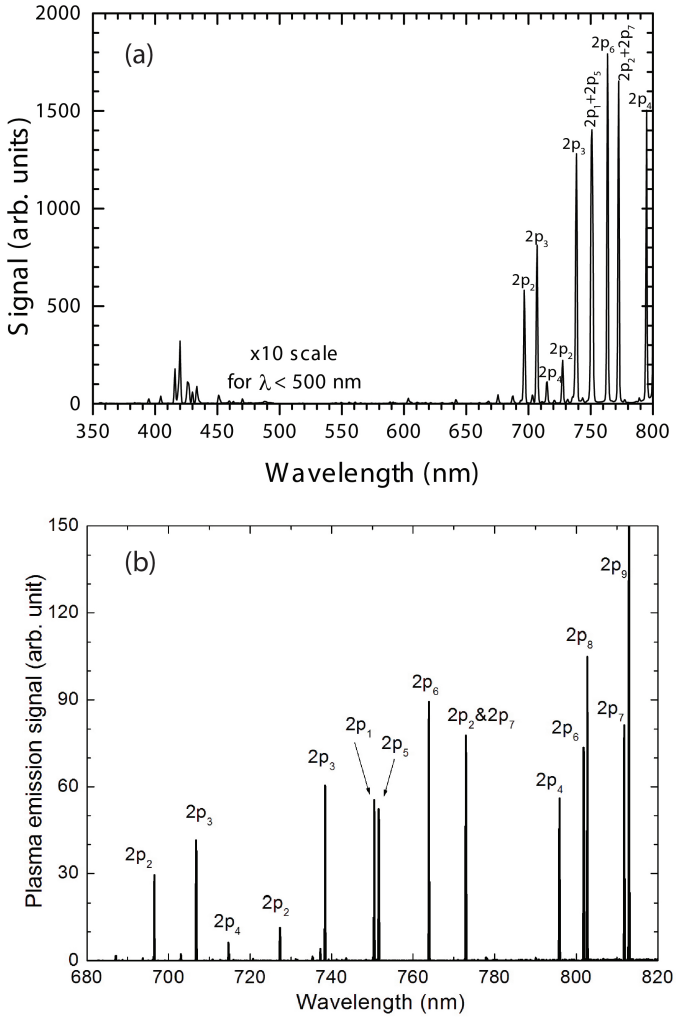

Figure 8.2: Sample Ar spectrum (600 W, 15 mTorr ICP) recorded with (a) the Verity spectrometer (1.4 nm effective resolution), and (b) the high resolution spectrometer (0.1 nm effective resolution). Only part of the spectrum recorded by the high resolution spectrometer is plotted as a comparison to that from the *Verity* spectrometer to illustrate the limited spectral resolution of the *Verity* spectrometer.

intensities from the spectra of plasmas in which Ar is mixed with molecular gases. Indeed, molecular emissions occur at many of the same wavelengths as Argon peaks used in the OES analysis. In previous studies of *static* OES measurements [75], a high resolution system (i.e, a PMT in conjunction with a monochromator) was used, so that the recorded atomic Ar spectral peaks (∼0.1 nm) appeared to be narrow spikes compared to the broad molecular spectra. Under this circumstance, it is easy to extract Ar atomic peak areas numerically from the molecular 'background' emissions. However, using the *Verity* spectrometer in the real-time OES system, the widths of atomic Ar peaks

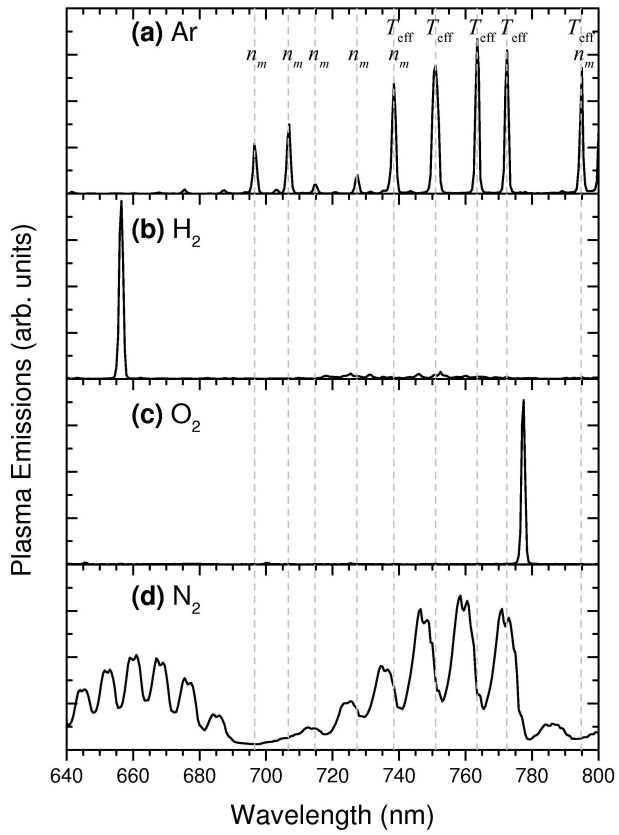

Figure 8.3: Plasma emission spectra (15 mTorr, 600 W ICP) recorded with the Verity spectrometer. Vertical dashed lines denote locations of Ar peaks used to determine Ar($3p^5 4s$) number densities (n_m), and the effective electron temperature (T_{eff}).

(∼4 nm) are no longer negligible compared to the widths of the molecular emission spectral features. As illustrated in Fig. 8.3, the hydrogen and oxygen spectra are dominated by atomic emission lines, with little overlap at the Ar emission wavelengths used in OES analysis. The overlap between nitrogen and Ar spectra, however, are much more significant and complicated, thus motivating the development of an alternate analysis strategy. In addition, estimating the Ar ground state density for plasmas in Ar/molecular gas mixtures becomes more difficult under dynamic plasma conditions that involve time-varying Ar fraction. Finally, to achieve fast time resolution, it is required to acquire emission spectra and conduct the OES analysis (Fig. 8.1) quickly.

Electron temperature In the previous study of argon plasmas produced by our ICP system in the 1-25 mTorr pressure range, the EEDFs were found to be well represented by the x-form (T_x, x) with a fixed value x=1.2 [59, 74]. Therefore, in the real-time electron temperature measurements

presented in this chapter, a fixed value of x=1.2 is used. The electron temperature is derived from the relative optical intensities of selected Ar emission lines as described in Chapter 2. The most accurate electron temperature results are achieved when the set of lines analyzed include emissions originating from a variety of upper levels, where some levels are populated primarily via excitation of ground state atoms by high energy electrons and some levels are populated primarily by excitation of metastable atoms by low energy electrons. Unfortunately, out of the 10 achievable Ar ($2p_x \rightarrow 1s_y$) emission peaks, only one line (763 nm) is dominated by excitation of metastables. In order to prevent the fitting process from being dominated by high-energy electrons, only the 4 largest peaks in the ground-state dominated category are included in the analysis (Fig. 8.1). This selection adds two benefits: only a limited wavelength range (736-797 nm) is used, so that the errors introduced by wavelength dependent spectral sensitivity are minimized, and by only using the most intense emissions, the effect of errors in subtracting the background spectrum is minimized.

Electron density The electron quenching of electronically excited states is used to determine electron density with a single Ar emission line ratio due to optical emissions out of two excited levels with distinct lifetimes (as described in Section 2.3.3). Due to the low resolution of the *Verity* spectrometer, the $5p_5/3p_1$ ratio used by Zhu *et al.* in Ref. [94] is ruled out in this real-time OES system, due to the inability to resolve either of these lines. Instead, a $4p_5/2p_{1,5}$ line ratio 'pair' is selected here. The denominator of the line ratio is actually the sum of the $2p_1$ and $2p_5$ contributions at 750.39 nm and 751.47 nm.

One benefit of using the $4p_5/2p_{1,5}$ line ratio is that there is a built-in means of cross checking the electron density results. Two different emission lines (360.65 nm and 383.47 nm) from the $4p_5$ can typically be resolved even at 1.4 nm resolution. Because these two lines have almost equal transition probabilities (0.76 and 0.75 $\times 10^6$ s^{-1}) [61], the two $4p_5$ peaks should be almost identical in size (in the absence of any background). Two reasonably close electron density values should be derived from a single spectrum by using both of the two $4p_5$ lines. A considerable difference between the electron densities obtained from using different $4p_5$ emission lines indicates a potential error in electron density measurements.

Extracting Ar emission intensities from Ar-molecular gas mixtures

As illustrated in Fig. 8.1, Ar emission intensities extracted from recorded spectra are necessary inputs to obtain plasma parameters. For Ar/molecular mixed-gas plasmas in which the Ar spectral lines are generally immersed within a thicket of molecular emissions, special background subtraction schemes are needed to extract Ar emission intensities, beyond the standard background subtraction used for pure Ar [140]. The sophistication required in the molecular background subtraction depends upon the degree of molecular contamination (Fig. 8.3). Thus, two different background subtraction schemes have been applied to extract Ar emission intensities from molecular gases: (i) the trapezoid background method for O_2 and H_2, and (ii) the spectral background method for N_2.

Trapezoid background subtraction For cases with either minor overlap between molecular and Ar spectral features, or where the background varies linearly over the wavelength region of interest (Ar/H_2 and Ar/O_2 mixes), a trapezoid background subtraction process, corrected for nonzero Ar emissions at the edges of the peak regions was implemented. As illustrated in Fig. 8.4, the gray shaded region corresponds to the integrated area of the raw spectra without background subtraction. Defining the S_L and S_R to be the recorded signals at the left and right edges of the spectral peak region (λ_L, λ_R), the conventional estimation of the background contribution is equal to the trapezoidal area under the dashed line.

This standard approach assumes zero background signal for the pure Ar emission region, which is typically not the case for the *Verity* spectrometer. Particularly for the weaker emission lines, the overlap with neighboring lines can be significant, so that the standard approach tends to overestimate the background. Therefore, the effective molecular background signal at Ar peak edges (S'_L and S'_R) is calculated by excluding the residual emission signal for pure Ar spectra.

The non-zero background signals at the edges of the peak region are estimated from their ratios (ξ_L and ξ_R) to the Ar emission intensity (S'_P) at the center of peak regions (λ_P) in pure Ar spectra. Finally, the revised background (cross hatched region in Fig. 8.4) can be obtained by substituting the corrected S'_L and S'_R into the conventional background calculations. Detailed derivation of this background subtraction method can be found in Ref. [140].

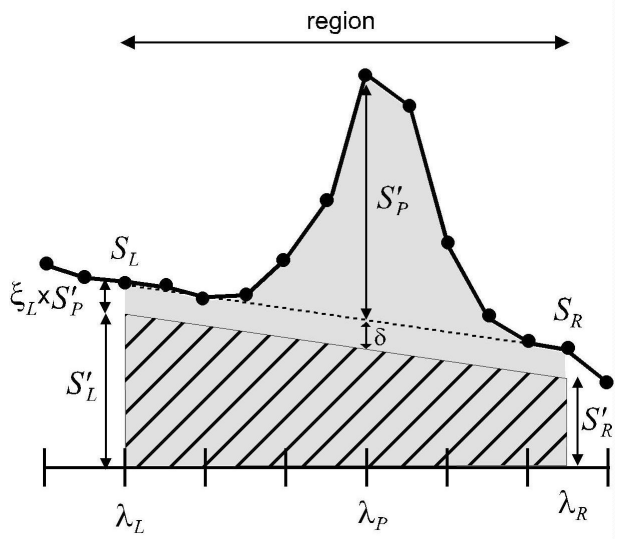

Figure 8.4: Trapezoid background subtraction which accounts for residual Ar emissions at edges of the region of interest.

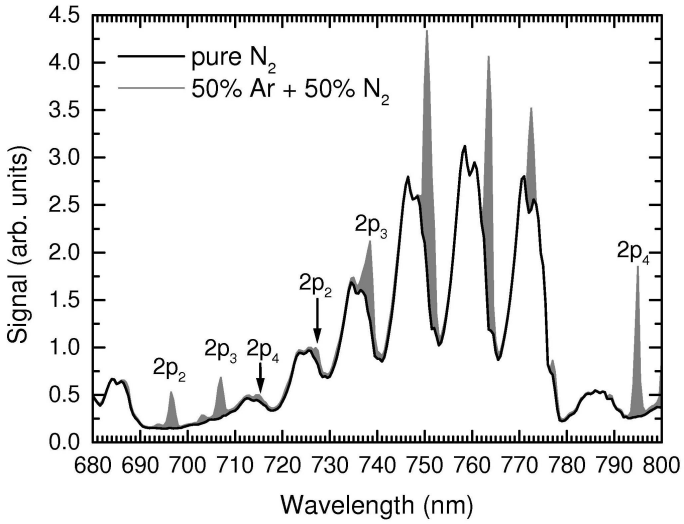

Figure 8.5: The two spectra obtained with the Verity spectrometer for a pure N_2 plasma and a 50-50 Ar-N_2 plasma (15 mTorr, 600 W). The amplitude of the nitrogen spectrum has been scaled to match the nitrogen contribution in the mixed gas spectrum. The gray features are Argon emission lines, the intensities of which are determined by subtracting off the scaled spectrum of the pure N_2 plasma.

Spectral background subtraction In contrast to O_2 and H_2, N_2 has broad emission bands that overlap with the Ar spectral region used in the OES-BF analysis (Fig. 8.3), and the trapezoid background subtraction method produces poor agreement with results obtained using a high resolution spectrometer. Thus, another method referred to here as 'spectral background subtraction' was developed. The basic idea of spectral background subtraction is to take a spectrum from a pure N_2 plasma, multiply the magnitude of the spectral intensity by a scale factor so that the N_2 intensities match those of the N_2/Ar mixture, and then subtract it from the mixed Ar/N_2 spectrum to yield the Ar spectrum (Fig. 8.5). Assuming the Ar has negligible contribution to the signal at the edges of the peak region of interest, the signal at the edges are used to define the scale factor.

Similar to the trapezoid background subtraction, the non-zero Ar signal at the edges of emission regions is accounted in order to calculate a more accurate scale factor. Separate scale factors are calculated for each Ar emission peak rather than using one universal value for the entire spectrum, to allow for some variation in the relative magnitudes of the different vibrational bands for the spectra acquired with mixed and nitrogen-only plasmas. Detailed derivation of this background subtraction method can be found in Ref. [140].

Estimating the Ar ground state density

In addition to the emission intensities, the Ar ground state density is another necessary input to the OES analysis (Fig. 8.1). The Ar ground state density is calculated from the ideal gas law with the Ar partial pressure and gas temperature as inputs. The value of the gas temperature can either be assumed constant at some representative value (i.e., 750 K) or it can be measured with laser absorption spectroscopy [148]. The Ar partial pressure in the chamber is only required for gas mixtures and can be obtained from the flow rates of the gases read from the mass flow controller and the total pressure under static gas composition conditions.

When the Ar fraction is changing dynamically, the effective gas composition for Ar-molecular gas mixtures depends on both the 'instantaneous' relative Ar flow rates that the mass flow controllers report and the pre-existing composition in the chamber. Therefore, the effective Ar fraction at time T is estimated by averaging the 'instantaneous' relative Ar flow rates from $T - \Delta t$ to T where Δt is a time constant for reaching a new steady state when the flow rate has changed. In principle, it is possible to calculate the appropriate average time Δt based upon the chamber volume, pumping

speed, and total flow rates. In practice, Δt is measured as how long the system took to settle to a new equilibrium after a step change in the mass flow controller (MFC) settings by monitoring the Ar emission intensities.

Real-time data processing

As discussed in Chapter 2, a numerical 'fit' process is required to convert Ar emission intensities to plasma parameters of interest. For a particular choice of trial plasma parameter values, χ^2 values are calculated using the experimental and model predicted line ratios. This numerical calculation is repeated for an array of possible plasma parameter values with the location of the minimum χ^2 corresponding to the 'best fit' plasma parameter results. The real-time feature of the OES diagnostic system here requires a fast 'fit' process.

The *SpectraView* software provided to control the *Verity* spectrometer and record emission spectra includes a data processing feature which can be used for the emission model analysis. However, the *Verity* spectrometer is mainly designed for endpoint detection in semiconductor etching systems so that the speed of the *SpectraView* software for heavy numerical data processing is insufficient for real-time analysis. Therefore two strategies were developed: 1) a 'fast' gradient search algorithm which reduces the numerical processing time and 2) an interface from the *SpectraView* program that transfers spectra to a more suitable numerical processing program, such as *LabVIEW*.

The 'fast' gradient method developed for the OES analysis starts with an initial guess for metastable and resonance densities and uses the local slope of the χ^2 surface to obtain refined estimates for metastable and resonance densities. Assuming the search isn't trapped in a local minimum, the number of evaluations before finding the best fit is much less than trying all possible values. Furthermore, once located, this pair of metastable and resonance densities can be used as the starting point for following iterations of the sequence, essentially permitting real-time tracking of metastable and resonance densities. The numerical calculation time in the OES analysis was reduced to less than 5 s by using this algorithm.

Another strategy to improve the data processing speed is exporting spectral data out of the *SpectraView* software to conduct the numerical processing with a more suitable program which is the *LabVIEW* program in this project. Binary data files stored on the hard disk, which can be read and written while the *SpectraView* and *LabVIEW* program are running, shuttle values between

these two programs. The fitting process takes about 50 ms in *LabVIEW* program. In addition, the 'fast' gradient algorithm can be applied to the 'fit' calculations in *LabVIEW* program to further decrease the data processing time. However, in this project, the time spent exporting the spectral line intensities into the *LabVIEW* program is ∼100 ms, which dominates the data processing time. Since the data processing can occur simultaneously with a new spectrum being recorded, the total time from the spectra acquisition to obtain the plasma parameters is approximately 100 ms.

8.1.3 Sample results

To evaluate the real-time OES system, a series of measurements were conducted under dynamic conditions as the chamber pressure (1-25 mTorr), power (50-1000 W) (for pure Ar) or Ar percentage (50-100 %) (for Ar-molecular gas (N_2, O_2, H_2) mixtures) were respectively ramped up and down over a period of about 100 seconds. The plasma parameters derived from the real-time OES measurements were compared with OAS (n_m, n_r) and Langmuir probe (T_e, n_e) results obtained under static conditions (described in Chapter 4). In this section, two sets of dynamic measurements are presented for: (1) a pure Ar plasma as the chamber pressure is varied and (2) an Ar/N_2 plasma as Ar fraction is varied. The EEDF (or electron temperature) changes with the source pressure such that the first set of sample measurements provide a test of the capability of this real-time OES diagnostic to capture the electron temperature variation. For the second set of sample measurements, the N_2 spectrum has significant overlap with Ar lines of interest, and thus provides a test of the background subtraction method. The dynamic estimation scheme to determine the Ar fraction in gas mixtures is also tested.

Figure 8.6 illustrates the performance of the real-time OES measurements under dynamic conditions as the chamber pressure is ramped up and down between 1 and 25 mTorr over a period of 100 seconds. Also plotted in Fig. 8.6b-d are the values of the effective electron temperature, electron density, and Ar($3p^5 4s$) number densities measured by probe and white-light OAS *taken under static conditions* plotted at times corresponding to moments when the pressure equaled the values of the static measurements. The OES-derived plasma parameters evolve in time in response to the pressure change. Agreement (±10%) in T_{eff} (x=1.2), n_e and $1s_5$ and $1s_4$ number densities obtained from the real-time *Verity* OES analysis and the static probe and OAS measurements were observed. While these static measurements required many minutes of data collection and analysis,

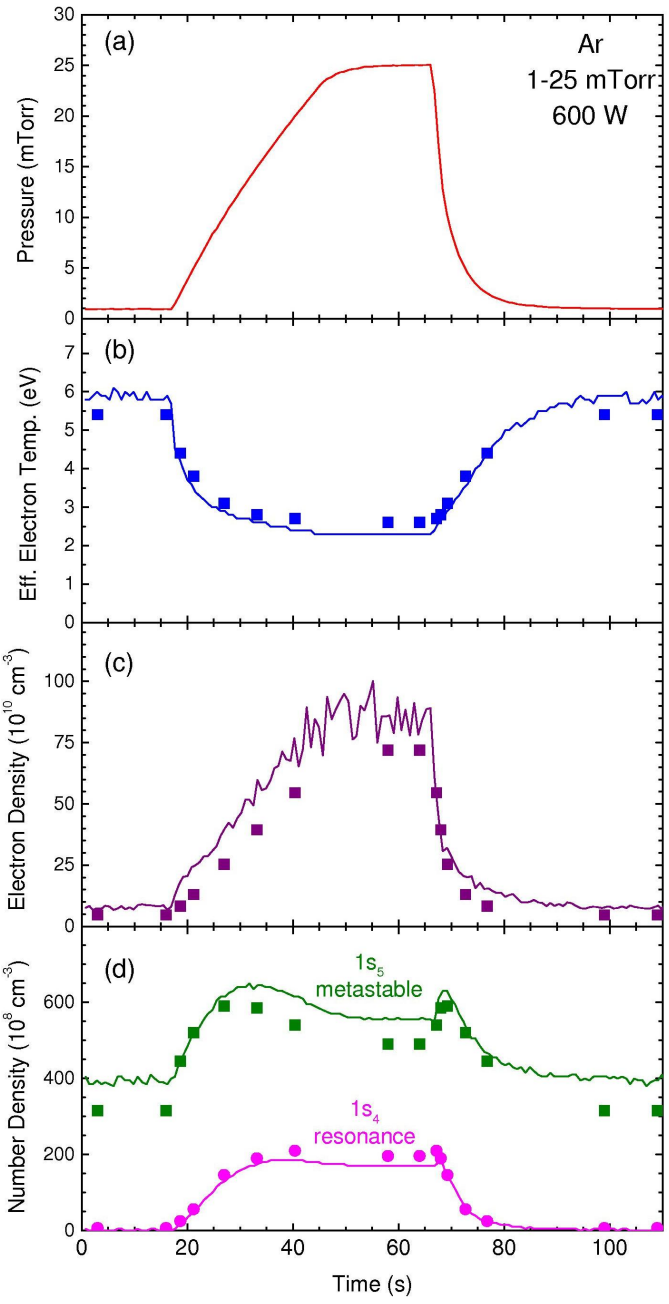

Figure 8.6: Real-time spectroscopic measurements for 600 W Ar ICP (lines) as a function of time (a) source pressure, (b) T_{eff}, (c) n_e and (d) $1s_5$ and $1s_4$ number densities. Points represent values obtained by Langmuir probe and OAS under static conditions at fixed values of the pressure [76].

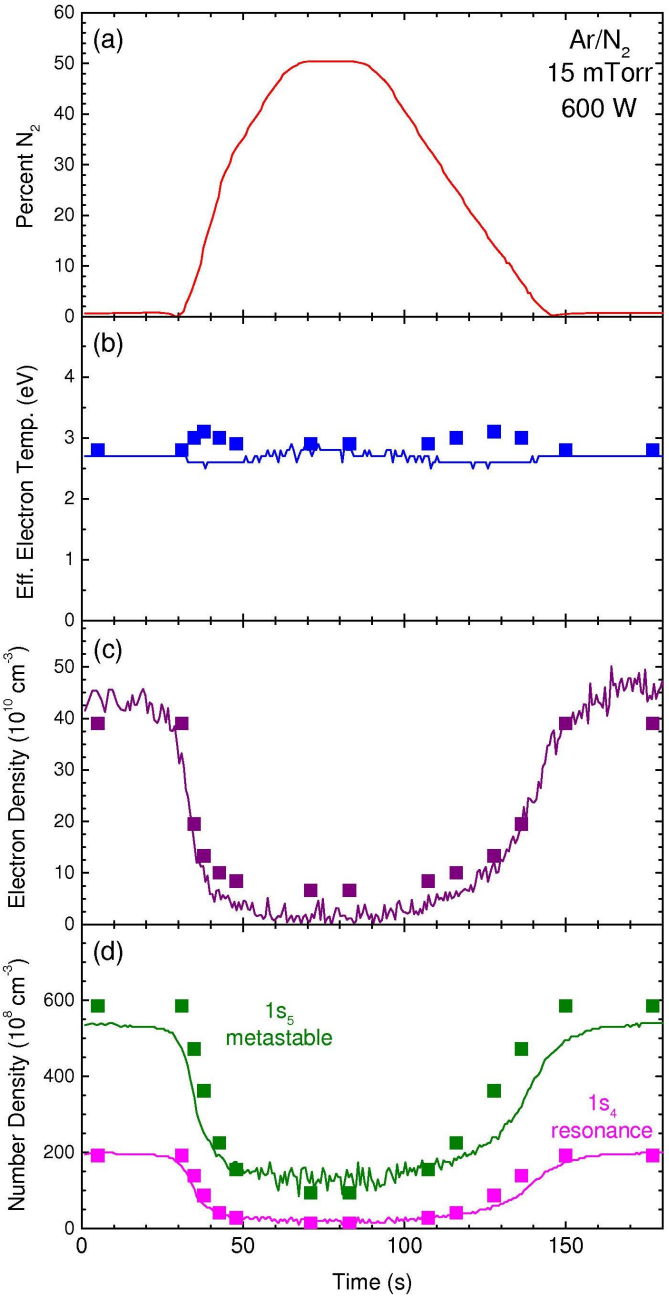

Figure 8.7: Real-time spectroscopic results for 15 mTorr, 600 W Ar/N_2 ICP (lines) as a function of time (a) N_2 percentage, (b) T_{eff}, (c) n_e and (d) $1s_5$ and $1s_4$ number densities. Points represent values obtained by Langmuir probe and OAS under static conditions at fixed values of the N_2 admixture [76].

the OES values in Fig. 8.6b-d were obtained in real-time at an update rate of 2 Hz.

Fig. 8.7 plots the plasma properties as a function of time as the N_2 percentage is dynamically varied between 0 and 50% over 100 seconds. Adding nitrogen to the plasma has two primary effects as far the Ar OES diagnostic is concerned, First, collision-transfer reactions between N_2 and metastable Ar atoms quenches the metastable Ar atoms. Second, vibrational and rotational excitation of N_2 molecules soak up a lot of energy, reducing energy that previously went into ionization of Ar atoms, reducing the plasma density in the Ar/N_2 mixes. One thing that remains basically unchanged, however, is the electron temperature owing to the similar ionization energies of Ar and N_2. All three effects are well illustrated in Fig. 8.7.

As demonstrated from the sample data presented here and the more extensive comparison of results in Ref. [140], it is possible to use a low-resolution spectrometer to perform real-time, non-invasive measurements of the electron temperature as well as other plasma properties in a wide variety of plasmas. Note that this capability was partially achieved by restricting the assumed shape of the EEDF, which was assumed to be characterized by only a single parameter the effective electron temperature (T_{eff}).

8.2 'Low resolution' OES diagnostic for x-form EEDFs

To move beyond the assumption of a Maxwellian distribution, or a fixed EEDF shape (i.e., x=1.2, determined by other means), the general approach of the preceding chapters is to expand the number of emission lines used in OES analysis to include levels with different excitation threshold energies. Indeed, as illustrated in Ref. [59, 74], there is not enough information in only the Ar 2p emission lines used in the analysis of Sec. 8.1 to simultaneously constrain both the values of T_x and x. The difficulty with a low-resolution spectrometer is to find additional lines that can be sufficiently resolved from neighboring emissions and used in the analysis. To further simplify this problem, in this section the study is restricted to a pure Ar inductively coupled plasma with no injected electrons. By varying the source pressure, a variety of EEDF shapes can be generated with depleted high energy tails.

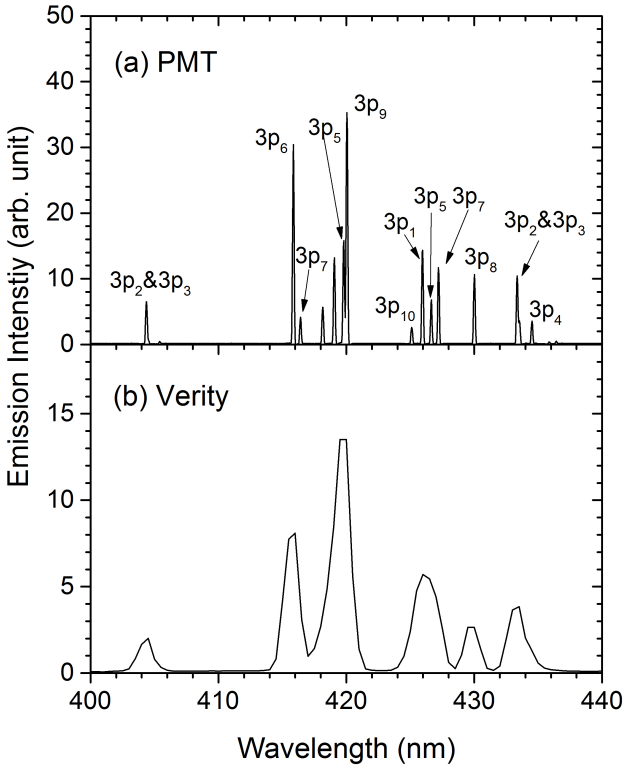

Figure 8.8: Portion of an Ar spectrum (600 W, 15 mTorr ICP) recorded with (a) the high resolution spectrometer, i.e., PMT (0.1 nm effective resolution), and (b) the Verity spectrometer (1.4 nm effective resolution).

8.2.1 Extracting Ar 3p emission intensities

The selection of Ar 3p emission lines used in the OES analysis is limited by the low spectral resolution (∼1.4 nm) of the *Verity* spectrometer. A portion of an Ar spectrum recorded with the high resolution spectrometer (i.e., PMT) and the *Verity* spectrometer is plotted in Fig. 8.8. Most of the Ar ($3p_x \rightarrow 1s_y$) emission lines overlap with neighboring Ar peaks (i.e., 419.83 and 420.07 nm) and cannot be resolved in the low resolution spectra.

In preceding chapters, emissions from individual emission lines were used in the fitting process. The analysis with the low-resolution spectrometer is performed on wavelength regions, where each region contains one or more Ar emission lines. When multiple emission lines occur within a region, the contributions from different sources are summed together. Table 8.1 lists the wavelength regions

Table 8.1: Wavelength ranges defined for Ar 3p emission lines in Verity spectrometer. The intense Ar 3p peaks contained in each peak region are listed. These Ar 3p emission lines are used in addition to the 2p lines in the emission analysis.

peak region in *Verity* $\lambda_1 - \lambda_2$ (nm)	lines in region
414 - 417.5	415.8 ($3p_6$), 416.42 ($3p_7$)
417.5 - 422	418.19 ($3p_2$), 419.07 ($3p_8$), 419.10 ($3p_4$), 419.83 ($3p_5$), 420.07 ($3p_9$)
428.5 - 432	430.01 ($3p_8$)
432 - 437	433.36 ($3p_3$), 433.53 ($3p_2$), 434.52 ($3p_4$)
449 - 454	451.07 ($3p_5$), 452.23 ($3p_{10}$)

of argon 3p lines as used with the *Verity* spectrometer. These Ar 3p emissions lines are used in the emission analysis in addition to the Ar 2p lines. With one exception, all the intervals contain the contributions from multiple Ar lines. These combined peaks reduce the information content that is gained by adding more lines to the analysis. For example, the 419.83 nm emission line is mainly sensitive to ground state excitation, whereas the 420.1 nm emission line shifts from being ground state dominated at higher electron temperatures to metastable excitation dominated at lower electron temperatures. Thus, an analysis of the 420.07/419.83 nm line ratio is a sensitive test of the electron temperature [149]. However, if only the sum of 419.83 and 420.07 nm line intensities is known, this information about the EEDF is essentially lost.

8.2.2 Sample OES measurements

To evaluate the 'low-resolution' OES diagnostic for both T_x and x, a series of measurements were conducted for a 600 W ICP for argon pressure between 2.5 and 30 mTorr. The EEDF (T_x, x) derived from the OES method were compared with Langmuir probe results. An increase in the operating pressure leads to a decrease in the electron temperature (T_x). This trend is well reflected in our OES and probe measurements (Fig. 8.9a). The absolute T_x values obtained from the OES method agree within $\pm 15\%$ with the Langmuir probe results at all pressures. However, the values of EEDF shape parameter (x) obtained from the probe and OES measurements were inconsistent. In the 2.5-30 mTorr range, the x value obtained from the probe was observed to increase with the

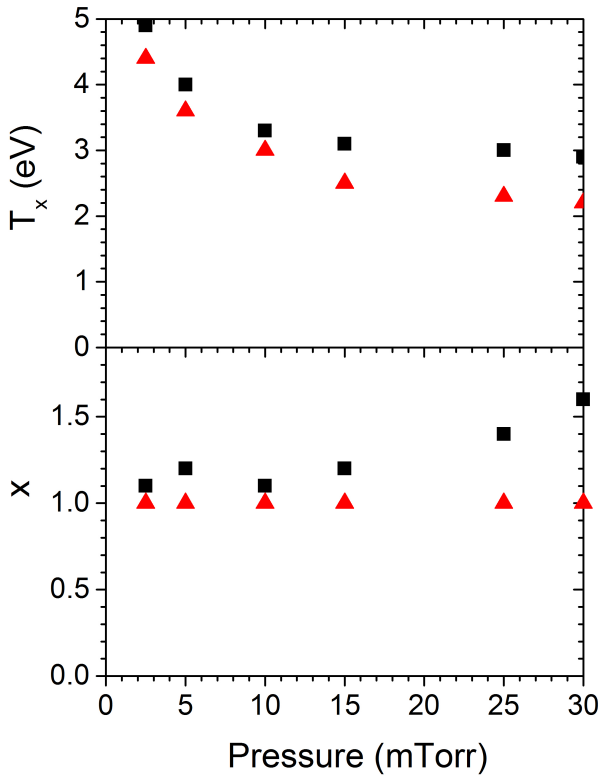

Figure 8.9: Variation of electron temperature T_x and EEDF shape parameter x with pressure for a 600 W Ar ICP. Squares are from probe values, and triangles are from OES measurements using a low-resolution spectrometer.

source pressure from 1.1 to 1.6, while the OES-derived x was fixed at the value of 1 (Fig. 8.9b). Therefore, the 'low-resolution OES' method is not able to capture the variation of x over the 2.5-30 mTorr pressure range.

To examine the sensitivity of the OES shape parameter x, the χ^2 difference between the model and experimental line ratios as a function of T_x and x for the 15 mTorr case is plotted (Fig. 8.10). Numerous trial EEDFs described by the pair of parameters (T_x, x) running along the line from T_x = 2.4 eV, x = 1 to T_x = 3.4 eV, x = 1.8 have approximately equal quality fits (within ±10% of the minimum χ^2 value) to the observed OES line ratios. There is not enough information in the low-resolution spectra to distinguish between these parameter pairs.

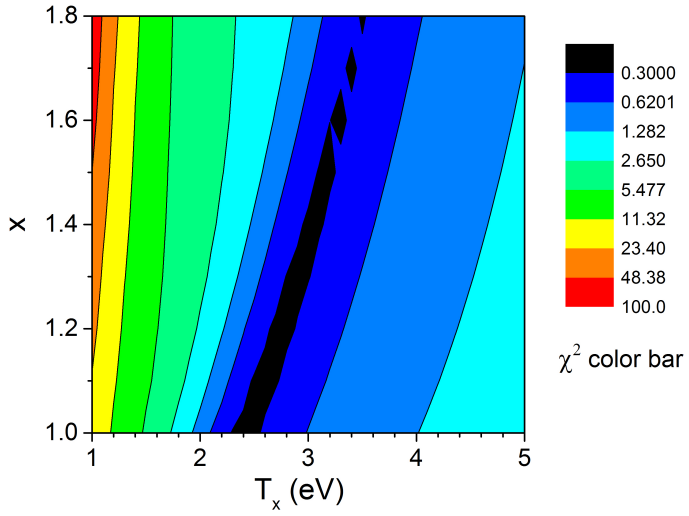

Figure 8.10: Contour plot of χ^2-values for 15 mT 600 W Ar plasma with smaller values of χ^2 correspond to a better quality fit.

8.3 'Low resolution' OES diagnostic for enhanced EEDF tails

The OES diagnostic for enhanced EEDF tails using Ar, He and He emissions has been developed and illustrated in previous chapters. In this section, the emission analysis (described in Chapter 6) is adapted to the spectra recorded with the low-resolution *Verity* spectrometer to determine EEDF tails. OES measurements of EEDFs with both the low-resolution and the high-resolution spectrometer are conducted in an Ar-containing ICP with electron injection as a function of electron injection current. The 'low-resolution' OES diagnostic is illustrated by checking the dependence of the EEDF tail density on the variation of electron injection current. The accuracy of the low-resolution OES-derived EEDF tails is assessed by comparing with the results obtained using a high-resolution spectrometer.

8.3.1 Apparatus

The setup for real-time OES diagnostic using the *Verity* spectrometer has been discussed in Sec. 3.2.1 (Fig. 3.2). In Fig. 3.2, the optical fiber views the plasma through a viewport directly opposite the Langmuir probe. The filament electron source, however, produces a huge amount

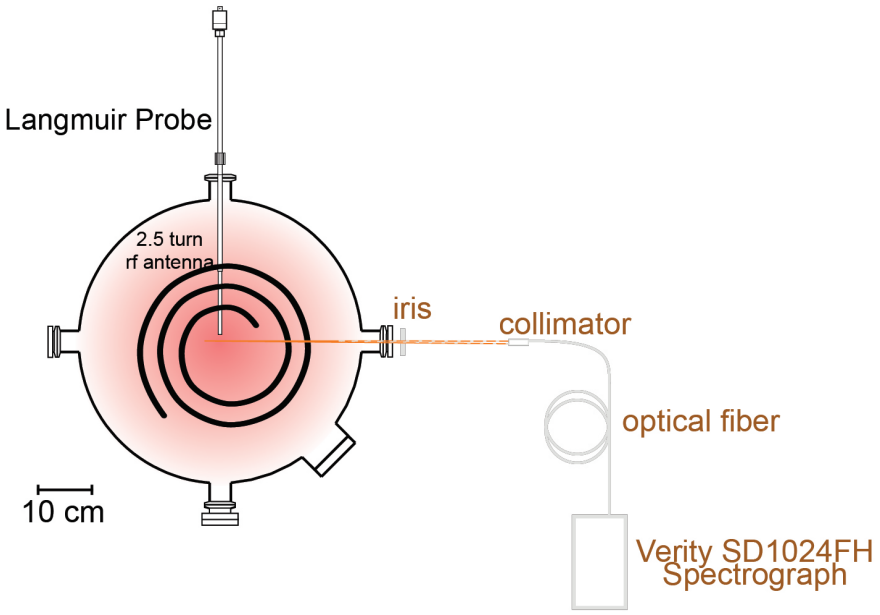

Figure 8.11: Top down view of ICP system showing the compact, fiber coupled Verity spectrometer for low-resolution OES diagnostic for enhanced EEDF tails.

of blackbody radiation. This light scatters off of the probe tip, which completely dominates the spectrum measured by the spectrometer. This problem is greatly reduced by moving the optical fiber to another viewport which excludes the Langmuir probe from the viewing region (Fig. 8.11).

8.3.2 Challenge for 'low resolution' OES diagnostic for EEDF tails

The primary challenge for the 'low-resolution' OES diagnostic for enhanced EEDF tails is to extract Ar, Ne and He emission intensities from the spectra. At a low resolution, many of the previously employed Ne and He peaks are incapable of being resolved from neighboring peaks. Sample Ne, He and Ar spectrum recorded with the *Verity* spectrometer are shown in Fig. 8.12. At ~1.4 nm resolution, the Ne 585.28 nm peak is indistinguishable from the He 587.58 nm peak and four neighboring Ar peaks between 583.42 and 588.86 nm. Without injected electrons, the emission spectra of a 5:1:5 Ar:Ne:He plasma is dominated by the Ar neutral emissions when recorded by a low-resolution spectrometer as illustrated in Fig. 8.13. Even at wavelengths of 640.22 nm and 587.56 nm which correspond to the most intense Ne and He emission lines, respectively, the spectral lines are dominated by Ar neutral emission peaks (Fig. 8.13). The 480.6 nm Ar^+ line which is well

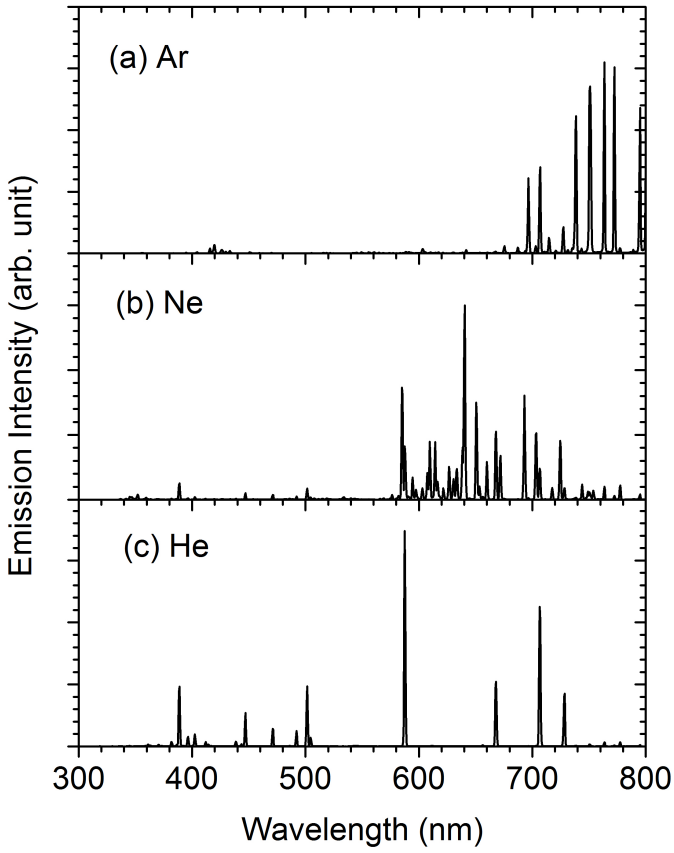

Figure 8.12: Plasma emission spectra (15 mTorr, 600 W ICP) with the Verity spectrometer.

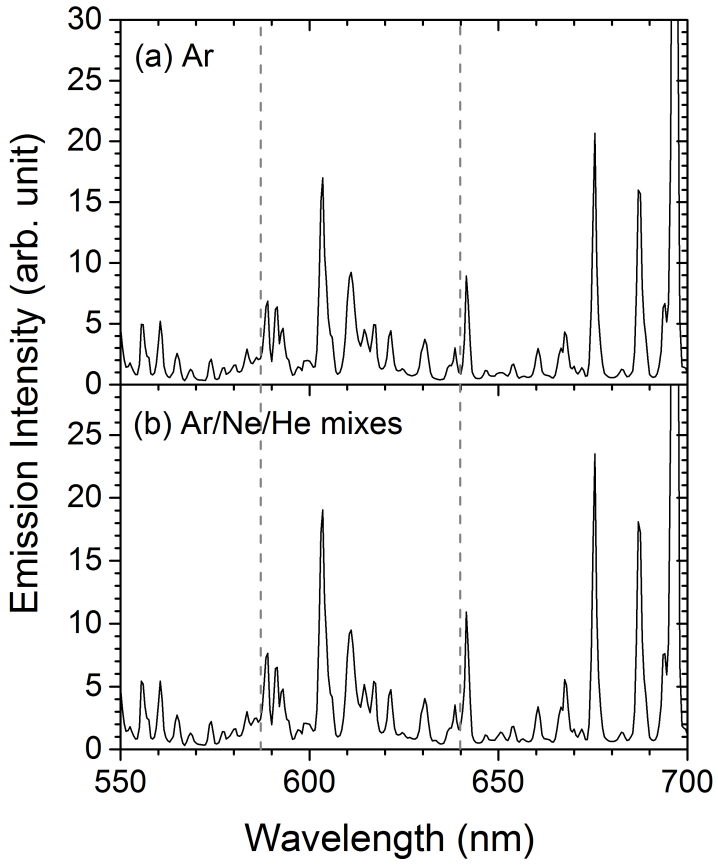

Figure 8.13: Portion of emission spectra for (a) 100 W Ar ICP and (b) 100 W mixed-gas ICP (15 mTorr Ar, 15 mTorr He and 3 mTorr Ne). Vertical dashed lines denote locations of two intense Ne and He peaks.

separated with other Ar neutral emissions is weaker than the noise level of the recorded spectra. This is because the excitation threshold energies of Ne (∼19 eV), He (∼23 eV) and Ar^+ (∼35 eV) emitting states are much higher than those of Ar neutral emitting states (∼13 eV). The Ne, He and Ar^+ emissions are much weaker compared with their neighboring Ar neutral emissions such that they cannot be recognized from the low-resolution spectra.

Despite being imperceptible in a pure ICP discharge, with injection of high energy electrons, the Ne, He and Ar^+ emissions are much more noticeable. Fig. 8.14 plots portion of the emission spectra for 100 W mixed-gas ICP (15 mTorr Ar, 15 mTorr He and 3 mTorr Ne) with and without electron injection (1 A, -50 V bias). Some intense Ne and He emission lines, i.e., 650.65 nm for

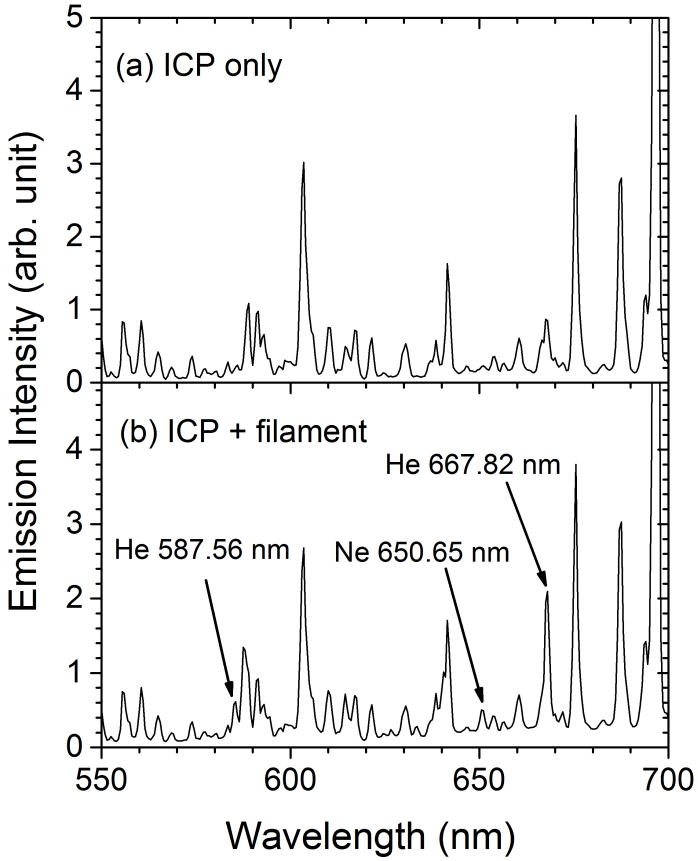

Figure 8.14: Portion of emission spectra for 100 W mixed-gas ICP (15 mTorr Ar, 15 mTorr He and 3 mTorr Ne) with and without electron injection (1 A, -50 V bias). The non-zero background for ICP+filament case is due to scattered filament light.

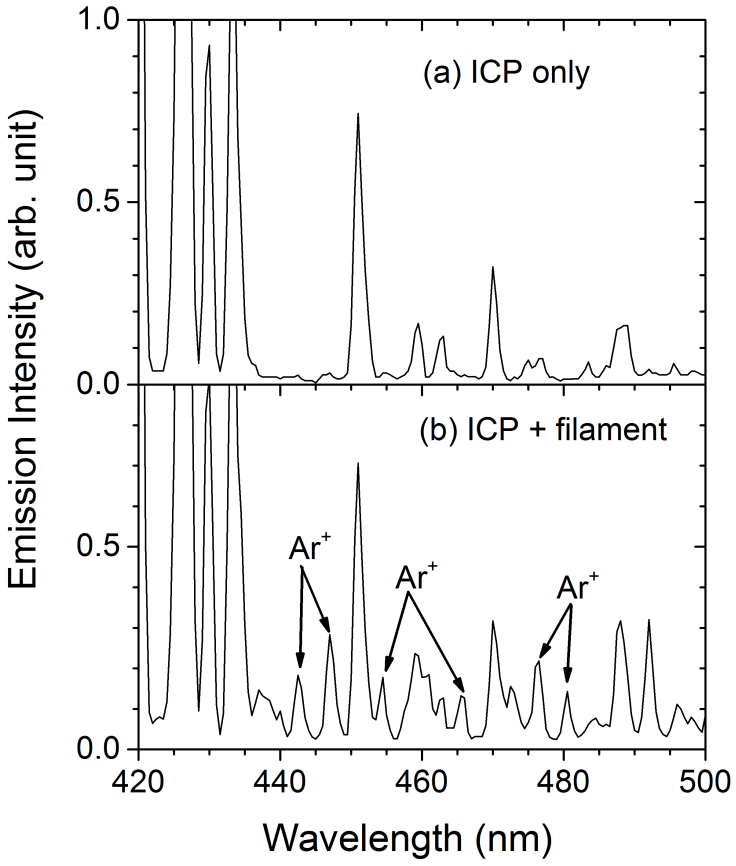

Figure 8.15: Portion of emission spectra for 100 W Ar/Ne/He ICP (15 mTorr Ar, 15 mTorr He and 3 mTorr Ne) with and without electron injection (1 A, -50 V bias). The non-zero background for ICP+filament case is due to scattered filament light.

Ne and 587.56, 667.82 nm for He, respectively, can be recognized. However, the overlap between Ne, He and Ar spectra are still significant. It is difficult to extract the intensities of the Ne and He peaks independent of the contaminating Ar lines and then use them in the emission analysis. On the other hand, there are some Ar^+ peaks which can be fully resolved when 'hot' electrons are injected to the gas-mixed ICP discharge (Fig. 8.15). As a result, in the following analysis, only Ar neutral and a few selected Ar^+ emission lines will be used in the emission model analysis of low-resolution spectra to determine EEDF tails.

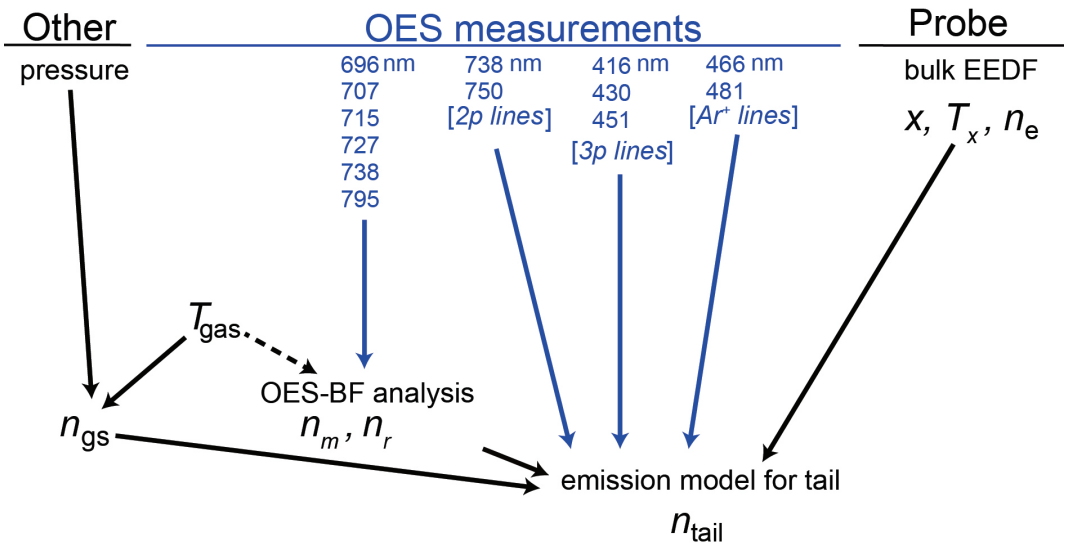

Figure 8.16: Flow chart for OES analysis to determine EEDF tails using Ar emissions. The 'bulk' EEDF (T_x, x, n_e) used in the emission analysis is obtained from the Langmuir probe.

8.3.3 Determining EEDF tails with low-resolution spectrometer

A flow chart showing the general procedure of the analysis and wavelengths used is shown in Figure 8.16. Note that the reduced number of Ar 2p and 3p 'regions'/lines are used in the analysis. In principle, many more 2p lines can be fully resolved even at 1.4 nm resolution, and more 3p regions can be used as well. Nevertheless, for the purpose of measuring only the tail region, it is advantageous to have more equal number of 'lines' in the three different categories. Considering the limitation of determining both T_x, x using the low-resolution spectrometer illustrated in Sec. 8.2.1, the 'bulk' EEDF is obtained from Langmuir probe measurements.

8.3.4 Sample OES measurements

To evaluate the capability of the 'low resolution' OES diagnostic, measurements of EEDF tails were made in a 100 W Ar-containing plasma (15 mTorr Ar, 15 mTorr He and 3 mTorr Ne) with electron injection (-50 V bias) as a function of electron injection current. The plasma parameters used in the emission analysis as a function of electron injection current are listed in Table 8.2. Note that the differences in Ar metastable densities (n_m and n_r) between the two OES methods may be attributed to the uncertainties in emission intensity measurements with the *Verity* spectrometer. Since the

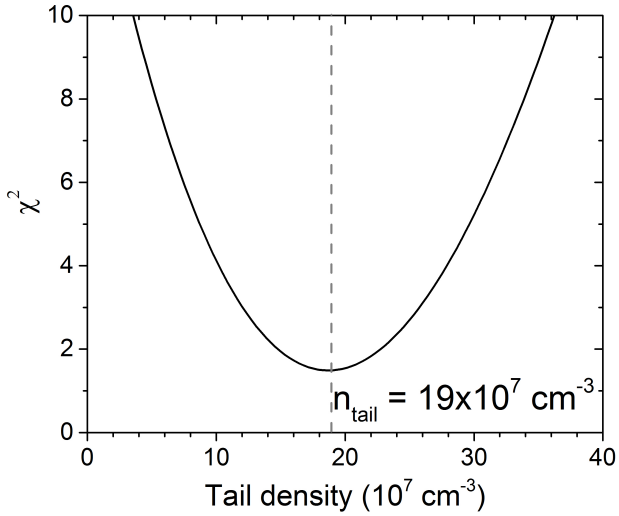

Figure 8.17: Tail density (n_{tail}) dependence of goodness of fit measure χ^2 (divided by the number of degrees of freedom) for a 100 W Ar-containing plasma (15 mTorr Ar, 15 mTorr He and 3 mTorr Ne) with electron injection (1 A, -50 V bias). Dashed vertical line correspond to best-fit value of the tail density.

Verity spectrometer has a larger solid angle compared with the high-resolution spectrometer (i.e., PMT), the effect of scattered emissions are more significant.

Using the pre-set values listed in Table 8.2 for E_{cut} and s, the tail density (n_{tail}) was obtained from the OES analysis using measurements from the *Verity* spectrometer with the resulting values are also included in Table 8.2. For instance, with 1 A electron injection current, the analysis yielded a tail density of 19×10^7 cm^{-3}. The sensitivity of the OES derived tail density can be seen by examining Figure 8.17 which plots the χ^2 difference between the model and experimental line ratios as a function of the tail density used in the model calculation. The minimum χ^2 value, corresponding to the best fit, is well localized in the neighborhood of 19x10^7 cm^{-3} with an estimated uncertainty of about $\pm$15% (for a $\pm$10% increase in the minimum value of reduced χ^2).

Fig. 8.18 compares the tail densities as a function of the electron injection current obtained from an OES analysis of the low-resolution and the high-resolution spectra. Note that the high-resolution results were obtained using a larger set of ten Ar and Ar$^+$ emission lines as described in Chapter 5. Both sets of measurements were analyzed using E_{cut} fixed at 65 eV and s=4.4 which are selected based on the OES measurements in Chapter 6. Considering the uncertainties in both

Table 8.2: Plasma parameters for 100 W Ar-containing plasma (15 mTorr Ar, 15 mTorr He and 3 mTorr Ne) with electron injection (-50 V bias) as a function of electron injection current. Number densities for Ar metastable and resonance levels are from OES branching fraction measurements (Sec. 2.3.2). Number densities for Ar neutral ground state atoms are calculated by ideal gas low based upon the measured gas temperatures. EEDF parameters are based on probe measurements. The ground state density of Ar^+ atoms is assumed to be equal to n_e. Seven Ar and Ar^+ lines are used in the low resolution OES method to determine $n_{\rm tail}$, while ten Ar and Ar^+ lines are employed in the high resolution OES method.

parameter	0 A	0.2 A	0.4 A	0.7 A	1 A
n_0 (Ar) $(10^{13}$ cm$^{-3})$	21.5	20.	19	18.6	18
OES-BF					
high resolution OES					
n_m $(10^8$ cm$^{-3})$	503	340	345	314	360
n_r $(10^8$ cm$^{-3})$	220	80	94	80	106
low resolution OES					
n_m $(10^8$ cm$^{-3})$	655	595	555	500	450
n_r $(10^8$ cm$^{-3})$	130	110	100	90	80
probe EEDF					
n_e $(10^{10}$ cm$^{-3})$	3.5	5	8.5	15.1	18.2
T_x (eV)	3.5	3	2.9	2.7	2.5
x	1.3	1.2	1.2	1.1	1
EEDF tail parameters					
$E_{\rm cut}$ (V)	65	65	65	65	65
s	4.4	4.4	4.4	4.4	4.4
low resolution OES					
$n_{\rm tail}$ $(10^7$ cm$^{-3})$	0	1.5	6.8	14.4	19
high resolution OES					
$n_{\rm tail}$ $(10^7$ cm$^{-3})$	0	2.9	5	13.5	17

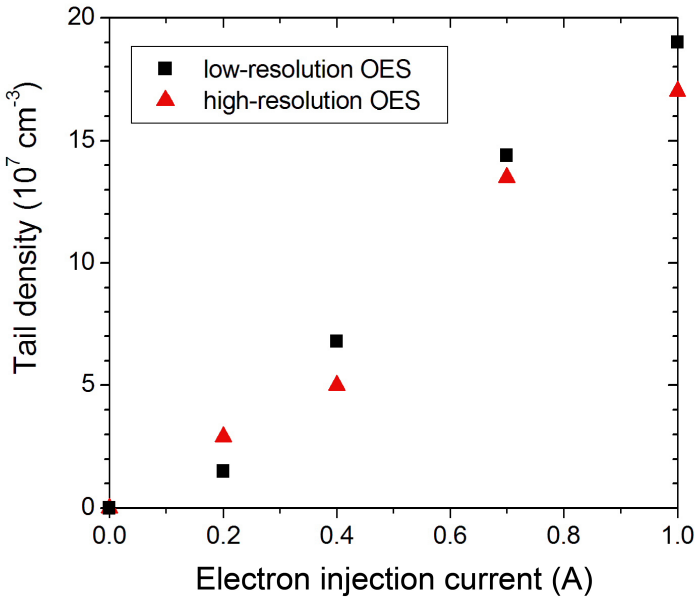

Figure 8.18: OES-derived tail density as a function of electron injection current for a 100 W Ar-containing plasma (15 mTorr Ar, 15 mTorr He and 3 mTorr Ne) with electron injection (-50 V bias). Squares are from low-resolution OES measurements, and triangles are from high-resolution OES measurements.

measurements, the low and high-resolution results are in agreement with the tail density increasing with the electron injection current. Hence, despite the limitations, a low-resolution spectrometer can be used to measure non-Maxwellian EEDFs with enhanced high energy tails.

8.3.5 Conclusion

The sample results illustrate the use of a low-resolution *Verity* spectrometer to measure the density of enhanced EEDF tails. However, there are some limitations in this OES diagnostic. For example, for the low resolution spectra, the number of emission lines that can be included in the emission analysis is smaller, and the uncertainties in measured emission intensities are higher than those measured using a high resolution spectrometer (i.e., PMT). As a result, this low-resolution OES method is not capable of determining both the density and the shape of EEDF tails. Using the electron temperature extracted from the *Verity* 2p analysis by assuming a Maxwellian distribution, or a fixed EEDF shape (i.e., x=1.2, determined by other means), it is possible to measure non-Maxwellian EEDFs with enhanced tail in an all-optical method with a low-resolution spectrometer.

Overall, considering its simplicity, non-invasive nature and inexpensiveness, this 'low resolution' OES diagnostic is a easy-to-use diagnostic for enhanced EEDF tails which may be implemented on plasma process tools.

Chapter 9

Conclusion

9.1 Summary and Conclusions

In this work, OES diagnostics using emissions from different rare gases (i.e., Ar alone, a mix of Ar, Ne and He) for non-Maxwellian EEDFs with enhanced high energy tail were developed and evaluated. Energetic electrons were injected into ICP plasmas from an auxiliary electron source. Plasmas with enhanced enhanced tail EEDFs were produced by this modified ICP source, and the shape of EEDFs were varied systematically over a range that extends beyond what has been used in previous OES studies. The changes in EEDF tails were determined as a function of control parameters (electron injection current, filament bias voltage, source pressure and ICP discharge power) using the OES diagnostic, and the results compared to expected trends in the EEDF tail parameters.

Emissions from different species (i.e., Ar, Ne and He) and from different emitting states of a single species have different ground state and metastable excitation threshold energies, are sensitive to different portions of the EEDF. The capabilities of OES diagnostics can be expanded by increasing the number of emission lines that sample different regions of the EEDF. In the work presented here, a total of five regions were sampled [1]:

(i) E$\sim$2 eV (Ar lines dominated by excitation of metastable atoms)

(ii) E$\sim$13 eV (Ar lines dominated by excitation of ground state atoms)

[1] Or seven regions. The threshold listed in (i) and (ii) are for Ar (2p) levels. Emissions are also used for Ar (3p) levels which have thresholds about 1 eV higher.

(iii) E∼19 eV (Ne lines dominated by excitation of ground state atoms)

(iv) E∼23 eV (He lines dominated by excitation of ground state atoms)

(v) E∼35 eV (Ar^+ lines dominated by excitation of neutral ground state atoms)

The diagnostic is only useful when interesting things happen to the EEDF within this 2-35 eV energy range. For example, using only neutral Ar lines (i) and (ii), it is possible to sample the 'bulk' EEDF in the 0-13 eV range, but little information can be learned about the high energy tail region. Further, the EEDF measurements are restricted to plasmas with electron temperatures in the 1 to ∼10 eV range. The method fails when the electron temperature is either much higher ($T_e \gg 100$ eV) as in the plasma found in stellar interiors and in fusion experiments [16], or much lower ($T_e < 1$ eV) as in afterglow plasmas.

The threshold energies for excitations from the Ar neutral ground state to Ar^+ emitting states (∼35 eV) are much higher than Ar neutral emissions (∼13 eV), and therefore are much more sensitive to differences in the EEDF tails. Using both Ar neutral and Ar^+ emissions in the emission analysis, the OES diagnostic is capable of quantitatively determining one of the three parameters, tail density (n_{tail}), in the log-normal representation of the EEDF tail. In order to extend the capability of the OES diagnostic, Ne and He emissions which have excitation threshold energies of ∼19 eV and ∼23 eV for Ne and He respectively are used to provide information about the 'middle' energy portion of EEDF tails which is missed by using Ar neutral and Ar^+ emissions. This OES diagnostic involving the use of emissions from multiple rare gases (i.e., Ar, Ne and He) can be used to determine both the density (n_{tail}) and the shape (s) parameters of the EEDF tail *simultaneously*. Unlike the bulk temperature measurements, which are primarily sensitive to the threshold energies, the tail measurements are sensitive to the energy dependent shape of the ground state excitation cross sections. These shapes typically vary significantly for various emission lines for electron energies up to a few times the threshold energies. Using the Ar, Ne, He and Ar^+ line set, tail measurements up to 65 eV were made. Variations in the ground state excitation cross sections are probably large enough to permit tail measurements to ∼200 eV. For EEDF tails beyond this range, e.g. keV injected electrons, the emission spectra of these lines are insensitive to the EEDF shape.

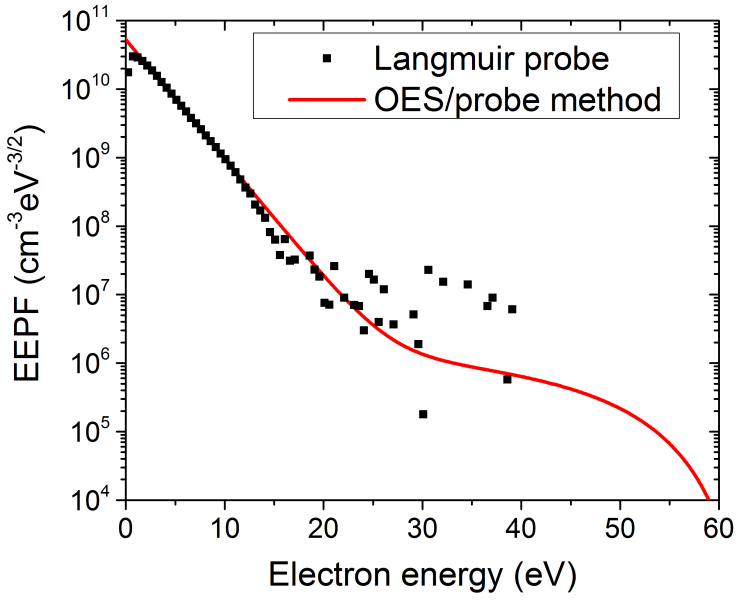

Figure 9.1: EEDF results for a 100 W Ar-containing plasma (15 mTorr Ar, 15 mTorr He and 3 mTorr Ne) with electron injection (1 A, -50 V bias). Squares are probe results. Red line is the EEDF represented by the sum of the 'bulk' (x-form) and the 'tail' (long-normal representation) EEDF. The 'bulk' EEDF is obtained with probe and the 'tail' EEDF is determined using the OES method with Ar, Ne and He emissions.

The OES diagnostic using Ar, Ne and He emissions can measure EEDFs in an energy range beyond the detection limit of the Langmuir probe system used in the present experiment. Fig. 9.1 shows the EEDF results from the probe and OES methods for a sample plasma conditions, i.e., 100 W Ar-containing plasma (15 mTorr Ar, 15 mTorr He and 3 mTorr Ne) with electron injection (1 A, -50 V bias). For the energy range beyond ~20 eV, the probe results are basically noise, while the OES measurements yield an enhanced EEDF tail. Langmuir probe measurements are well suited for determining EEDFs in the low energy range (<15 eV for the present experiment), but the OES diagnostic is sensitive to the high-energy range of the EEDF.

An all-optical emission method for measuring the non-Maxwellian EEDF with enhanced high-energy tail is also possible. With the exception of the ground state number density (which requires the knowledge of the gas pressure and gas temperature), the required metastable and resonance densities can be determined using the OES-BF technique which exploits radiation-trapping. Using these number densities in conjunction with the emission model and the observed Ar neutral emission

intensities, it is possible to measure the 'bulk' EEDF (T_x, x and n_e). Using the emissions from multiple rare gases (i.e., Ar, Ne and He), it is possible to determine EEDF tail distributions (with estimated tail cutoff energies based on physical reasoning). The performance of this all-OES diagnostic was illustrated in the sample measurements of Chapter 7.

The OES diagnostics, in principle, can be by implemented with an inexpensive, compact and easy to use low-resolution spectrometer which are widely equipped on many plasma process tools used in IC manufacturing. The primary difficulty introduced by using a low-resolution spectrometer is suitably resolving the numerous emission lines used in the analysis. As a result, the effective number of lines available for the fitting process is reduced, lowering the power of the OES diagnostic. The low-resolution OES diagnostic can only determine the electron temperature for the 'bulk' EEDF by assuming a Maxwellian distribution or a fixed EEDF shape determined by other means. For the EEDF tail, only the tail density can be determined using Ar neutral and Ar^+ emissions when other parameters for the log-normal representation are known.

Toward the goal of increasing control over the shape (i.e., energy dependence) of the EEDF, several groups have implemented schemes to modify EEDFs on plasma processing systems [40]. In some of the reported schemes, evidence of non-Maxwellian EEDFs with enhanced high-energy tail have been observed. The OES diagnostic developed in this thesis which is capable of determining enhanced EEDF tails may thus be a valuable aid in their development and understanding of plasmas. For example, MacKenzie's Maxwell Demon, consisting of positively (or negatively) biased thin wires, is a useful tool to vary the electron temperature without changing the discharge power and the neutral pressure [150, 151, 152, 153]. Yip *et al.* [154] studied the changes in electron distribution function by the Demon in an Ar containing plasma (0.1-4 mTorr) sustained by energetic electrons emitted from heated and biased (0.75 A, -60 V) filaments. A Langmuir probe was used to measure the 'bulk' low-temperature plasma produced by the high energy 'primary' electrons. Only the 'bulk' electron temperature was reported. With the OES diagnostic presented here, it may be possible to extend the EEDF description into the higher energy range of the primary electrons. The knowledge of the EEDF may be beneficial to their understanding of the filament discharge plasma and the effect of the Demon. Hass *et al.* reported the tailoring of electron energy distributions in low temperature ICP [116] and CCP [45] plasmas by injecting energetic electrons (100 eV) from an auxiliary filament electron source. From Langmuir probe measurements and a global model

analysis, the effect of electron injection on the electron temperature and density was characterized. In their analysis, the effect of an energetic tail on the EEDF was quantified without reference to the exact form of the tail. Using OES diagnostics to better quantity the tail region may aid their analysis. Other schemes have also been used to produce high-energy electrons to improve process outcomes in plasma processing systems [39, 103, 38, 44, 43, 107]. OES diagnostics present a non-invasive way of monitoring the EEDFs of these types of systems in a near real-time fashion which may be needed for process feed-back control. While the low-resolution spectrometer used in this experiment was incapable of measuring EEDFs with enhanced tails, low-cost spectrometers with similar CCD detectors are available with a higher resolution over a restricted wavelength range using the same number of CCD pixels. Or more expensive systems which couple a higher resolution spectrometer with a wide wavelength range can be used to implement the diagnostic in a real-time setting.

9.2 Future work

Future studies may be conducted to address some of the limitations of the OES diagnostics for non-Maxwellian EEDFs with enhanced high-energy tail. For example, one limitation of the present work was the given use of a fixed Ar/Ne/He gas mixture. In general, adding more gases to the plasma increases the complexity of the gas handling system and increases the number of gas-phase reactions possible in the plasma. This was not a true limitation in the present experiment since the existing system was capable of 3 gas mixtures and arbitrarily large amounts of Ne and He could be added to the Ar plasma without effecting the plasma conditions all that much. In this context, the 5:1:5 Ar:Ne:He mixture used in this work is somewhat arbitrary. However, when applying the OES diagnostic to different laboratory and industrial applications, adding such a large amount of rare gases may disturb the plasma properties such that the OES diagnostic is not fully non-invasive. Optimizing the gas mixture of which sufficient emission signal could be measured for the OES analysis without perturbing the plasma may be beneficial for other plasma systems particularly when the trace-gases are added as a tracer to a more reaction gas.

A second limitation found here was that the log-normal distribution used to describe the tail-component of the EEDF uses three parameters E_{cut}, n_{tail} and s, but only the n_{tail} and s values

were generally obtained in the OES fitting process. While this was not much of a limitation in the present experiment where E_{cut} could be determined from the control parameter settings, a robust method for extracting all three parameters will be required for a full diagnostic. For example, high energy electrons have been previously detected using OES methods in a pulsed ICP discharge at the start of a pulse [155]. What value of E_{cut} is appropriate for this system? Additional future efforts will be required to determine the best way to extract values of E_{cut} using OES emissions. Much can be gained by extending the OES diagnostic to measure all three EEDF tail parameters in the log-normal distribution *simultaneously*.

A third limitation found in the spectra recorded with a low-resolution spectrometer was that the Ne and He emissions could not be fully resolved and used in the OES analysis to determine the EEDF tail. Therefore, the OES diagnostic with low-resolution spectrometers is only capable of measuring the EEDF tail density using Ar neutral and Ar^+ emissions. In principle, by considering the sum of multiple emission lines in the emission analysis (as described in Sec. 8.2), Ne and He emissions can be employed in the OES analysis without resolving them in the low-resolution spectra, allowing the possibility to determine both the density and the shape of EEDF tails. This would combine the benefits of a fast spectra acquisition time ($\sim$0.1 s) of the low-resolution spectrometer with a non-Maxwellian EEDF shape determination to allow real-time monitoring of the EEDF for plasma process tools.

Provided a way is found to fully extract the tail parameters from the optical measurements, a future direction of the diagnostic is to study pulsed discharges [38]. As mentioned previously, the presence of a significant number of 'hot' electrons at the start of a pulse were detected in a pulsed ICP using a single pair of Ar neutral lines [155]. This single line pair, however, can not reveal the energy distribution. Measuring the EEDF would aid in understanding the exact mechanism producing these high energy electrons.

Chapter 10

Bibliography

[1] A. Bogaerts, E. Neyts, R. Gijbels, and J van der Mullen. Gas discharge plasmas and their applications. *Spectrochim. Acta Part B*, 57:609–658, 2002.

[2] J. Hopwood. Review of inductively coupled plasmas for plasma processing. *Plasma Sources Sci. Technol.*, 1:109, 1992.

[3] J. R. Roth. *industrial Plasma Engineering* . Institute of Physics Publishing, London, one edition, 2001.

[4] H. Schlüter and A. Shivarova. *Advanced Technologies Based on Wave and Beam Generated Plasmas*. Springer Netherlands, Bulgaria, 1999.

[5] Ara Chutjian. Recent Applications of Gaseous Discharges: Dusty Plasmas and Upward-directed Lightning. *Adv. At. Mol. Opt. Phys.*, 43:373, 2000.

[6] A. Grill. *Cold Plasma in Materials Fabrication: from Fundamentals to Applications*. Wiley-IEEE Press, New York, 1994.

[7] H. K. Yasuda. *Plasma Polymerization and Plasma Interactions with Polymeric Materials*. Wiley, New York, 1990.

[8] U. S. Kalghatgi, G. Fridman, M. Copper, G. Nagaraj, M. Peddinghaus, M. Balasubramanian, V. N. Vasilets, A. F. Gutsol, A. Fridman, and G. Friedman. Mechanism of Blood Coagulation

by Nonthermal Atmospheric Pressure Dielectric Barrier Discharge Plasma. *IEEE Trans. Plasma Sci.*, 35:1559, 2007.

[9] V. M. Donnelly and A. Kornblit. Plasma etching: Yesterday, today, and tomorrow. *J. Vac. Sci. Technol. A*, 31:050825, 2013.

[10] J. Pelletier. Plasma-Based Ion Implantation and Deposition: A Review of Physics, Technology, and Applications. *IEEE Trans. Plasma Sci.*, 33:6, 2005.

[11] H. Abe, M. Yoneda, and N. Fujiwara. Developments of Plasma Etching Technology for Fabricating Semiconductor Devices. *Jpn. J. Appl. Phys.*, 47:1435, 2008.

[12] N. Hershkowitz. Role of Plasma-Aided Manufacturing in Semiconductor Fabrication. *IEEE Trans. Plasma Sci.*, 26:6, 1998.

[13] M. A. Lieberman and A. J. Lichtenberg. *Principles of Plasma Discharges and Materials Processing*. John Wiley & Sons, New York, 1994.

[14] H. Kodama, A. Shirakura, A. Hotta, and T. Suzuki. Gas barrier properties of carbon films synthesized by atmospheric pressure glow plasma. *Surf. Coat. Technol.*, 201:913, 2006.

[15] R. Hippler, S. Pfau, M. Schmidt, and K. H. Schoenbach. *Low Temperature Plasma Physics: Fundamental Aspects and Applications*. Wiley, New York, 2001.

[16] W. C. Chen, X. M. Zhu, S. Zhang, and Y. K. Pu. Reconstruction of ion energy distribution function in a capacitive rf discharge. *Appl. Phys. Lett*, 94:211503, 2009.

[17] Valery A. Godyak. Nonequilibrium EEDF in Gas Discharge Plasmas. *IEEE Trans. Plasma Sci.*, 34:755–766, 2006.

[18] K. H. Becker and C. C. Lin. Elementary collision processes in plasmas. In *Low Temperature Plasmas*. Wiley-VHG, 2nd edition, 2007.

[19] H Sugai, I Ghanashev, M Hosokawa, K Mizuno, K Nakamura, H Toyoda, and K Yamauchi. Electron energy distribution functions and the influence on fluorocarbon plasma chemistry. *Plasma Sources Sci. Technol.*, 10:378–385, 2001.

[20] R. R. Schaller. Moore's law: past, present and future. *IEEE Spectrum*, 34:53, 1997.

[21] R. G. poulsen. Plasma etching in integrated circuit manufacture—A review. *J. Vac. Sci. Technol.*, 14:266, 1977.

[22] John V. Ringwood, Shane A. Lynn, Giorgio Bacelli, Beibei Ma, Emanuele Ragnoli, and Sean McLoone. Estimation and Control in Semiconductor Etch: Practice and Possibilities. *IEEE Trans. on Semiconductor Manufacturing*, 23:87–98, 2010.

[23] M. Armacost, P. D. Hoh, R. Wise, W. Yan, J. J. Brown, J. H. Keller, G. A. Kaplita, S. D. Halle, K. P. Muller, M. D. Naeem, S. Srinivasan, H. Y. Ng, M. Gutsche, A. Gutmann, and B. Spuler. Plasma-etching processes for ULSI semiconductor circuits. *IBM J. Res. Dev.*, 43(1/2):1–26, 1999.

[24] Hyungjoo Shin, Weiye Zhu, Vincent M. Donnelly, and Demetre J. Economou. Surprising importance of photo-assisted etching of silicon in chlorine-containing plasmas. *J. Vac. Sci. Technol. A*, 30:021306, 2012.

[25] F. H. Bell and O. Joubert. Polysilicon gate etching in high density plasmas. V. Comparison between quantitative chemical analysis of photoresist and oxide masked polysilicon gates etched in $HBr/Cl_2/O_2$ plasmas. *J. Vac. Sci. Technol. B*, 15:88, 1997.

[26] H.J. Levinstein and F. Vratny. Apparatus and method for plasma-assisted etching of wafers, December 6 1983. US Patent 4,419,201.

[27] O. A. Popov. *High density plasma sources*. Noyes Publications,, Park Ridge, NJ, 1996.

[28] D. Bhattacharya and N. K. Jha. FinFETs: From Devices to Architectures. *Advances in Electronics*, 2014:21, 2014.

[29] S. banna, A. Agarwal, G. Cunge, M. Darnon, E. Pargon, and O. Joubert. Pulsed high-density plasmas for advanced dry etching processes. *J. Vac. Sci. Technol. A*, 30:040801, 2012.

[30] Z. C. Lu, J. E. Foster, T. G. Snodgrass, J. H. Booske, , and A. E. Wendt. Measurements of electron energy distribution function in an argon/copper plasma for ionized physical vapor deposition. *J. Vac. Sci. Technol. A*, 17:840–844, 1999.

[31] K. Hassouni, C. D. Scott, S. Farhar, A. Gicquel, and M. Capitelli. Non-Maxwellian effect on species and energy transport in moderate pressure H_2 plasmas. *Surf. Coat. Technol.*, 97:391–403, 1997.

[32] V. A. Godyak, R. B. Piejak, and B. M. Alexandrovich. Measurements of electron energy distribution in low pressure RF discharges. *Plasma Sources Sci. Technol.*, 1:36–58, 1992.

[33] J. K. Lee F. Iza and M. G. Kong. Electron kinetics in radio-frequency atmospheric-pressure microplasmas. *Phys. Rev. Lett.*, 99:075004, 2007.

[34] I. D. Kaganovich, V. I. Demidov, S. F. Adams, and Y. Raitses. Non-local collisionless and collisional electron transport in low-temperature plasma. *Plasma Phys. and Contr. Fusion*, 51:124003, 2009.

[35] U. Kortshagen, I. Pukropski, and L. D. Tsendin. Experimental investigation and fast 2-dimensional self-consistent kinetic modeling of a low-pressure inductively-coupled rf discharge. *Phys. Rev. E*, 51:6063–6074, 1995.

[36] V. A. Godyak, R. B. Piejak, and B. M. Alexandrovich. Electron enery distribution function measurements and plasma parameters in inductively coupled argon plasma. *Plasma Sources Sci. Technol.*, 11:525–43, 2002.

[37] V. I. Kolobov, D. F. Beale, L. J. Mahoney, and A. E. Wendt. Non-local electron kinetics in an inductively coupled radio frequency discharge. *Appl. Phys. Lett.*, 65:537, 1994.

[38] Samer Banna, Ankur Agarwal, G. Cunge, M. Darnon, E. Pargon, and O. Joubert. Pulsed high-density plasmas for advanced dry etching processes. *J. Vac. Sci. Technol. A*, 30:040801, 2012.

[39] Mingmei Wang and M. J. Kushner. High energy electron fluxes in dc-augmnted capacitively coupled plasmas II. Effects on twisting in high aspect ratio etching of dielectrics. *J. Appl. Phys*, 107:023309, 2010.

[40] V. A. Godyak. Electron energy distribution function control in gas discharge plasmas. *Phys. Plasmas*, 20:101611, 2013.

[41] L. Lie, S. Sridhar, V. M. Donnelly, D. J. Economou, M. D. Logue, and M. J. Kushner. External control of electron energy distributions in a dual tandem inductively coupled plasma. *J. Appl. Phys.*, 118:083303, 2015.

[42] J. I. Hong, S. H. Seo, S. S. Kim, N. S. Yoon, C. S. Chang, and H. Y. Chang. Electron temperature control with grid bias in inductively coupled argon plasmas. *Phys. Plasmas*, 6:1017, 1999.

[43] C. C. W. Chung, S. S. Kim, and H. Y. Chang. Experimental measurement of the electron energy distribution function in the radio frequency electron cyclotron resonance inductive discharge. *Phys. Rev. E*, 69:016406, 2004.

[44] A. Mareska, K. Orlov, and U. Kortshagen. Experimental study of diffusive cooling of electrons in a pulse inductively coupled plasma. *Phys. Plasmas*, 65:056405, 2002.

[45] F. A. Haas, A. Goodyear, and N. St. J. Braithwaite. Tailoring of electron energy distributions in low temperature plasmas. *Plasma Sources Sci. Technol.*, 7:471–477, 1998.

[46] Plasma 2010 Committee. *Plasma Science: Advancing Knowledge in the National Interest*, chapter 2, pages 38–74. National Academy Press, 2007.

[47] Low Temperature Plasma Science: Not Only the Fourth State of Matter but All of Them, 2008.

[48] D. D. Monahan and M. M. Turner. Global models of electronegative discharges: critical evaluation and practical recommendations. *Plasma Sources Sci. Technol.*, 17(4):045003, 2008.

[49] N. Hershkowitz. *Plasma Diagnostics*, volume 1, chapter How Langmuir Probes Work, pages 113–184. Academic Press, San Diego, 1989.

[50] V. I. Demidov, S. V. Ratynskaia, and K. Rypdal. Electric probes for plasmas: The link between theory and instrument. *Rev. Sci. Instr.*, 73:3409–3439, 2002.

[51] Xi-Ming Zhu and Yi-Kang Pu. Optical emission spectroscopy in low-temperature plasmas containing argon and nitrogen: determination of the electron temperature and density by the line-ratio method. *J. Phys. D*, 43:403001, 2010.

[52] U. Fantz. Basics of plasma spectroscopy. *Plasma Sources Sci. Technol.*, 15:S137, 2006.

[53] H. R. Griem. *Principles of Plasma Spectroscopy.* Cambridge University Press, Cambridge, 1997.

[54] Takashi Fujimoto. *Plasma Spectroscopy.* Clarendon Press, Oxford, 2004.

[55] E. O. Degenkolb, C.J. Mogab, M.R. Goldrick, and J.E. Griffiths. Spectroscopic study of radiofrequency oxygen plasma stripping of negative photoresists. 1. Ultraviolet-spectrum. *Appl. Spectrosc.*, 30:520–527, 1976.

[56] J. B. Boffard, B. Chiaro, T. Weber, and C. C. Lin. Electron-impact excitation of argon: optical emission cross sections in the range 300-2500 nm. *At. Data Nuc. Data Tables*, 93:831–863, 2007.

[57] J. B. Boffard, G. A. Piech, M. F. Gehrke, L. W. Anderson, and C. C. Lin. Measurement of electron-impact excitation cross sections out of metastable levels of argon and comparison with ground-state excitation. *Phys. Rev. A*, 59:2749–2763, 1999.

[58] R. O. Jung, J. B. Boffard, L. W. Anderson, and C. C. Lin. Excitation into $3p^5 5p$ levels from the metastable levels of Ar. *Phys. Rev. A*, 75:052707, 2007.

[59] J. B. Boffard, R. O. Jung, C. C. Lin, and A. E. Wendt. Optical emission measurements of electron energy distributions in low-pressure inductively-coupled plasmas. *Plasma Sources Sci. Technol.*, 19:065001, 2010.

[60] G. A. Piech, J. B. Boffard, M. F. Gehrke, L. W. Anderson, and C. C. Lin. Measurement of cross sections for electron excitation out of the metastable levels of argon. *Phys. Rev. Lett.*, 81:309–312, 1998.

[61] NIST ASD Team, Yu Ralchenko, A. E. Kramida, and J. Reader. NIST Atomic Spectra Database (version 3.1.5), [Online]. Available: `http://www.nist.gov/asd3`, 2010. National Institute of Standards and Technology, Gaithersburg, MD.

[62] W. L. Wiese, J. W. Brault, K. Danzmann, V. Helbig, and M. Kock. Unified set of atomic transition probablilities for neutral argon. *Phys. Rev. A*, 39:2461, 1989.

[63] O. Zatsarinny and K. Bartschat. B-spline calculations of oscillator strengths in neutral argon. *J. Phys. B*, 39:2145, 2006.

[64] J. E. Chilton, M. D. Stewart, and C. C. Lin. Electron-impact excitation cross sections of neon. *Phys. Rev. A*, 61:052708, 2000.

[65] J. B. Boffard, M. L. Keeler, G. A. Piech, L. W. Anderson, and C. C. Lin. Measurement of electron-impact excitation cross sections out of the neon $^3P_2$ metastable level. *Phys. Rev. A*, 64:032708, 2001.

[66] F. A. Sharpton, R. M. St. John, C. C. Lin, and F. E. Fajen. Experimental and Theoretical Studies of Electron-Impact Excitation of Neon. *Phys. Rev. A*, 2:1305–1322, 1970.

[67] R. M. St John, F. L. Miller, and C. C. Lin. Absolute electron excitation cross sections of helium. *Phys. Rev.*, 134:A888, 1964.

[68] John B Boffard. *Experimental Measurement of Electron-Impact Excitation Cross Sections out of Rare-Gas Metastable Levels*. PhD thesis, University of Wisconsin-Madison, 1998.

[69] J. E. Chilton. Private communication., 1997. Some of this data can also be found in Appendix E of G. A. Piech's PhD thesis (1998).

[70] B. Van Zyl, G. H. Dunn, G. Chamberlain, and D. W. O. Heddle. Benchmark cross sections for electron-impact excitation of $n\,^1S$ levels of He. *Phys. Rev. A*, 22:1916, 1980.

[71] H. R. Griem. *Plasma Spectroscopy*. McGraw-Hill, New York, 1964.

[72] D. A. O. Hope, T. I. Cox, and V. G. I. Deshmukh. Langmuir probe and optical emission spectroscopic studies of Ar and O_2 plasmas. *Vacuum*, 37:275, 1987.

[73] J. B. Boffard, C. C. Lin, and C. A. DeJoseph. Application of excitation cross sections to optical plasma diagnotics. *J. Phys. D*, 37:R143–R161, 2004.

[74] J. B. Boffard, R. O. Jung, C. C. Lin, L. E. Aneskavich, and A. E. Wendt. Optical diagnostics for characterization of electron energy distributions: argon inductively coupled plasmas. *Plasma Sources Sci. Technol.*, 20:055006, 2011.

[75] J. B. Boffard, R. O. Jung, C. C. Lin, and A. E. Wendt. Measurement of metastable and resonance level densities in rare gas plasmas by optical emission spectroscopy. *Plasma Sources Sci. Technol.*, 18:035017, 2009.

[76] Shicong Wang, A. E. Wendt, J. B. Boffard, C. C. Lin, Svetlana Radovanov, and Harold Persing. Non-invasive, real-time measurements of plasma parameters via optical emission spectroscopy. *J. Vac. Sci. Technol. A*, 31:021303, 2013.

[77] M. V. Malyshev and V. M. Donnelly. Determination of electron temperatures in plasmas by multiple rare gas optical emission, and implications for advanced actinometry. *J. Vac. Sci. Technol. A*, 15:550, 1997.

[78] M. V. Malyshev and V. M. Donnelly. Trace rare gases optical emission spectroscopy: Nonintrusive method for measuring electron temperatures in low-pressure, low-temperature plasmas. *Phys. Rev. E*, 60:6016, 1999.

[79] V. M. Donnelly and M. J. Schabel. Spatially resolved electron temperatures, species concentrations, and electron energy distributions in inductively coupled chlorine plasmas, measured by trace-rare gases optical emission spectroscopy. *J. Appl. Phys.*, 91:6288, 2002.

[80] S. Iordanova and I. Koleva. Optical emission specroscopy diagnostics of inductively-driven plasmas in argon gas at low pressures. *Spectrochim. Acta Part B*, 62:344–356, 2007.

[81] Yu. M. Smirnov. Cross Sections for Aluminum Atom Excitation by Electron Impact. *Opt. Spectrosc.*, 82:200–204, 1997.

[82] J T Gudmundsson. On the effect of the electron energy distribution on the plasma parameters of an argon discharge: a global (volume-averaged) model study. *Plasma Sources Sci. Technol.*, 10:76–81, 2001.

[83] K. Behringer and U. Fantz. Spectroscopic diagnostics of glow discharge plasmas with non-Maxwellian electron energy distributions. *J. Phys. D*, 27:2128, 1994.

[84] V. A. Godyak, R. B. Piejak, and B. M. Alexandrovich. Probe diagnostics of non-Maxwellian plasmas. *J. Appl. Phys.*, 73:3657, 1993.

[85] Albert Meige and Rod W. Boswell. Electron energy distribution functions in low-pressure inductively coupled bounded plasmas. *Phys. of Plasmas*, 13:092104, 2006.

[86] E. Limpert, W. A. Stahel, and M. Abbt. Log-normal distributions across the sciences: Keys and clues. *BioScience*, 51:341, 2001.

[87] A. C. G. Mitchell and M. W. Zemansky. *Resonance Radiation and Excited Atoms.* Cambridge University Press, Cambridge, 1961.

[88] K. Behringer and U. Fantz. Some Basic Physics Results for Plasma Spectroscopy and Modelling. *Contrib. Plasma Phys.*, 39:411, 1999.

[89] F. E. Irons. The Escape Factor in Plasma Spectroscopy-I. The Escape Factor Defined and Evaluated. *J. Quant. Spectrosc. Radit. Transfer*, 22:1–20, 1979. [Part-II, *op. cit.*, pp. 21-36, part-III, *op. cit.*, pp. 37-44.].

[90] T. Holstein. Imprisonment of Resonance Radiation in Gases. *Phys. Rev.*, 72:1212, 1947.

[91] T. Holstein. Imprisonment of Resonance Radiation in Gases. II. *Phys. Rev.*, 83:1159, 1951.

[92] R Mewe. Relative Intensity of Helium Spectral Lines as a Function of Electron Temperature and Density. *Brit. J. Appl. Phys.*, 18:107, 1967.

[93] M. Schulze, A. Yanguas-Gil, A von Keudell, and P Awakowicz. A robust method to measure metastable and resonant state densities from emission spectra in argon and argon-diluted low pressure plasmas. *J. Phys. D: Appl. Phys.*, 41:065206, 2008.

[94] Xi-Ming Zhu, Wen-Cong Chen, Jiang Li, and Yi-Kang Pu. Determining the electron temperature and the electron density by a simple collisional-radiative model of argon and xenon in low-pressure discharges. *J. Phys. D*, 42:025203, 2009.

[95] Xi-Ming Zhu and Yi-Kang Pu. A simple collisional-radiative model for low-pressure argon-oxygen mixture discharges. *J. Phys. D*, 40:5202–5205, 2007.

[96] M. J. Druyvesteyn. Der Niedervoltbogen. *Z. Phys.*, 64:781, 1930.

[97] A. E. Wendt. Passive external radio frequency filter for Langmuir probes. *Review of Scientific Instruments*, 72(7):2926–2930, July 2001.

[98] K. F. Schoenberg. Electron distribution function measurement by harmonically driven electrostatic probes. *Rev. Sci. Instrum*, 51:1159, 1980.

[99] U. Kortshagen and H. Schl´uter. Determination of electron energy I distribution functions in surface wave I produced plasmas: II. Measurements . *J. Phys. D: Appl. Phys.*, 24:1585, 1991.

[100] A. Dyson, P. Bryant, and J. E. Allen. Multiple harmonic compensation of Langmuir probes in rf discharges . *Meas. Sci. Technol.*, 11:554, 2000.

[101] J. L.Jauberteau and I. Jauberteau. Electron energy distribution function in plasma determined using numerical simulations of multiple harmonic components on Langmuir probe characteristic—Efficiency of the method. *Rev. Sci. Instrum*, 78:043501, 2007.

[102] D. A. Herman and A. D. Gallimore. Discharge Cathode Electron Energy Distribution Functions in a 40-cm NEXT-type Ion Engine. Tuscon, Arizona, July 2005. American Insititute of Aeronautics and Astronautics, American Insititute of Aeronautics and Astronautics.

[103] Mingmei Wang and M. J. Kushner. High energy electron fluxes in dc-augmnted capacitively coupled plasmas I. Fundamental characteristics. *J. Appl. Phys*, 107:023308, 2010.

[104] D. J. Heason and J. W. Bradley. Modifying the IEDFs at a plasma boundary in a low-pressure RF discharge using electron beam injection. *Plasma Sources Sci. Technol.*, 10:627–635, 2001.

[105] A. A. Goruppa, N. St. J. Braithwaite, and D. M. Grant. Direct electrical control of diamond-like carbon growth by plasma-enhanced CVD. *Diamond and Related Materials*, 3:1223–1226, 1994.

[106] Y Andrew, I. Abraham, J. H. Booske, Z. C. Lu, and A. E. Wendt. Absolute densities of long lived species in an ionized physical vapor deposition copper-argon plasma. *J. Appl. Phys.*, 88:3208, 2000.

[107] C. A. DeJoseph Jr., V. I. Demidov, and A. A. Kudryavtsev. Modification of a nonlocal electron energy distribution in a bound plasma. *Phys. Rev. E*, 72:036410, 2005.

[108] A. M. Marakhtanov, M. Tuszewski, M. A Lieberman, A. J Lichtenberg, and P. Chabert. Stable and unstable behavior of inductively coupled electronegative discharges. *J. Vac. Sci. Technol. A*, 21:1849, 2003.

[109] N. C. M. Fuller, I. P. Herman, and V. M. Donnelly. Optical actinometry of Cl_2, Cl, Cl^+, and Ar^+ densities in inductively coupled Cl_2-Ar plasmas. *J. Appl. Phys.*, 90:3182–3191, 2001.

[110] M. V. Malyshev and V. M. Donnelly. Diagnostics of chlorine inductively coupled plasmas. measurement of electron temperatures and electron energy distribution functions. *Journal of Applied Physics*, 87(4):1642–1649, 2000.

[111] N. C. M. Fuller, Irving P. Herman, and Vincent M. Donnelly. Optical actinometry of cl2, cl, cl+, and ar+ densities in inductively coupled cl2–ar plasmas. *Journal of Applied Physics*, 90(7):3182–3191, 2001.

[112] N. C. M. Fuller, M. V. Malyshev, V. M. Donnelly, and I. P. Herman. Characterization of transformer coupled oxygen plasmas by trace rare gases-optical emission spectroscopy and Langmuir probe analysis. *Plasma Souruces. Sci. Technol.*., 9:116–127, 2000.

[113] Z. Chen, V. M. Donnelly, and D. J. Economou. Measurement of electron temperatures and electron energy distribution functions in dual frequency capacitively coupled CF4/O2 plasmas using trace rare gases optical emission spectroscopy. *J. Vac. Sci. Technol. A*, 27(5):1159, 2009.

[114] Zhu Ximing and Pu Yikang. Determination of non-maxwellian electron energy distributions in low-pressure plasmas by using the optical emission spectroscopy and a collisional-radiative model. *Plasma Science and Technology*, 13(3):267, 2011.

[115] D. Sydorenko, A. Smolyakov, I. Kaganovich, and Y. Raitses. Effects of non-maxwellian electron velocity distribution function on two-stream instability in low-pressure discharges. *Phys. Plasmas*, 14:013508, 2007.

[116] F. A. Haas and N. St. J. Braithwaite. Tailoring of electron energy distributions in low-pressure inductive discharges. *Applied Physics Letters*, 74(3):338–340, 1999.

[117] Xi-Ming Zhu and Yi-Kang Pu. A simple collional-radiative model for low-pressure argon discharges. *J. Phys. D*, 40:2533–2538, 2007.

[118] B. Wu, A. Kumar, and S. Pamarthy. High aspect ratio silicon etch: A review. *J. Appl. Phys.*, 108:051101, 2010.

[119] R. Hon, S. X. D. Zhang, and S. W. R. Lee. Formation of through-silicon-vias by laser drilling and deep reactive ion etching. *ASME International Mechanical Engineering Congress and Exposition*, 13-20:243–248, 2004.

[120] M. J. Schabel, V. M. Donnelly, A. Kornblit, and W. W. Tai. Determination of electron temperature, atomic fluorine concentration, and gas temperature in inductively coupled fluorocarbon/rare gas plasmas using optical emission spectroscopy. *Journal of Vacuum Science & Technology A*, pages 555–563.

[121] H. Cho, K. P. Lee, Y. B. Hahn, E. S. Lambers, and S. J. Pearton. Effects of ultraviolet illumination on dry etch rates of nife-based magnetic multilayers. *Journal of Vacuum Science & Technology A*, 18(4):1273–1277, 2000.

[122] J. W. Butterbaugh, D. C. Gray, and H. H. Sawin. Plasma–surface interactions in fluorocarbon etching of silicon dioxide. *Journal of Vacuum Science & Technology B*, 9(3):1461–1470, 1991.

[123] D. Dergez, j. Schalko, A. Bittner, and U. Schmid. Fundamental properties of a-SiNx:H thin films deposited by ICP-PECVD for MEMS applications. *Appl. Surf. Sci*, 284:348–353, 2013.

[124] N Laidani, R Bartali, P Tosi, and M Anderle. Argon–hydrogen rf plasma study for carbon film deposition. *Journal of Physics D: Applied Physics*, 37(18):2593, 2004.

[125] S.J. Cho, J.W. Roberts, I. Guiney, X. Li, G. Ternent, K. Floros, C.J. Humphreys, P.R. Chalker, and I.G. Thayne. A study of the impact of in-situ argon plasma treatment before atomic layer deposition of al2o3 on gan based metal oxide semiconductor capacitor. *Microelectronic Engineering*, 147:277 – 280, 2015.

[126] D. R. Cote, S. V. Nguyen, A. K. Stamper, D. S. Armbrust, D. Tobben, R. A. Conti, and G. Y. Lee. Plasma-assisted chemical vapor deposition of dielectric thin films for ulsi semiconductor circuits. *IBM J. Res. Dev.*, 43(1-2):5–38, January 1999.

[127] Argon plasma immersion ion implantation of polystyrene films. *Nuclear Instruments and Methods in Physics Research Section B: Beam Interactions with Materials and Atoms*, 266(7):1074 – 1084, 2008.

[128] J Hopwood. Review of inductively coupled plasmas for plasma processing. *Plasma Sources Science and Technology*, 1(2):109, 1992.

[129] J. R. Conrad, J. L. Radtke, R. A. Dodd, Frank J. Worzala, and Ngoc C. Tran. Plasma source ion implantation technique for surface modification of materials. *Journal of Applied Physics*, 62(11):4591–4596, 1987.

[130] J. E. Chilton, J. B. Boffard, R. S. Schappe, and C. C. Lin. Measurement of electron-impact excitation into the $3p^5 4p$ levels of argon using Fourier-transform spectroscopy. *Phys. Rev. A*, 57:267–277, 1998.

[131] A. E. Wendt. *Lecture Notes for ECE 528 Plasma Processing.* University Of Wisconsin-Madison, 2005.

[132] V M Donnelly. Plasma electron temperatures and electron energy distributions measured by trace rare gases optical emission spectroscopy. *Journal of Physics D: Applied Physics*, 37(19):R217, 2004.

[133] V. M. Donnelly and M. J. Schabel. Spatially resolved electron temperatures, species concentrations, and electron energy distributions in inductively coupled chlorine plasmas, measured by trace-rare gases optical emission spectroscopy. *Journal of Applied Physics*, 91(10):6288–6295, 2002.

[134] M. J. Schabel, V. M. Donnelly, A. Kornbilt, and W. W. Tai. Determination of electron temperature, atomic flourine concentration, and gas temperature in inductively coupled flurocarbon/rare gas plasmas using optical emission spectroscopy. *J. Vac. Sci. Technol. A*, 20:555–563, 2002.

[135] R. O. Jung, G. A. Piech, M. L. Keeler, J. B. Boffard, L. W. Anderson, and C. C. Lin. Electron-impact excitation cross sections into Ne($2p^5 3p$) levels for plasma applications. *J. Appl. Phys.*, 109:123303, 2011.

[136] R. Stephen Berry. The theory of penning ionization. *Radiation Research*, 59(2):367–375, 1974.

[137] Kadou Hirobe and Takashi Tsuchimoto. End point detection in plasma etching by optical emission spectroscopy. *J. Electrochem. Soc.*, 127:234, 1980.

[138] E. O. Degenkolb, C. J. Mogab, M. R. Goldrick, and J. E. Griffiths. Subscribed content spectroscopic study of radiofrequency oxygen plasma stripping of negative photoresists. i. ultraviolet spectrum. *Appl. Spectrosc.*, 30:520, 1976.

[139] W. R. Harshbarger, R. A. Porter, T. A. Miller, and P. Norton. Study of optical emission from an rf plasma during semiconductor etching. *Appl. Spectrosc.*, 31:201, 1977.

[140] Shicong Wang, A. E. Wendt, J. B. Boffard, C. C. Lin, Svetlana Radovanov, and Harold Persing. Non-invasive, real-time measurements of plasma parameters via optical emission spectroscopy. *J. Vac. Sci. Technol. A*, 31:021303, 2013.

[141] W. Wang, J. Bi, and J. Zhao. Plasma etching process monitoring with optical emission spectroscopy. Chengdu, China, May 2009. IEEE International Conference on Industrial Mechatronics and Automation, IEEE.

[142] F. Weilnboeck, N. Kumar, G. S. Oehrlein, T.-Y. Chung, D. Graves, M. Li, E. A. Hudson, and E. C. Benck. Real-time measurements of plasma photoresist modifications: The role of plasma vacuum ultraviolet radiation and ions. *J. Vac. Sci. Technol. B*, 30:031807, 2012.

[143] Hyungjoo Shin, Weiye Zhu, Vincent M. Donnelly, and Demetre J. Economou. Surprising importance of photo-assisted etching of silicon in chlorine-containing plasmas. *J. Vac. Sci. Technol. A*, 30:021306, 2012.

[144] R. Abdolvand and F. Ayazi. An advanced reactive ion etching process for very high aspect-ratio sub-micron wide trenches in silicon. *Sens. Actuators A*, 144:109–116, 2008.

[145] V. M. Donnelly. Plasma electron temperatures and electron energy distributions measured by trace rare gases optical emission spectroscopy. *J. Phys. D*, 37:R217–R236, 2004.

[146] D. Mariotti, Y. Shimizu, T. Sasaki, and N. Koshizaki. Gas temperature and electron temperature measurements by emission spectroscopy for an atmospheric microplasma. *J. Appl. Phys.*, 101:013307, 2007.

[147] Jiang Li, Fei-Xiang Liu, Xi-Ming Zhu, and Yi-Kang Pu. The spatially resolved measurements of the atomic densities in argon Paschen 1s levels by OES in a capacitively coupled plasma. *J. Phys. D*, 44:292001, 2011.

[148] Anne P. Thorne. *Spectrophysics, 2nd ed.* Chapman and Hall, London, 1988.

[149] J. B. Boffard, R. O. Jung, C. C. Lin, L. E. Aneskavich, and A. E. Wendt. Argon 420.1 nm-419.8 nm emission line ratio for measuring plasma effective electron temperatures. *J. Phys. D*, 45:045201, 2012.

[150] K. R. MacKenzie, R. J. Taylor, D. Cohn, E. Ault, and H. Ikezi. Plasma electron heating by absorption of cold electrons. *Applied Physics Letters*, 18(12):529–530, 1971.

[151] N. Hershkowitz, C.-S. Yip, and G. D. Severn. Experimental test of instability enhanced collisional friction for determining ion loss in two ion species plasmas a). *Physics of Plasmas*, 18(5), 2011.

[152] Kohgi Kato, Satoru Iizuka, and Noriyoshi Sato. Electron temperature control for plasmas passing through a negatively biased grid. *Applied Physics Letters*, 65(7), 1994.

[153] K H Bai, C K Choi, and H Y Chang. Electron temperature control with a small mesh number grid in inductively coupled plasmas. *Plasma Sources Science and Technology*, 13(4):662, 2004.

[154] Chi-Shung Yip, J P Sheehan, Noah Hershkowitz, and Greg Severn. Mackenzie's demon with instabilities. *Plasma Sources Science and Technology*, 22(6):065002, 2013.

[155] J. B. Boffard, S. Wang, C. C. Lin, and A. E. Wendt. Detection of fast electrons in pulsed argon inductively-coupled plasmas using the 420.1–419.8 nm emission line pair. *Plasma Sources Sci. Technol.*, 24:065005, 2015.